UNIVERSITÀ DEGLI STUDI DI MILANO
DEPARTMENT OF PHYSICS

PHD SCHOOL IN
PHYSICS, ASTROPHYSICS AND APPLIED PHYSICS
CYCLE XXXIII

SOFT POLYMERIC NANOCOMPOSITES FOR ELECTROMECHANICAL CONVERSION

Disciplinary Scientific Sector FIS/03

PhD Thesis of:

Sara Moon Villa

Director of the School: Prof. Matteo Paris

Supervisor of the Thesis: Prof. Paolo Milani

A.Y. 2021-2022

SUMMARY

1. INTRODUCTION

The nature of progress is that what begins as a luxury for the rich becomes a necessity for the poor as it's developed and passed on.
- Milton Friedman

1.1 CONTEXT

Today we are at the edge of the Fourth Industrial Revolution, characterized by a range of new technologies that are fusing the physical, digital and biological worlds, impacting all disciplines, economies and industries. Internet of Things, big data, cloud robotics, artificial intelligence, nanotechnology, quantum computing, and additive manufacturing are some of the key-technologies that are enabling the next-generation industry.

The core concept behind the Fourth Industrial Revolution relies on Cyber Physical Systems: computer-based systems that integrate physical components with cyber space to perform advanced automation and control tasks. Embedded computers and communication networks govern physical actuators that operate and receive inputs from sensors, creating a smart control loop capable of adaptation, autonomy, and improved efficiency. Almost all devices necessary for these tasks are typically encompassed by the Internet of Things [1].

Internet of Things
The term Internet of things (IoT) is used to describe the networked interconnection of sensors and actuators embedded in everyday objects [2] allowing information to be shared between systems that affect each other, in order to provide them better awareness and improve their efficiency, reliability and sustainability [3]. The Internet of Things can be applied to multiple environments (Figure 1.1), since it is adjustable to almost any technology, and is nowadays integrated in many sectors to simplify, improve, automate and control different processes.

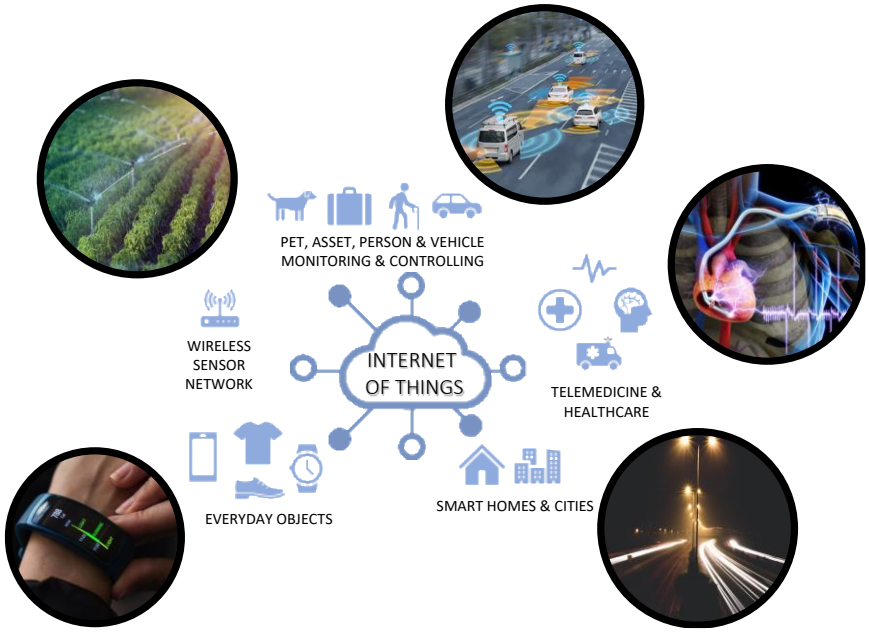

Figure 1.1: The Internet of Things can potentially be integrated in every aspect of the human life.

IoT-powered smart cities aim at improving the quality of life of their populations in a variety of ways, through measures that promote eco-friendly, sustainable environments and the delivery of healthcare services to citizens at home and around the city [4], public and environmental health surveillance, crisis management applications [5] and the improvement of the performance of public services, as transport, traffic, energy and health. Smart homes and buildings are one of the essential building blocks of smart cities [6,7], while smart grids focus mainly on energy saving for homes and businesses based on the power grid to collect usage data from appliances. Smart industry is expected to revolutionize manufacturing as we know it [8], while smart sensor networks enable precision agriculture and smart farming, increasing productivity while reducing resources consumption (water, light, pesticides etc.) [9–11].

Medical care represents one of the most attractive application areas for Internet of Things. IoT is expected to transform healthcare industry by increasing efficiency, lowering costs and put the focus back on better patient care [12]. Internet of Things has been widely applied to interconnect available resources and provide reliable, effective and smart healthcare service to the elderly, patients with chronic conditions and those that require consistent supervision [13]. One good example of patient

based IoT are the widely commercialized health monitoring smart watches. These devices present different monitoring functionalities depending on the patient necessities, i.e. step count, activity level, body temperature, hearth rate, blood pressure, posture, eating and sleeping behaviour [14]. Moreover, the ones dedicated to special needs patients have typically the additional feature of geo-locating the patient and alerting the caregivers. In some cases, for example seizures and tremors in epilepsy patients [15,16], the constant monitoring can be a crucial factor in treatment and prevention, and therefore improve to quality of life (Figure 1.2).

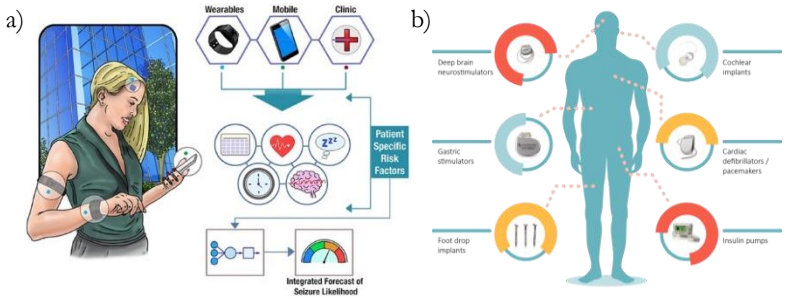

Figure 1.2: a) Data from clinical notes, wearable devices, and mobile apps can be combined to obtain a deeper understanding of patient-specific risk factors and to model seizure likelihood for epilepsy patients [16]. b) Examples of implantable medical devices.

This aspect is even more crucial for implantable medical devices (some examples in Figure 1.2b), since they can be used to diagnose, prevent, and cure diseases *in vivo* by performing tasks like drug releasing, monitor health parameters, or life-saving tasks as insulin-injections or heart defibrillations.

Especially for implantable or wearable applications (some examples of which can be observed in Figure 1.3), which need to be in constant contact with human bodies, it is crucial that these devices can adapt to the physical motion in order to have a seamless integration between body and device. The human physical sensation is maintained under large deformations; thus, softness and compliance have been the main technological obstacle in fabrication of sensory devices. For the past two decades, the research on stretchable physical sensors have made great technological advances, and have been employed in various applications such as electronic skin, haptic devices, bionics, wearable/implantable healthcare sensors, etc. The research field that deals with these soft devices as actuators, stretchable electronics, sensors, wearables, implantables, and e-skins is called soft robotics.

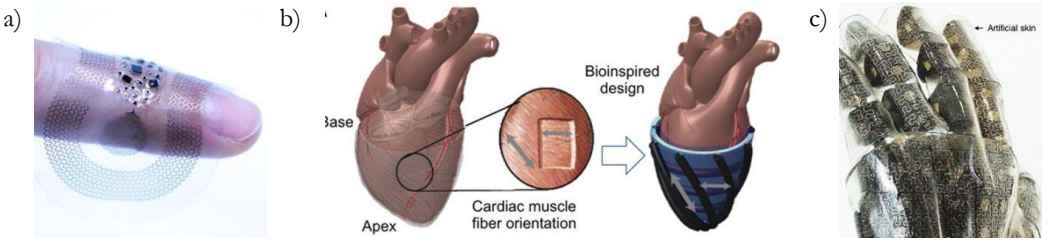

Figure 1.3: Some examples of soft devices. a) Wearable and wireless sensors designed to monitor health conditions of premature babies. b) Conformal soft robotic sleeve that can support heart function, from [17], c) Smart artificial skin covering a prosthetic hand [18].

Soft robotics

Soft Robotics is the branch of robotics that deals with the design, development, and construction of soft, flexible robots with movements and mechanical characteristics similar to that of the biological organisms [19–21]. Since it offers unprecedented solutions for applications involving smooth touches, soft robotics is receiving a rapidly growing interest for applications requiring close interactions with humans [19,22–24], biomedical active wearable and implantable devices [24–27] smart sensor networks in precision agriculture [28–31] and manipulating and grasping fragile objects.

Conventional robotics employs rigid materials to fabricate precise robotic systems, easy to model and with limited degrees of freedom determined by rigid joints [32]. The advantages of this approach are precision, speed and robustness, capacity to bear high loads and large mechanical work: all important features for repetitive tasks as, for example, factory assembly lines. Conventional robots are not capable to adapt to changing conditions within the tasks they are designed for, or to operate in fully unstructured environments [33]. In contrast, natural organisms exploit soft structures to move efficiently in complex natural environments [34]. Soft robotics aims to equip robots with these skills by providing them with capabilities that are based on material properties and body morphology, focusing on the mechanical qualities and on the integration of materials, structures, and software in the same way that natural organisms integrate neural and mechanical controls. In Figure 1.4 is represented briefly the concept of bioinspired robotics and soft robotics [35,36] using a popular culture reference, and the real-life application of the same concept [37].

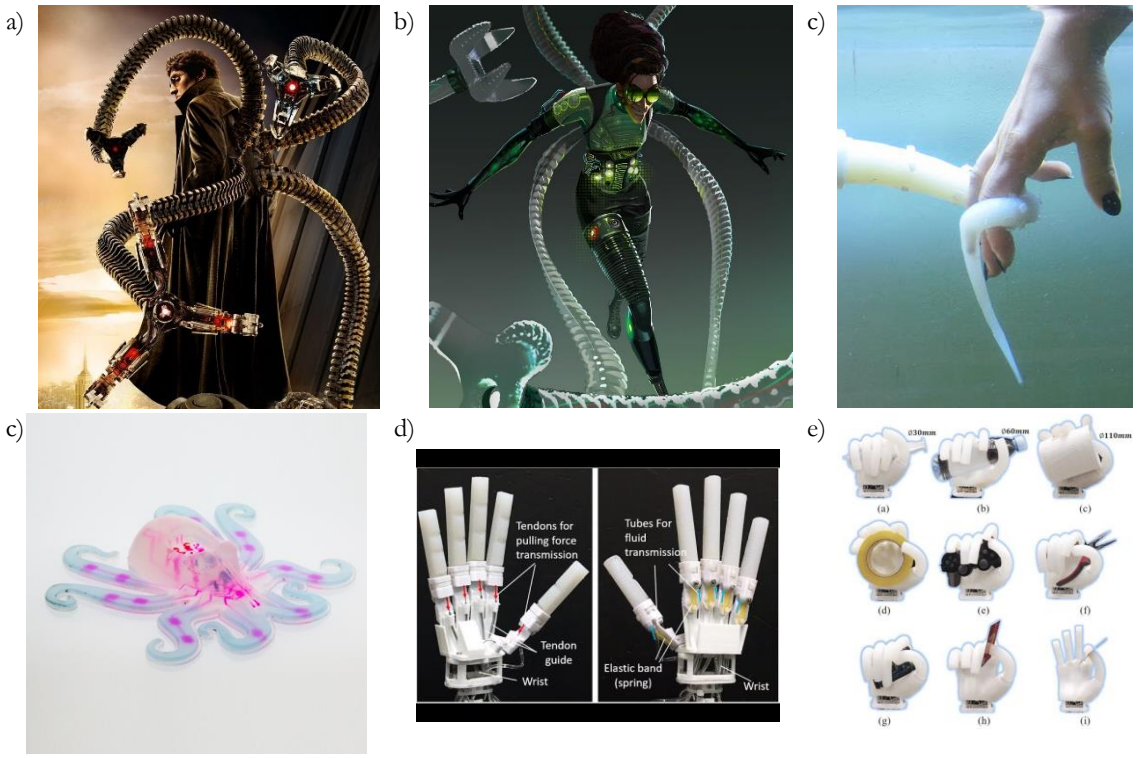

Figure 1.4: Nature inspired robotic arms are the main weapon of a popular antagonist in the comic and movie series Spiderman. a) The original character, Dr. Octopus, is equipped with hard robotic tentacles with many rigid joints that allow them to achieve several degrees of freedom. b) An alternative and modern version of the character, Dr. Olivia Octavius, is equipped with soft robotic arms. c) An actual soft robotic actuator based on octopus-like tentacle, it is soft, flexible, and continuous. The arm is able to elongate, shorten, and bend in any direction, as well as to stiffen selectively in different parts [37]. Images d), e) and f) contain examples of soft robot prototypes developed in the last few years. d) An entirely soft, autonomous robot based on an integrated design and fabrication strategy, that allowed untethered operations [38]. e),f) Soft robotic hand with fluidic and tendon driven actuators [39].

In this framework mechanical properties as conformability, flexibility and stretchability are fundamental features for the materials in order to be suitable for the selected application [40,41], as well as the absence of compliance matching [42] causes surface damages and mechanical limitation, due to interfacial stress concentration and the non-uniform distribution of internal loads. Most of the materials constituent complex living organisms, such as skin and muscle tissue, have

a modulus on the order of 10^2–10^9Pa (Figure 1.5) [43][40]. Advances in soft materials (e.g., elastomers, hydrogels, electroactive polymers, etc.) and advanced manufacturing technologies (e.g., 3D printing) are fuelling the rapid development of soft robotics [44], as well as the progressed in science and technology of smart materials [42], i.e. materials that change their behaviour as a response to specific stimulus (e.g. magnetic and electric fields, stress, acoustic waves, temperature)[45].

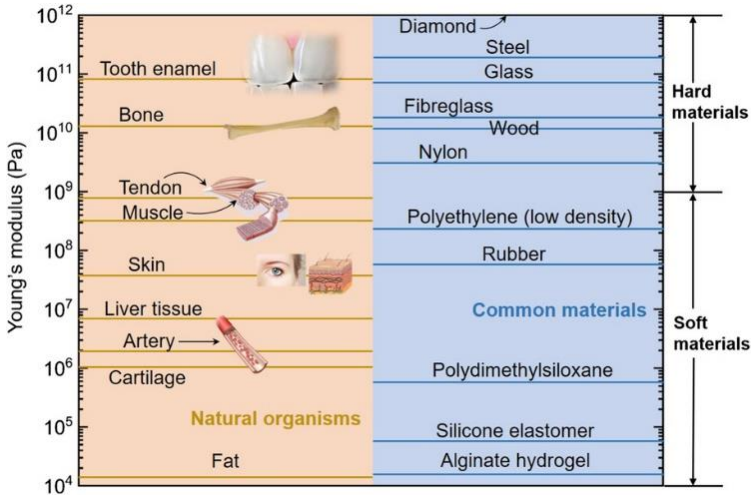

Figure 1.5: Young's modulus of some biological and engineering materials. The Young modulus of soft and hard materials is approximately in order of 104 ~109 Pa and 109 ~1012 Pa, respectively. Image from [44]

Soft robotic devices require portability, control, and design flexibility [46] of all of their elements: soft actuators and sensors, power supply, energy storage and wireless communication. While 3D printing and the miniaturization of the electronic integrated circuits following Moore's law are precious technologies for reaching the desired design flexibility and portability, a sustainable power source is still a key technical challenge for practical applications of soft robots. Autonomous robotics can potentially benefit from renewable resources, by harvesting energy from the environment. A variety of energy sources are available including mechanical (vibrations, human motion, wind/fluid motion), electromagnetic (radio frequency, solar), and thermodynamic (chemical or thermal energy).

1.2 MOTIVATIONS AND AIM OF THE THESIS

Many of IoT and soft robotics applications rely on autonomous devices with energy production and storage, mechanosensing, and data processing capabilities [25][26][47][48]. In these frameworks the sensing and the harnessing of mechanical energy present in the ambient can represent an enabling factor for the use of wearable or implantable devices [49–52]. In this context bio-mechanical energy can be a quantity to be measured [26], but it can also represent a viable source of power, in particular for wearable or implantable devices [27].

Soft electro-mechanical transducers are receiving a widespread interest for both sensing and energy harvesting applications. In the last decade the research on novel nanocomposites based on polymeric nanocomposites has been very active, and many materials with diverse and innovative compositions and architectures have been fabricated and reported. Nevertheless, there are still some critical aspects that affect this research field, in particular for what regards their characterization.

Despite the widespread interest that these smart materials are attracting, the methods commonly used to characterize them are frequently qualitative and unreliable. Moreover, the description of the testing conditions is often incomplete, so that the data cannot be reproduced by other researchers, and the performances of the various materials cannot be compared. The knowledge of these properties is necessary for a complete understanding of the material working principle, for the prediction of its effective properties aimed at optimization purposes, and for the selection of the right material in device applications. In this framework the development of a quantitative and reliable measurement technique is crucial in order to to assess these materials figure of merit, their reliability and reproducibility.

During my PhD I worked on the development of a reliable and quantitative measurement instrument, and on the development of some novel soft electro-mechanical transducers based on different physical electro-transduction effects.

1.3 THESIS OUTLINE

This thesis work will be focused on the fabrication and characterization of materials with electro-mechanical conversion capabilities, for applications in both energy harvesting and pressure and strain sensing. Four different kinds of materials were

developed and tested, three active materials based on piezoelectric $BaTiO_3$ nanoparticles on different polymeric matrixes, that can be applied both as sensors and as energy harvesters, and a passive material based on a piezoresistive polymer/metal nanocomposite, which can be applied as a strain sensor. For the characterization of such nanocomposites, a custom experimental set-up to measure the piezoelectric coefficients in a wide frequency range was developed and validated.

In Chapter 2 the different mechanisms that allow electro-mechanical conversion are presented. After a brief introduction on the concept, the principal classes of transducers used in this thesis work are discussed in detail, presenting their conversion mechanism and the mathematical formalism used to describe their behaviour, the principal materials that belong to these classes, and the typical solutions conventionally used to make them compatible with soft systems.

In Chapter 3 is examined the state-of-the-art for the characterization of piezoelectric materials, in particular soft nanocomposites. After a brief review of the principal techniques and how they are applied in current research, the limitations of the current approach to piezoelectric nanocomposite characterization are discussed. In the rest of the Chapter the experimental set-up designed and developed for the robust and reproducible characterization of these materials is presented and described in detail, with specifics regarding the hardware and electronic design, the calibration of the instrument and the validation on commercial standard samples.

In Chapter 4 is presented a piezoresistive sensor based on an elastomer/metal nanocomposite, developed in the framework of a project funded by Fondazione Cariplo and Regione Lombardia (Smart Valves based on Active Soft Materials – ASSIST), in collaboration with Politecnico di Milano and two industrial partners, Dolphin Fluidics s.r.l and WISE s.r.l.

Section 4.1 describes the optimization of a fabrication protocol targeting the production of polydimethylsiloxane (PDMS) substrates with reproducible mechanical properties.

In Section 4.2 the Supersonic Cluster Beam Deposition technique, used to produce nanostructured electrodes based on cluster-assembled gold thin films onto the PDMS, is presented, and the optimization of the fabrication protocol with this technique to produce nanostructured films with reproducible mechanical and electrical characteristics is reported.

In Section 4.3 the electro-mechanical tests of such nanocomposites are discussed, and a brief mock-up of the final application of the project is presented.

In Chapter 5 different piezoelectric materials based on Barium Titanate nanoparticles are reported, fabricated in the framework of a collaboration with University of Bologna. Section 5.1 reports the procedure used for the fabrication of surface functionalized $BaTiO_3$ nanoparticles, for improved dispersion in lipophilic and hydrophilic media.

In Section 5.2 a smart material engineered to combine piezoelectric and piezoionic effects is presented. The fabrication of this material, based on an ionogel matrix with embedded $BaTiO_3$ nanoparticles, and its electro-mechanical characterization with a prototype of the instrument presented in Chapter 3, are described.

In Section 5.3 a piezoelectric nanocomposite based on PDMS and incorporating lipophilic nanoparticles is presented. The nanocomposite synthesis, polarization procedure and its full characterization using the instrument presented in Chapter 3 are presented and discussed.

In Section 5.4 the polarization and the electro-mechanical characterization of novel 3D printed piezoelectric resins, fabricated in the framework of a collaboration including also the INANNOMAT research group, from Universitad de Càdiz, are reported. The research on this topic is still on-going.

Electrodes are an essential aspect during the fabrication of soft piezoelectric materials, since they collect the generated charges from the surface. Since they guarantee a high surface-area, electrodes fabricated by Supersonic Cluster Beam Deposition are supposed to increase the efficiency of charge collection. In Section 5.5 the experiments performed on the efficiency of such electrodes on the materials presented in the previous sections are discussed.

In the final Chapter the conclusions and the perspectives emerging from this work are discussed.

2. ELECTRO-MECHANICAL TRANSDUCTION

Electro-mechanical transducers are all the numerous devices that are able to link the electrical and mechanical energy domains, from the firsts electrostatic generators, loudspeakers and microphones (Figure 2.1) to the most advanced applications described in the Introduction.

Depending on the application some transduction mechanisms are more suitable than others. For instance, in order to convert mechanical energy into an electrical one a direct and efficient conversion is required, which can be achieved by piezoelectric, triboelectric and electromagnetic or electrostatic induction transducers [53]. On the other hand, for sensing applications, i.e. to read and track a change in strain or pressure, the requirements are reliability, high precision and low energy consumption, which can be also achieved by the use of capacitive, piezoresistive, and piezoionic transducers.

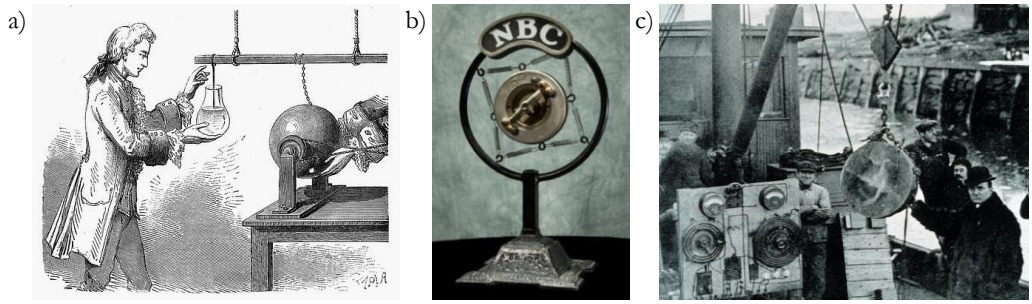

Figure 2.1: Some examples of historical electromechanical transducers. a) The glass globe friction machine, common in the 18th century, was one of the firsts electrostatic generators. It exploits the triboelectric effect between glass and cloth to accumulate static charges in an electrical conductor. b) The carbon microphone, developed at the end of the 19th century, used the piezoresistive effect of a layer of carbon granules to reproduce electrically the sound signal. c) The Fessenden Oscillator, developed between 1912 and 1914, was the first functioning sonar device. It works similarly to a coil loudspeaker to produce sound waves in water. Fessenden oscillators were later replaced with piezoelectric oscillators, due to their higher functioning frequencies.

The prefix piezo comes from ancient greek (πιέζειν, piezein) and means pressure, it therefore represents the mechanical portion of the transduction. Depending on the transduction mechanism, the electrical counterpart may have different names. In Figure 2.2 can be observed some examples. In piezoresistive materials (Figure 2.2a) the mechanical strain induces a change in resistivity, while in piezocapacitive materials (Figure 2.2b) the geometrical variation of the distance between the two electrodes alters the electrical capacitance. Something different happens in piezoelectric materials, where the mechanical stress induces a change in the potential (Figure 2.2c) caused by the re-arrangement of electrical dipoles, and in piezoionic materials (Figure 2.2d), where the potential is caused by the movement of the charged ions.

This chapter is focused on three classes of transducers: piezoelectric, piezoresistive and piezoionic materials. An interesting effect that was not used during the work of the present thesis is the triboelectric effect. The triboelectric effect is related to a contact electrification due to the separation of two different materials that were previously in contact (Figure 2.2e), and it is the origin of most of the static electricity in everyday life, even though its functioning is yet to be fully explained [54].

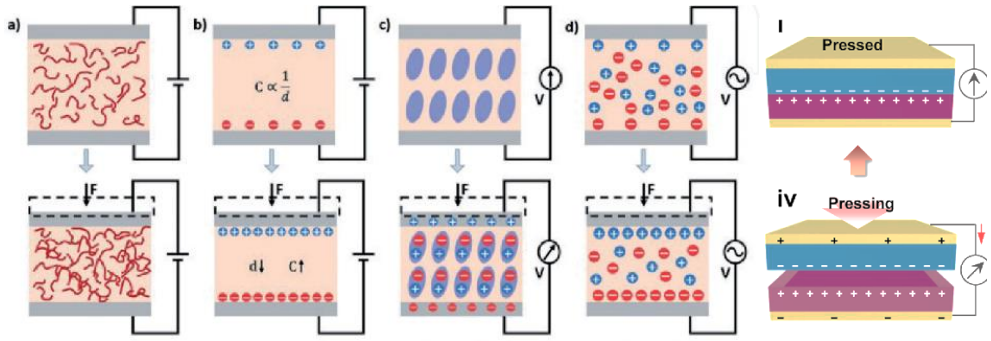

a) Piezoresistive b) Piezocapacitive c) Piezoelectric d) Piezoionic e) Triboelectric

Figure 2.2: Different mechanisms for electro-mechanical transduction (images from [55] and [56]).

After a theoretical introduction on the mechanisms and the principles that allow the electro-mechanical conversion the most common solutions necessary to integrate these materials with soft systems will be introduced, and the state of the art regarding this type of materials will be discussed.

2.1 PIEZOELECTRIC EFFECT

The piezoelectric effect was discovered in 1880 by Pierre and Jacques Curie. By analogy with temperature-induced charges in pyroelectric crystals, they observed an induced net polarization when certain crystals were perturbed mechanically, which, since they were also dielectric, resulted in an electric charge accumulated on the crystal surfaces. In 1881 Gabriel Lipmann predicted from thermodynamic principles the reversibility of the piezoelectric effect, i.e. a strain is induced in the material when subjected to an external electrical field; this prediction was confirmed experimentally by the Curie brothers. In 1920 Joseph Valasek discovered that the spontaneous electrical polarization of Rochelle Salt can be oriented by means of an electrical field. These materials exhibit a hysteresis cycle of polarization versus electrical field, and were called ferroelectrics, in analogy to ferromagnets.

Many different materials, both natural and synthetic, exhibit piezoelectric and ferroelectric properties. The firsts discovered and studied were crystalline materials (quartz, Rochelle salt, topaz, tourmaline and cane sugar), but over the next few decades many different materials were developed and studied. In particular in 1945 it was discovered that certain artificial polycrystalline anisotropic ceramics with high dielectric constant, as Barium Titanate, were ferroelectric, so it was possible to orient the electrical dipoles within the different grains, producing a ceramic material that acted very similar to a single crystal [57]. This discovery revived the interest in research and development of piezoelectric devices since it provided a new way for the fabrication and manufacturing of such materials with improved performances. In 1969 Heiji Kawai discovered the first and only case of piezoelectricity occurring in a semi-crystalline polymer, poly (vinylidene fluoride) [58], which opened up a wide range of new possible applications.

Piezoelectric materials have been exploited as electro-mechanical transducers for many applications. The first application they were used for was the quartz oscillator, used as time reference in quartz watches, but after the Second World War the piezoelectric effect evolved from a laboratory curiosity to a multimillion dollar industry with applications ranging from underwater sonars and medical imaging systems to car accelerometers, micro-balances, igniters, up to more advanced integrated microelectromechanical systems (MEMS) [59,60] used in the automotive industry, smartphones, and many scientifical instrumental techniques [61]. More recently they have been used as sensors, actuators, and energy harvesters in IoT and soft robotic devices, as the ones presented in the Introduction.

2.1.1 Theory and constants

Real piezoelectric materials involve mechanical and electrical dissipation, along with strong non-linear behaviour, hysteresis effects, temporal instability, and various magnetic electrical and mechanical interactions. For example, piezoelectric ceramics, of major importance in applications, involve ferroelectric domains, which yield to strong nonlinear effects [62]. Neglecting dissipation and non-linear effects is possible to obtain from thermodynamic considerations a linear piezoelectric theory, of which the results are presented below.

The piezoelectric effect can be formalized as a linear and reversible relationship between the induced electric displacement D and the applied mechanical stress σ. A piezoelectric coefficient tensor d_{ij} can be defined by the relationship:

$$D_i = \epsilon_0 \epsilon_{ij}^{\sigma} E_i + \sum_j \sigma_{jj} d_{ij}$$

where D is the electric displacement, E is the electric field, σ is the stress tensor, ϵ_0 is the vacuum permittivity and ϵ_{ij}^{σ} is the relative medium permittivity at a given σ.

The two quantities more suitable to describe the performance of a piezoelectric material are the piezoelectric coefficient d_{ij} and the piezoelectric voltage constant g_{ij}, both 3x6 matrixes of which the coefficients can be defined as:

	Direct effect	Converse effect
Piezoelectric charge coefficient	$d_{ij} = \left(\frac{\partial D_i}{\partial \sigma_j}\right)_E$	$d_{ij} = \left(\frac{\partial S_j}{\partial E_i}\right)_\sigma$
Piezoelectric voltage coefficient	$g_{ij} = \left(\frac{\partial E_i}{\partial \sigma_j}\right)_D$	$g_{ij} = \left(\frac{\partial S_j}{\partial D_i}\right)_\sigma$

These piezoelectric constants are defined as partial derivatives evaluated at constant stress (subscript σ), constant electrical field (subscript E), constant electrical displacement (subscript D). These conditions can be regarded as "*mechanically free*", "*short circuit*" and "*open circuit*" respectively.

Other quantities that determine the performance degree of a piezoelectric material are lifetime and maximum operating temperature, along with mechanical properties, as the Young's modulus, stiffness, and fragility.

2.1.2 Conversion Mechanism

A necessary condition for piezoelectricity is the absence of a centre of symmetry in the electronic structure of the materials. This structural property appears evident in crystals, where the ions relative positions are fixed, as can be observed in Figure 2.3a,b. Out of the 21 non-centrosymmetric crystal classes only one is non-piezoelectric (432), because the charges developed along one of the polar axes cancel each other out. Among these 20 classes, ten groups possess a unique polar axis. These materials contain therefore a built-in polarization, that manifests itself in temperature induced changes of the total dipole moment of the unit cell in absence of an applied field. These materials are called *pyroelectric*, as they respond to temperature changes with a change in the intrinsic dipole moment. Their polarization direction is usually constant, but for some of those materials it can be reversed by means of an external electric field [63]. Those materials are said to be ferroelectric.

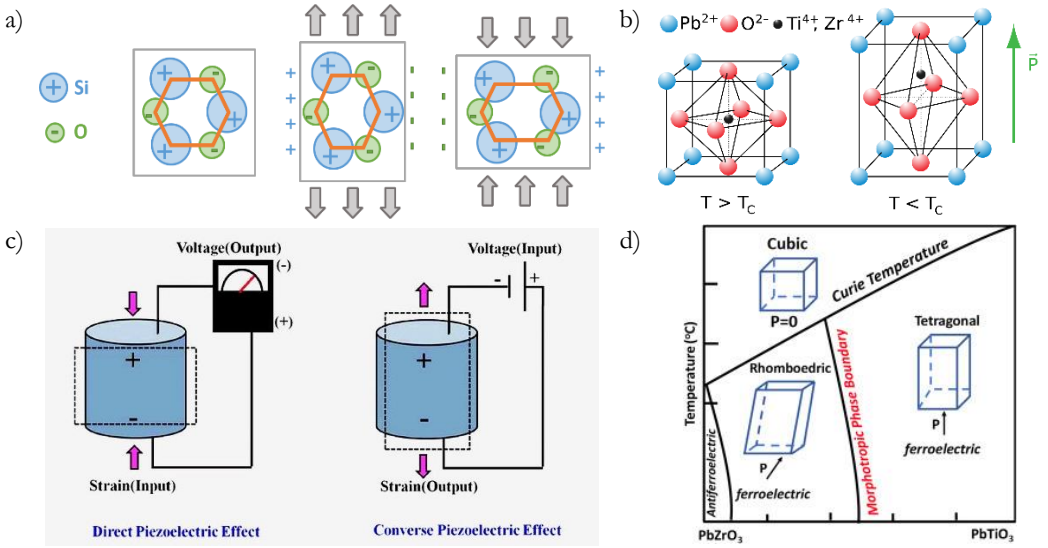

Figure 2.3: a) Piezoelectric effect in a quartz crystal cell. When the crystal is stress or strained the ions find themselves in new positions and as a result a net charge accumulates on opposite surfaces. b) Lead Zirconate Titanate has a tetragonal polar structure that provides it of a polar axis. c) Piezoelectric effect and converse piezoelectric effect schematic functioning. d) Phase diagram of (PZT) showing crystallite structures in different regions. Image from [64].

Typically, ferroelectric materials exhibit their spontaneous polarization below a phase transition temperature called Curie temperature T_C. At this temperature they undergo a phase transition from a low temperature ferroelectric phase to a high

temperature paraelectric phase (Figure 2.3d). The paraelectric phase is more symmetrical than the ferroelectric one and is rarely polar. For the majority of ferroelectric materials, the crystal structure becomes centrosymmetric in their paraelectric phase, therefore they cease to be piezoelectric [65]. Domains - chemically identical areas with different orientation of the electric polarization - naturally occur in ferroelectric crystals, since they minimize the free energy.

An important class of ferroelectric materials are piezoelectric ceramics, discovered in the early 1940's. Piezoelectric ceramics are polycrystalline materials composed of randomly oriented crystallite grains (Figure 2.4a). The piezoelectric responses of the crystallites are usually averaged out on the entire sample, but some of these piezoelectric ceramics are ferroelectric, so the polarization axes can be aligned in a roughly uniform direction, by means of a strong electric field, usually at high temperatures. This process, called poling, is unable to reorient grains, but can reorient polarization domains within individual grains (Figure 2.4b) in the field direction. Even if many domains are still present, a net polarization is developed through the material, and this polarization is enhanced with the degree of domains reorientation in the crystal. One of the consequences of domain-wall reorientation is the occurrence of the ferroelectric hysteresis loop, which measures the degree of re-orientation of the domains (Figure 2.4c).

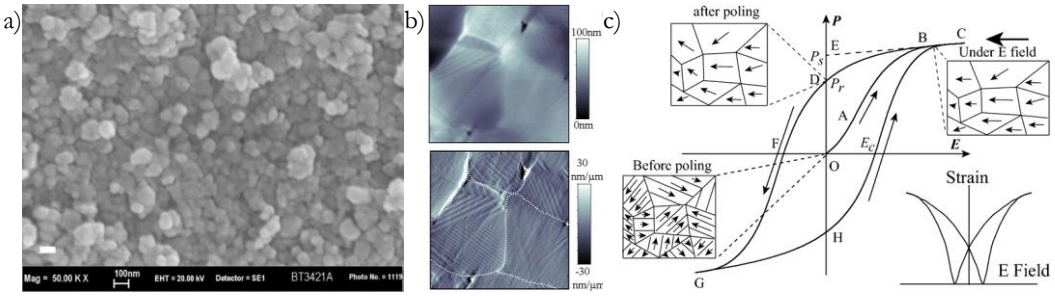

Figure 2.4: a) Microstructure of ferroelectric ceramics. SEM image of a Barium Titanate sample with average grain size of 50nm. Image from [66]. b) A 10 μm × 10 μm PFM scan of ferroelectric ceramic topography (up), and its derivative (down). In white are highlighted the borders between ceramic grains, while the ferroelectric domains are visible within the single grains. Image from [67]. c) Ferroelectric hysteresis loop and domains orientation. Image from [68].

The piezoelectric effect in real materials has different contributions. The first and *intrinsic* contribution is the one discussed at the beginning of this chapter, that originates in the field-induced lattice deformation. The *extrinsic* contributions are

defined as all the other contributions, such as the displacement of domain walls and interphase boundaries [69]. The total macroscopic effect depends on domains' density, their orientation, polarization, the strain relationship within the domains and, most importantly, the domain walls mobility [70]. The extrinsic piezoelectric response results principally from non-180° (for example 90°, see Figure 2.5b for reference) domain wall movements driven by the application of an external electric field or a mechanical stress. In ceramics the domains form under clamped conditions, so the domain-twinning depends on the grain size, in particular it was found that in fine-grained ceramics a lamellar structure is favoured, while in coarse-grained ceramics the minimum of free energy is reached with a banded lamellar structure (Figure 2.5b). This different domain structure affects the domain motion, and therefore the extrinsic response [71]. Microstructural investigations showed that poled ferroelectric ceramics contain a large number of non-180° domain boundaries, which strongly affect their electromechanical behaviour.

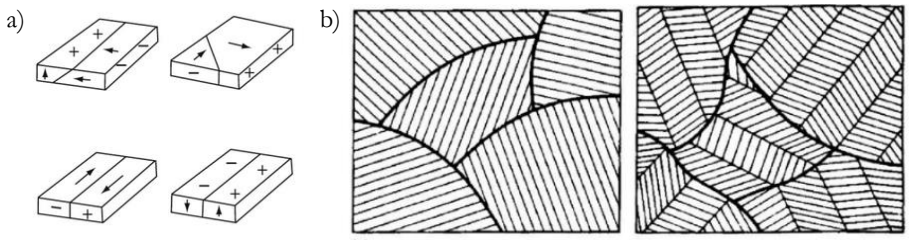

Figure 2.5: a) Domain configurations in tetragonal phase. On the left 90° domain walls, on the right 180° domain walls. b) Lamellar structure and banded lamellar structure of ferroelectric domains.

These extrinsic mechanisms operate simultaneously and can contribute up to the 70% of the total material response, as well as give rise to most of the non-linear effects, such as weak field frequency dispersion, hysteresis, and non-linear piezoelectric responses [72]. Some examples of linear and non-linear behaviours can be observed in Figure 2.6.

The theoretical and microscopical understanding of the mechanisms that links domain walls and interphases displacement with the extrinsic contribution is still not complete and presents a great challenge [69][71].

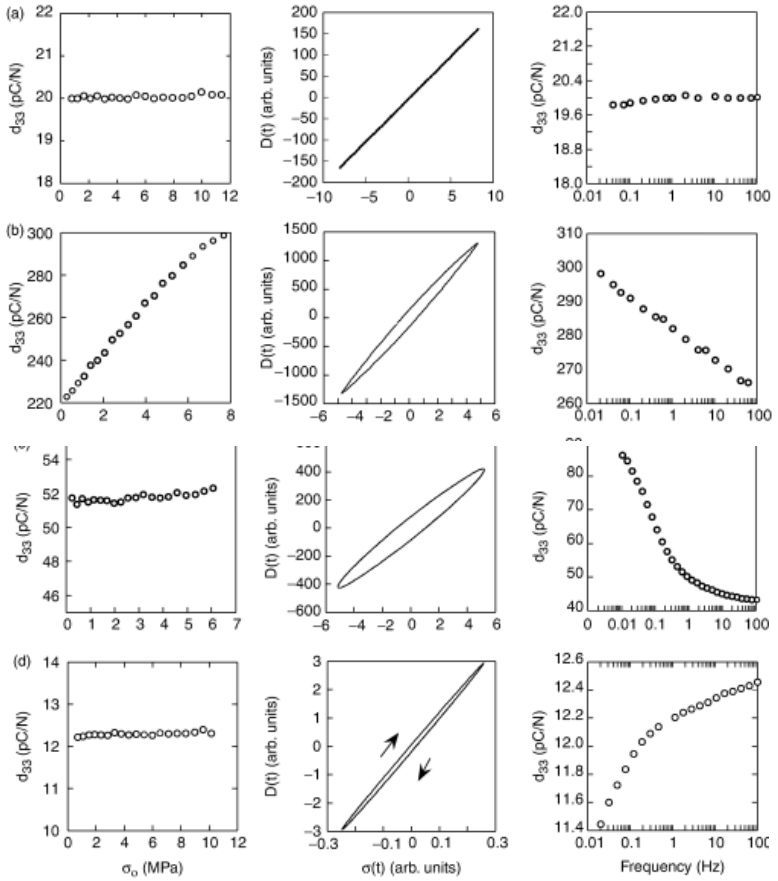

Figure 2.6: Non-linear piezoelectric behaviour of different ceramic samples. The first row ($SrBi_4Ti_4O_{15}$) is a reference for an ideal linear behaviour. Dynamic stress dependence on the left, hysteresis in the middle and frequency dispersion on the right. Images from [69].

2.1.3 Soft piezoelectric materials

Piezoelectric materials are a promising solution for mechanical energy conversion via electro-mechanical coupling. Despite the high piezoelectric properties, some of their limitations, such as rigidity, brittleness, toxicity, and lack of design flexibility limit the range of their energy-related applications, since the choice of a particular piezoelectric material for a specific application depends on various parameters such as acoustic impedance, application frequency, mechanical properties, and available volume.

For applications in the framework of soft robotics, however, portability, flexibility and stretchability of the devices are fundamental features [40,41]. The crystalline and ceramic piezoelectric materials described in the previous Section present high

piezoelectric outputs and high resistance to stress in the polarization direction. However, they are brittle, fragile, and non-resistant to laminar stress and strains. They respond well to high frequencies, especially near to their resonant frequency, and their Young's modulus is in usually the order of 10^{10}–10^{11}Pa. However, most of the materials constituent complex living organisms, such as skin and muscle tissue, have a modulus on the order of 10^{2}–10^{9}Pa [43][73]. The mechanical mismatch between the common piezoelectric materials and biomechanical soft environments raises several issues linked to the absence of compliance matching**,** such as surface damages and mechanical limitation. For applications in biomedical environments softer materials are needed, in order to minimize the interfacial stress concentration and to distribute internal loads.

Piezoelectric polymers present many advantages in comparison with classical crystal or piezoelectric ceramics, especially from an electromechanical point of view, as it is possible to control their mechanical properties, as flexibility and deformability. Piezoelectric polymers also have a low acoustic impedance, and they can have various electrical properties and wider bandwidths. The drawbacks of piezoelectric polymers are a low electro-mechanical coupling coefficient and the fact that they are unstable at high temperatures.

2.1.3.1 PVDF

The piezoelectric polymeric technology has been dominated for many years by ferroelectric polymers of the polyvinylidene fluoride family (PVDF) and its co-polymers with trifluoroethylene (PVDF-TrFE). The piezoelectric activity of this polymer was discovered in 1969 by Heiji Kawai [58], followed by the finding of its pyroelectricity by Bergman et al. [74] and by Nakamura and Wada [75]. Later, also ferroelectricity was confirmed in this polymer family, as discussed in the Lovinger's review of 1983 [76].

PVDF has a Young's modulus of 2.7GPa[77] and a piezoelectric constant of 30pC/N [78]. In comparison with ceramics the performance is much smaller, but the advantages of piezoelectric polymers are flexibility, small acoustic impedance and robustness.

The piezoelectricity of PVDF arises from the strong molecular dipoles in its polymeric chain. In the bulk form PVDF is semi-crystalline (Figure 2.7a), i.e. it consists in randomly oriented ferroelectric crystallites dispersed within an amorphous region. PVDF's crystallite have four different phases, of which one is apolar (the α-phase), while the other three are polar. In particular in the β-phase the

dipoles are all aligned along the backbone (Figure 2.7b). Since the polymer is ferroelectric, it is possible to orient the dipoles of the crystalline phases, hence, to obtain an overall polarization of PVDF. Piezoelectricity in bulk PVDF arises from variations in dipole density, so it is called *dipole density piezoelectricity*.

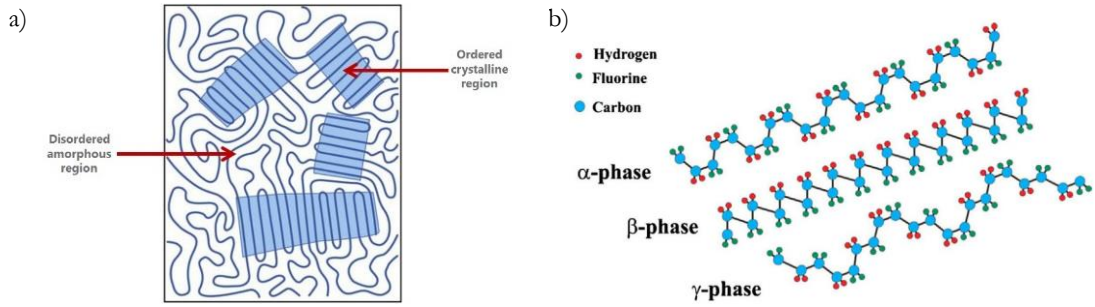

Figure 2.7: a) PVDF phases along the polymer backbone. The β-phase is ferroelectric because the strong molecular dipoles are aligned. b) Schematic of semi-crystalline polymer.

2.1.3.2 Piezoelectrects

Piezoelectrects, namely voided charged polymers [61], are polymers that contain internal gas voids, for example cellular polypropylene or Parylene-C (Figure 2.8). It is possible to charge the internal polymer surfaces by applying a large electrical field across the polymer film. The field ionizes the gas molecules inside the voids and opposite charges are accelerated and implanted on each side of the voids. Those embedded dipoles respond as piezoelectric materials to external fields or applied forces, but instead of ion or domain displacement, the working mechanism is the deformation of the charged voids.

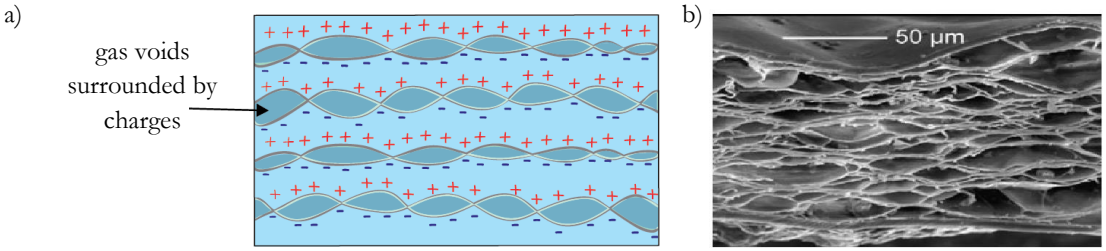

Figure 2.8: a) Piezoelectrects, or voided charged polymers, are polymers that contain internal gas voids. The piezoelectric effect is due to electrical charges implanted in the polymer material surrounding the voids b) Parylene-C internal structure's SEM image. Parylene-C is a piezoelectrect.

Piezoelectrects can have a high transversal piezoelectric coefficient, that can span from 20 to 1200pC/N depending on shape and density of the voids [61], although they lack in thermal stability, they age at high deformations, and they don't show any longitudinal piezoelectric effect [79–82]. Another dominant phenomenon in voided charged polymers is the dependence on the frequency of the applied force or electrical field. This dependence is present in other piezoelectric materials, but it is not as influential as in voided charged polymers [61].

2.1.3.3 Piezoelectric nanocomposites

A widely explored solution to obtain flexible and stretchable piezoelectric materials is to combine the mechanical characteristics of a polymeric matrix with the electro-mechanical conversion property of piezoelectric nanoparticles [61][83][84]. This can be achieved by developing composite piezoelectric materials through dispersing nanosized ceramics in a polymer matrix. The properties of composites depend on the connectivity of different phases. Many theoretical investigations on binary systems have been performed with regard to the dielectric constant, piezoelectric constant, and the elastic constant [85–88].

They proposed a two-phase model as shown in Figure 2.9, composed of a non-piezoelectric continuous phase (phase 1) and a piezoelectric phase (phase 2, which can be spherical [88], ellipsoidal [87], or cubic [85]), where the apparent piezoelectric constants can be expressed as:

Apparent piezoelectric charge coefficient $$d = \Phi \mathrm{L}_\sigma L_E d_2$$

Apparent piezoelectric voltage coefficient $$\mathrm{g} = \Phi \mathrm{L}_\sigma L_D g_2$$

Where Φ is the volume fraction of the piezoelectric phase, L_σ, L_E and L_D are the local field coefficients ($L_E=E_2/E$, where E_2 is the field produced in the piezoelectric phase), and d_2 is the piezoelectric coefficient of the piezoelectric particle. Yamada also inserted a poling ratio factor α. By deriving the local field coefficient from the permittivity constants and the connectivity of the piezoelectric phase, it is possible to write an expression for the piezoelectric constant and the mechanical constant for the composite system. The electrical and mechanical interactions expressed by two kinds of local field coefficients play important roles in the absolute values of the apparent piezoelectric constants and their frequency and temperature dependences, which are therefore the result of the inter-play between the different

phases of the nanocomposite material. In Figure 2.9c the results from a finite elmenet analysis simulations made on this class of materials are presented. The images show the calculated piezopotential for tensile strain of 0.33% in the x-axis is generated across the top and bottom sides of the PDMS matrix by the piezoelectric nanoparticles [89].

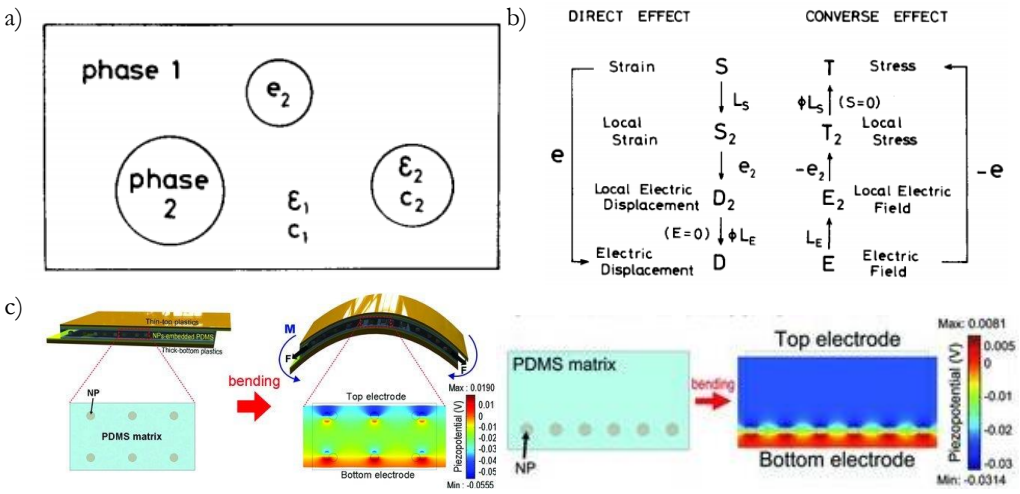

Figure 2.9: a) Two-phase model of a piezoelectric composite material. b) Piezoelectric effect for a two-phase system. Images from [88]. c) Simulation model for a piezoelectric polymer nanocomposite with the calculated piezopotential for dispersed and non-dispersed nanoparticles [89].

In the last few years, the scientific community has developed an increasing interest in polymer piezoelectric materials. Many different composites have been synthetized and characterized. In Appendix A is reported the state of the art for piezoelectric polymeric nanocomposites, both as formulations and measured performances.

2.2 PIEZORESISTIVE

The piezoresistive effect was first discovered in 1856, when Lord Kelvin found that the electrical resistivity of copper and iron changes when a mechanical strain is applied. In 1935, Cookson first applied the term piezoresistance to the change in conductivity with stress, as distinct from the relative change of resistance, which includes both geometric and material property dependent changes. Later, in 1954, Charles S. Smith discovered that the piezoresistive effect regarded also semiconductors such as Silicon and Germanium [90], and that for this kind of materials the piezoresistive effect can be several magnitude orders larger than in

metals. Furthermore, their sensitivity can be increased further through suitable doping. Technological advances in the fabrication of ICs including doping, etching, and thin film deposition methods, have allowed significant improvements in piezoresistive device sensitivity, resolution, bandwidth, and miniaturization [91]. At the same time a new class of piezoresistive composites, consisting of conducting nanoparticles dispersed in an insulating matrix, emerged. These polymer/metal nanocomposites can incorporate a variety of conductive fillers (carbon nanotubes, graphene, metal nanowires), and have the potential to fulfil the requirements of soft sensors.

Due to their high sensitivity and linearity, piezoresistive sensors have been extensively used in commercial micro-electromechanical systems (MEMS) devices and in macro-scale single sensors and sensor arrays as accelerometers, pressure sensors, strain-gauges, displacement sensors, flow sensors, torque sensors [92]. They have been very pervasive in different fields (e.g. biological and biomedical applications, harsh environments, heavy industry), and the recent progresses in the development of flexible and stretchable piezoresistive materials make them promising candidates for the wide range of wearable and implantable applications described in the Introduction, such as electronic skins for tactile soft robots.

2.2.1 Conversion Mechanism - crystals

In a bulk material the resistance is connected to the resistivity by the formula $R = \rho \frac{l}{A}$, where l is the length, A is the surface area and ρ is the resistivity. If the material is subjected to a tensile stress the material will deform, reaching a length of $l + \Delta l$. Because of the elastic properties the surface area will shrink accordingly to the Poisson's ratio $v = -\frac{\epsilon_{m,trasv}}{\epsilon_{m,long}}$ it will be reduced from $A = \omega^2$ to $A' = (\omega - v\Delta l)^2$. Considering small strains, $\epsilon = \Delta l / l \ll 1$, the relative variation of the other dimensions can be written as $\partial\omega/\omega = -\, v\, \partial l/l$, so the relative variation of the resistance caused by the geometrical change can be written as:

$$\frac{\partial R}{R} = \frac{1}{R}\frac{\partial R}{\partial l}\,\partial l + \frac{1}{R}\frac{\partial R}{\partial \omega}\,\partial \omega = \frac{\partial l}{l} - 2\frac{\partial \omega}{\omega} = \frac{\partial l}{l}(1 + 2v) = \epsilon(1 + 2v)$$

This yields a measure for the piezoresistance called the *Gauge factor* that can be calculated as the relative resistance change per unit strain:

$$G = \frac{\partial R}{R}\frac{1}{\epsilon}$$

Therefore, taking into account only the geometrical effect, the gauge factor is:

$$G \approx 1 + 2v$$

which, depending on the Poisson's ratio, can reach values of 1.4-2.0 [93]. At the beginning of the 20th century, the observation of an additional resistance change on top of the geometric change was difficult to explain, since ϱ was thought to be a constant, according to Drude's classical model of electron motion. Metals experience a small resistivity change with strain, while for silicon and other semiconductors the effect can be very strong.

The change in resistivity with the applied stress is based on the induced modulation of the electric field generated by the charge transport [92]. It is typical of elastic semiconductor bodies, such as silicon, germanium and gallium arsenide, and leads to substantial differences in the gauge factor, $\Delta\varrho/\varrho$ can be 50–100 times larger than the geometric term [93]. The change in resistivity can be written as a change in conductivity $\sigma = nq\mu$, where n is the number of free electrons, q is the unit electronic charge and μ is the mobility of the electrons [92]. Therefore, the variation of this parameter with stress is related to the change in the number of free electrons and the change in mobility induced by the lattice deformation, which leads to a modification of the effective mass of charge carriers [94].

2.2.2 Conversion Mechanism – nanocomposites

The tool employed for the description of electric conduction in polymer nanocomposites is called the percolation theory [95]. At low filler concentrations, metal particles are quite isolated and dispersed inside the insulating matrix resulting in a high electric resistance. By increasing the concentration of the filler, a conductive path is established and thus a drastic reduction in electric resistance comes about, defining the so–called "*percolation threshold*" [96–98].

Percolation phenomena are present in different kind of systems, such as porous media, spread of diseases and fires, gelation and glass transitions [99]. In particular the percolation formalism can be used to describe the metal/insulator transition in nanocomposites [100,101] and the thin film growth process from discontinuous to continuous states [96–98].

Percolation theory describes a system of interconnected metallic nanoparticles. The evolution of electrical conductivity of this system follows the variation of the connectivity of the particles in the insulating matrix. During the growth process

these materials undergo three electrical conduction stages (Figure 2.10). The first one is an insulating one, where electron paths are not present, and the insulating matrix dominates the electrical conduction. Below the percolation threshold φ_c the resistivity is infinite because there is no spanning cluster network of connected particles. This notion of a sharp cut-off applies well only to composites made of large conducting particles (in the micrometric scale), for which two particles can be considered electrically connected only if they essentially touch each other. However, when the nanostructured system is formed by elements and structures having sizes limited to a few nanometres, the presence of this sharp cut-off is less clear. As often it happens in such cases, even if the particles do not physically touch each other, electrons can still flow from one particle to the other if their separation is low enough that tunneling processes can occur [102,103]. In particular, below the critical transition point φ_c the tunneling process is the main mechanism that contributes to the conductivity of the system. The second is the percolation stage, where continuous electron paths or conductive networks start to form, and the conductivity of the composite jumps several orders of magnitude. In this insulator-conductor transition region, metal particles begin to touch each other, leading to the formation of conductive paths. In this regime, nanogranular systems exhibit a feature common to most random insulator-conductor mixtures, once a critical volume fraction of the conductive phase is reached, a sharp increase of the conductivity is observed (Figure 2.10).

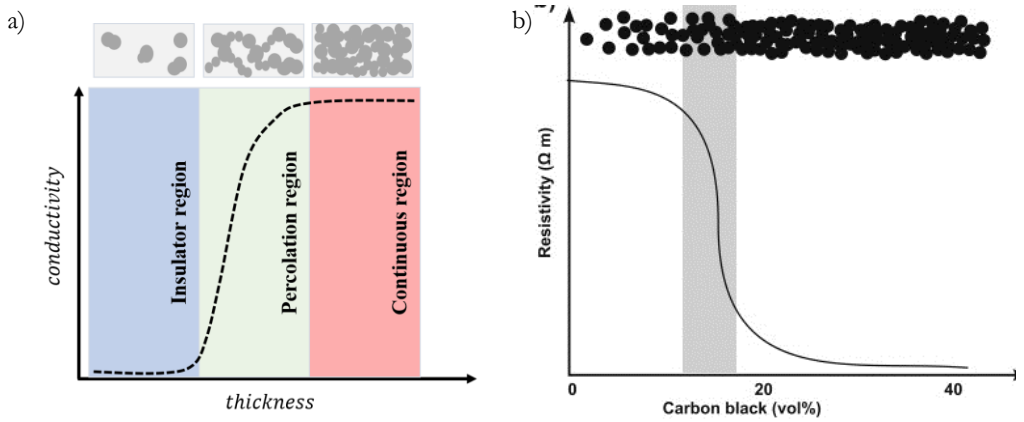

Figure 2.10: Dependence of the electrical conductivity (a) and resistivity (image from [101]) (b) of a composite with the concentration of conductive.

The electrical conduction is due to both percolation along the forming metallic network and electron tunnelling between isolated particles. By further increasing the

volume fraction of the metal fillers tunnelling effects become less and less, compared with the contribution of percolation [104,105]. The last phase is the continuous stage, where the further increase in concentration of fillers results in a small increase in conductivity approaching a maximum value. In this stage a continuous layer is formed, and an ohmic type conduction should be reached. Nevertheless, the presence of defects and grain boundaries may have a profound influence of the conduction regime. This happens with cluster assembled films (more details can be found in Section 4.2) [96–98].

The relationship between the electrical conductivity of the insulating matrix with filling conductive nanoparticles above the percolation threshold is described by an empirical power-law:

$$\sigma_{eff} = \sigma_0(\varphi_f - \varphi_c)^t$$

Where σ_{eff} is the effective nanocomposite electrical conductivity, σ_0 is the filler electrical conductivity φ_f is the fraction of conductive filler, φ_c is the fraction of fillers at percolation threshold, and t is a fitting parameter called critical exponent, it has a universal value, and it depends only form the dimensionality of the system [96,98,106,107].

The typical sensitivity obtained with the particle-based piezoresistive nanocomposites is relatively low because the 3D percolation in the particle composite compensates the geometrical change (elongation) in a strain axis by the opposite changes (shrinkage) in other axes [108]. In reality, different parameters are involved in the conduction mechanisms (e.g. geometries and properties, insulating matrix properties, and polymer–particle interaction). The percolation network can be controlled by changing the geometrical shape of the conductive fillers and their volume fraction in the elastomer composite [109]. Typical stretchable sensors monitor large deformations but cannot sense small particle strains with high precision [110].

2.3 PIEZOIONIC

Iontronic is an interdisciplinary concept that bridges electronics and electrochemistry, which devices are based on ions as signals carriers. It is found in nature, for example information transduction inside the brain is based on ion

transport across cell membranes and it is intrinsically compatible with deformable and soft applications [111].

Ionogels are a kind of hybrid materials composed of ionic liquids (ILs) and solid polymer network matrix. They have excellent mechanical properties, like high stretchability and mechanical toughness, ionic conductivity, and they can have additional properties like thermoresponsiveness, self-healing, mixed ionic/electronic properties, and photoluminescence [112], which makes them suitable for a variety of applications. They find uses as flexible supercapacitors, electrochromic devices, catalysis, and sensing devices [113].

Sensors based on ionic conductors can detect external stimuli through various types of output signals, for example resistance and capacitance reflect the changes in ion mobility and ion concentration, while in some selected frequencies the ionic conductor works as an ionovoltaic generator under mechanical stimulation [114].

2.3.1 Conversion Mechanism

Ionic gels are an emerging class of soft smart materials constituted by a polymeric backbone filled with a fluid containing mobile ions, such as room temperature ionic liquids or a solved salt in aqueous solution [115]. The piezoionic effect was recently defined as the generation of an output voltage induced by the separation of ions with different mobility, stimulated by a differential pressure applied to the material [115–118]. The redistribution of the ionic charges inside the polymer is driven by the matrix volumetric changes at the microscopic level induced by the imposed mechanical stress, which locally alter the ions concentration (Figure 2.11). The electro-mechanical response of piezoionic gels is isotropic and determined by the sign of the more mobile ions, at odd with that of piezoelectric nanocomposites, where the bias of the output voltage is determined by the polarization of the electrically poled nanofillers [61].

Simulations [119] and experiments [120] have shown that the origin of the piezoionic effect is the pressure gradient, rather than the Donnan potential [121] at the interface between the conductive polymer and the electrolyte. The key difference with piezoelectrics is that ions (free charges) are mobile, unlike the dielectric charges in piezoelectrics, and therefore the sign of the generated voltage is determined by the transport of the faster ions [120]. The piezoionic effect depends on the ions type, size and mobility, as well as on the mechanical properties of the polymeric network.

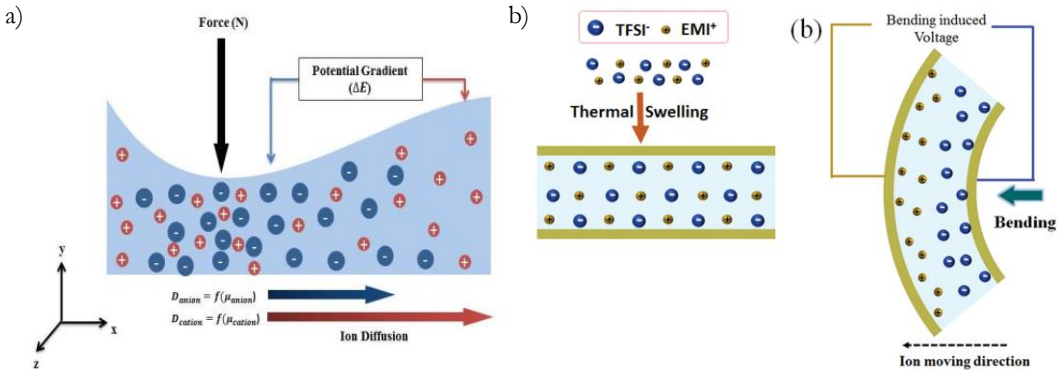

Figure 2.11: Schematic diagram for the mechanism of the self-powered sensing in piezoionic strain sensor due to redistribution of the ions under local pressure (a) [116] and bending (b) [122].

2.3.2 State of the art

The research on this kind of composites is rather new, and only few articles are present in literature. In general, these gels have low output voltages (1-10mV) and respond well to low frequencies (<1Hz). In the following paragraphs are presented the piezoionic materials reported in literature.

Dobashi et al. [115,116] (2015-2016) fabricated a polyurethane hydrogel-based touch sensor swollen with electrolytes that responded to a finger-tapping pressure (30kPa) with a voltage of 10mV and a current of 100nA and a PVDF-HFP based ionic polymer with a maximum sensitivity of 25 μV/Pa at 10 mHz.

Liu et al. [122] (2016) engineered a wearable piezoionic strain sensor that generates an output of 1.3mV under a bending-induced strain of 1.8% in 50ms, and was used to monitor human activities, as wrist bending and heart rate.

Adjaoud at al. [123] (2021) formulated a sensor based on Aquivion® conductive membranes and PEDOT-PSS flexible electrodes that provide an electrical output signal of 2.9mV.

Li et al. [124] (2021) manufactured a knittable electrolyte-coated high-surface-area carbon nanotube yarn. The yarn can generate voltage signals of 4−15 mV with low noise (0.024 mV) between its two ends when stretched asymmetrically. The voltage amplitude is very sensitive to tensile stretches at frequencies of 0.1−10 Hz and strains of 1-80%.

3. PIEZOMETER

If you cannot measure it,
you cannot improve it.
-Lord Kelvin

Despite the numerous studies on piezoelectric composites reported in literature, nowadays the main focus remains on the maximization of the piezoelectric output by varying the different ingredients (polymeric matrix, nanofiller, electrode types and other additives), while characterization techniques suitable for the quantitative measure of the piezoelectric performance of nanocomposites are not consistently applied in this research topic. The measure of piezoelectricity presents many challenges and technical issues, caused mainly by the lack of a standard and universally recognized method (see references [61,125–136] and Appendix A). This topic has been explored extensively also by Šutka et al. in [137].

In the following chapters is presented the characterization approach developed during the PhD. This method allows to perform a thorough electro-mechanical characterization of soft piezoelectric nanocomposites in the compression mode, enabling quantitative and reproducible measurements of the piezoelectric charge constant d_{33} and providing high sensitivity and the spectral distribution of the electro-mechanical conversion capabilities. In particular, the presented experimental set-up allows to perform reliable measurements of the piezoelectric coefficient spectrum over a selected frequency range for piezoelectric polymeric nanocomposites with a piezoelectric coefficient d_{33} down to 0.5pC/N. The technique was validated on a commercial sample of PVDF, and then used to characterize the piezoelectric performance of some novel piezoelectric polymeric nanocomposites, as reported in Chapter 5.

3.1 PIEZOELECTRIC CHARACTERIZATION

3.1.1 Piezoelectric coefficients

In Section 2.1.1 the piezoelectric coefficients were introduced as:

	Direct effect	Converse effect
Piezoelectric charge coefficient	$d_{ij} = \left(\frac{\partial D_i}{\partial \sigma_j}\right)_E$	$d_{ij} = \left(\frac{\partial S_j}{\partial E_i}\right)_\sigma$
Piezoelectric voltage coefficient	$g_{ij} = \left(\frac{\partial E_i}{\partial \sigma_j}\right)_D$	$g_{ij} = \left(\frac{\partial S_j}{\partial D_i}\right)_\sigma$

The piezoelectric charge coefficient relates to the electric charge generated by unit area for applied stress, and therefore the generated charge for applied force (C/N). It is the most crucial figure of merit that characterize the performance of a piezoelectric material.

$$d_{ij} = \frac{q_i/A_i}{\sigma_j}$$

The two constants d_{33} and d_{31} are of particular importance. The transverse piezoelectric coefficient, d_{33}, is employed when the force is applied along the polarization axis, and the charge is collected from the same surface the force is applied to. The longitudinal piezoelectric coefficient, d_{31}, is employed when the force is applied perpendicularly to the polarization axis, and the charge is collected from the same surfaces as in d_{33}. The piezoelectric charge constant is one of the most crucial characteristics to evaluate for a piezoelectric material.

The piezoelectric voltage coefficient, also called voltage output constant, is related to the electric field generated by a unit mechanical stress (Vm/N).

$$g_{ij} = \frac{E_j}{F_i}$$

These constants can be related to the piezoelectric charge coefficients by the simple relation:

$$g = \frac{d}{\varepsilon}$$

where ε is the relative permittivity.

3.1.2 Standard Characterization Methods

The most reliable method to measure the piezoelectric coefficient of piezoelectric materials is the dynamic method, or piezoelectric resonance method, which exploits the inverse piezoelectric effect. This method is the most accurate, since it is relatively easy to apply a uniform electric field, and the strain can be measured with reasonable accuracy (around 1%) by strain gauges or interferometric techniques. Furthermore, a dynamic excitation prevents the drift due to pyroelectric charges, and it is therefore more precise. The problem, for this kind of characterization, is to excite the samples and measure their response in different directions, or to excite and measure peculiar geometries or materials that does not present an elastic behaviour.

In order to obtain a simple direct measurement of the piezoelectric charge coefficient the most widely used method is a quasi-static d_{33} piezometer [138,139]. For the practical measurement of d_{33}, the equation can be altered as:

$$d_{33} = \frac{Q_3}{A_3} * \frac{A_3}{F_3} = \frac{Q}{F}$$

Since the measurements of the areas cancel out, it is evident that d_{33} can be simply determined by measuring the applied force on a sample surface and the generated charge on the same surface. The constant electric field condition is fulfilled in the short-circuit configuration. To achieve this condition a large capacitor should be placed in parallel to the piezoelectric sample. Applying a mechanical stress to the piezoelectric, the charge generated across the electrodes is transferred to the capacitor plates, and it is therefore possible to determine its value by a voltage measure across the capacitor (Figure 3.1). This method, which is very simple, is subjected to many errors and imprecisions mainly due to a pyroelectric thermal drift and charge loss due to internal conduction, and it is not used anymore for characterization, since it is difficult to control the electric boundary conditions.

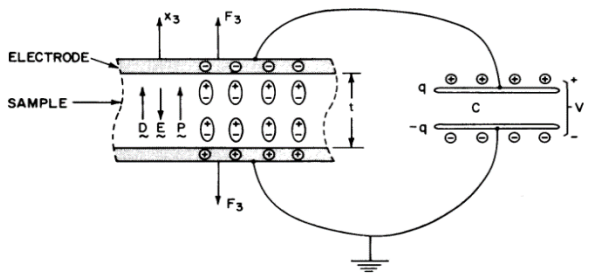

Figure 3.1: Static method for piezoelectric coefficient measurement. Image from [140].

The most widely used characterization method is the quasi-static method, or Berlincourt method. This method exploits the direct piezoelectric effect using a small oscillating force, with a frequency range around a few hundred hertz, to excite the sample. The output charge is measured with an electrometer or an appropriate electronic circuit. There are currently no standards for this measurement method, and consequently each system performs the measurement slightly differently. Since there are a large number of variables involved for the determination of the piezoelectric coefficient, the measured piezoelectric coefficients are unreliable, especially for relative comparison. Interlaboratory tests have shown systematic differences between results on the same samples, those differences are reduced under the same measurement conditions [139].

A Berlincourt d_{33}-meter comprises two parts. The first (Figure 3.2a) is composed of a force head able to clamp the sample with a controlled static preload force, an AC force load system to excite the sample with controlled frequency and amplitude, and a load cell, i.e. a piezoelectric sensor or a strain gauge, to measure the force applied to the sample The second is the charge measurement electronics, that comprises the contact electrodes to extract the charge and the signal conditioning electronics, that must operate under constant field conditions (for example exploiting a virtual mass amplifier or a large capacitor). The piezoelectric coefficient d_{33} is simply obtained dividing the charge measurement by the force measurement, either in amplitude or in RMS. This ratio might be done both with digital signals, or electronically using a differential amplifier. There are some commercial d_{33}-meters based on this technique and are the most widely used for what concerns the measurement of hard piezoelectric materials, like crystals or ferroelectric ceramics [141,142].

Figure 3.2: a) Schematic of the force-head component of a Berlincourt measurement set-up. b) A commercial d_{33}-meter (©PiezoTest)

3.1.3 Soft piezoelectric materials measurements

Despite the fact that piezoelectric polymeric nanocomposites are a widely researched topic, there is no common recognized method for the characterization techniques used to evaluate their performance, differently from when piezoelectric bulk materials are concerned, where the material Figure of Merit is determined based on their piezoelectric charge coefficient.

The three most common reported tests carried out in piezoelectric literature are piezo-force microscopy (PFM), unimorph cantilever beam testing, and tapping with a human finger. These techniques each have limitations, PFM measures only nanoscale response, unimorph cantilever beam testing only considers one mode of motion, and human finger tapping results in an undefined force, additionally it can introduce static charges (see Triboelectric effect in Section 2) [137].

The absence of a standard set of measures that describe the performance of this type of materials, coupled with the absence of reliable methodologies to assess the classic piezoelectric constants for soft nanocomposites, results in sets of non-comparable qualitative measurements of different quantities under often unreproducible mechanical stimuli. In fact, most of the work presented in literature report operative values of voltage and current as a performance assessment, usually without a detailed description of the experimental method used to obtain them.

Many researchers report "finger tapping" measurements, some other report voltage or current measurements made with a single force and a single stimulation frequency (see references from [58,103–114] and Appendix A for examples of such broad scattering of different characterization techniques). These characterization techniques are not suitable for many reasons: on one hand they could be affected by many artifacts (for example mechanical system resonant frequencies that would invalidate the whole measurement, or signal conditioning circuits used outside their range, as in ref. [134]), on the other hand the quantities that are usually characterized are operating voltages and currents, sometimes not even put in relation with the applied force. Moreover, as also reported by Šutka et al. [137], piezoelectric measurements done under uncontrolled conditions may be affected by other effects, such as contact electrification, triboelectricity, electrostriction or dielectric charging.

Only for few piezocomposites the value of the piezoelectric coefficient d_{33} is presented, usually measured with a commercial system operating at a single frequency and with a single pre-load force, while this class of materials has usually lower d_{33} than that of PVDF [83] and present a non-trivial dependency to the

stimuli frequency, due to the complex electro-mechanical coupling mechanism [143][144]. Due to these sensitivity issues these systems are usually employed to measure the piezoelectric coefficients of PVDF-based nanocomposites [145] or piezoelectrects, namely voided charged polymers [61], which have a high piezoelectric constant, even though they lack in thermal stability, they age at high deformations, and they do not show any longitudinal piezoelectric effect [79–82]. There is only one case of a measure of d_{33} concerning a piezoelectric nanocomposite with a polymeric base different than PVDF [134]. The measure was performed applying specific loads orthogonal to the substrate, and the charge was measured using an in-house built electrical conditioning circuit; the obtained piezoelectric coefficient for the nanocomposite was 40pC/N. However, the measure was performed using static loads and using an electronic circuit for signal processing that could not provide reliable information on the effective electrical charge generated by the nanocomposite, due to the specific configuration of the circuit and components employed (see for example [146] for technical details).

This lack of reproducibility in characterization techniques suggests that would be useful to develop and describe such an instrument, and to share the knowledge necessary to build it.

3.2 DESIGN AND DEVELOPMENT

During the course of this PhD project a suitable system for the measurement of soft polymeric nanocomposites was designed and developed. The approach was based on a Berlincourt-type apparatus, providing spectral information on the electro-mechanical response in a wide range of frequencies of compressive loads, with high sensitivity and automated data acquisition modalities, enabling repeatability and reproducibility of the electro-mechanical characterization in the low-force regime.

The system was designed to be modular and can be developed to cover different measurement ranges. A schematic of this measurement system is reported in Figure 3.3a, while some pictures of the development steps (first prototype, project, realization of the final system) are reported in Figure 3.3b, c and d.

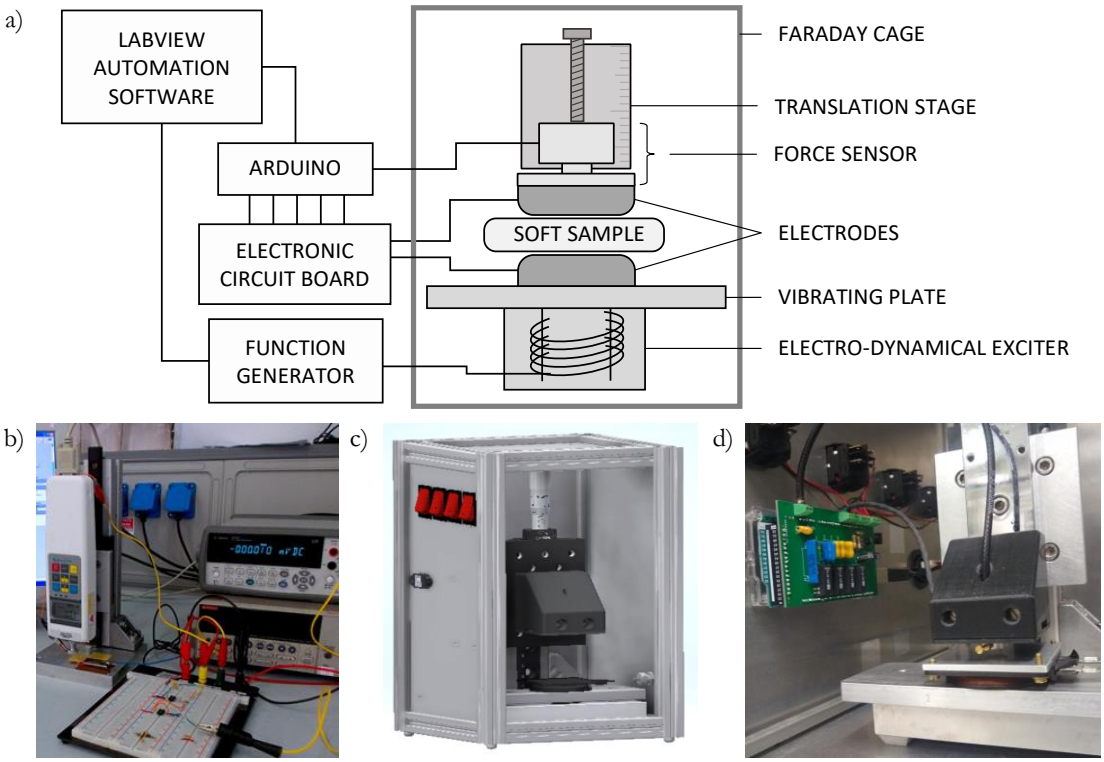

Figure 3.3: a) Experimental set-up used to measure the piezoelectric coefficient spectra of the piezoelectric polymer nanocomposite. b),c),d) Progressive development of the electro-mechanical characterization system. First prototype (a), CAD project of the system (b) and final realization (c).

3.2.1 Hardware

The system is designed to operate in a quasi-static or dynamic regime, in line with the Berlincourt technique [134. A vertical oscillating force is applied perpendicularly to the sample by means of an electromechanical exciter, while the force is measured by a force sensor and the output charge is collected by a dedicated electronic circuit. The system is modular, and its components can be interchanged to select different measurement ranges.

The selection of an appropriate exciter and a matching force sensor allows to explore different frequency and force ranges. In this work, a Visaton EX 60S loudspeaker and a TE Connectivity FS2050-000X-1500-G force sensor (range of 14.7N,an accuracy of $\pm 1\%$) were used. These two components allow to explore the range 0.1N-3N for the force signal amplitude and from below 1μHz up to over 1200Hz for the signal frequency. Both components are mounted on a structure (Figure 3.4) appropriately designed to maintain the various elements aligned and positioned

inside a Faraday cage to avoid cross-talking with electromechanical noise from the environment.

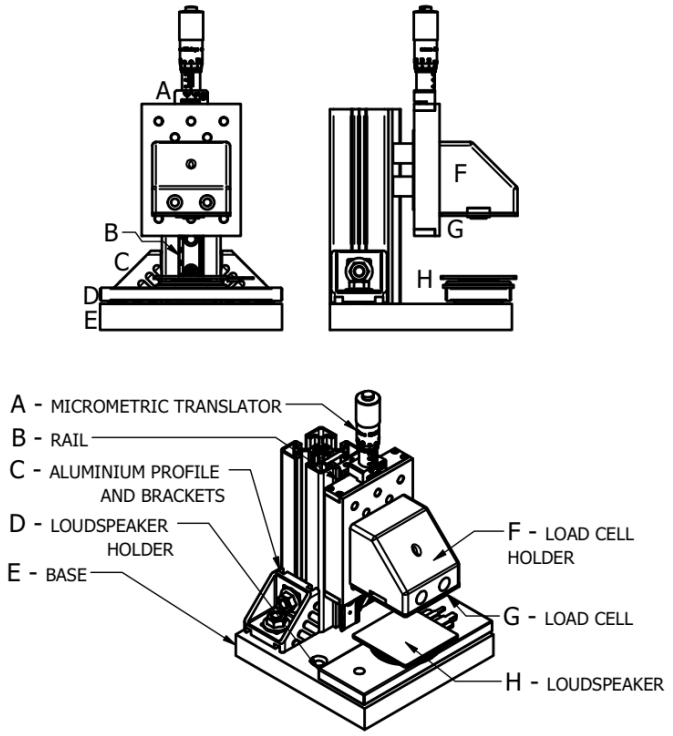

Figure 3.4: Mechanical CAD design of the assembly of the measuring instrument.

The main structure is composed of a solid base, vibrationally insulated from the ground, and a vertical column, stable enough to avoid bending when the exciter is in function. This structure (labelled as C in the CAD design) was built using ®Bosch Rexroth aluminium profiles and angle brackets, to ensure rapid and precise assembling with a solid fastening. The vertical profile is equipped with a dovetail optical rail and two dovetail rail carriers (®Thorlabs) for vertical gross positioning of the measuring head. A single-axis translation stage with standard micrometer (®Thorlabs) is connected to the rail carriers to regulate the fine positioning of the measuring head.

In order to optimize the system design, to reduce the final dimensions and connection cables' length, and to assure the vertical alignment of the elements, a custom element was designed and 3D printed. This element (Figure 3.5a) serves to hold the load cell and to house the electrical contacts necessary for the measurement.

As can be observed in Figure 3.5c, this element is grooved in order to fit the load cell sensor (Figure 3.5b), which is kept in place by a frame. The load cell holder shape was studied to resist the mechanical strains imposed by the electro-mechanical exciter and to stop against the translation stage.

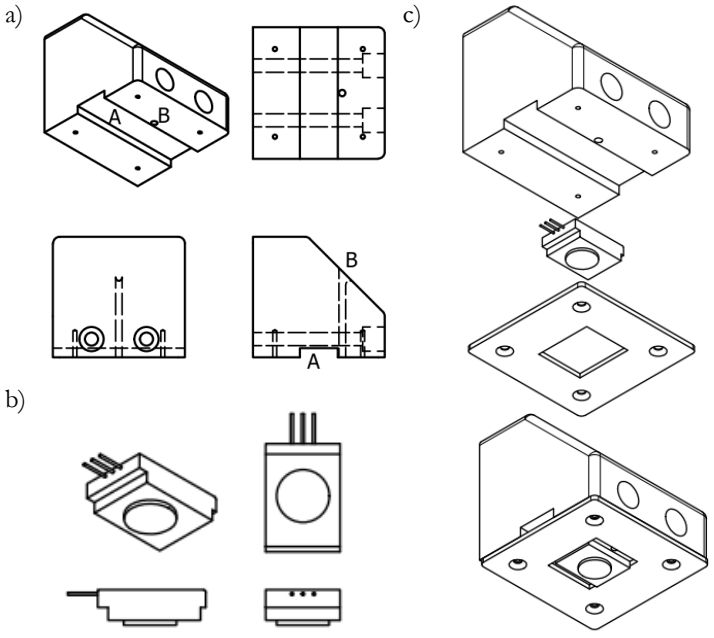

Figure 3.5: a) Load cell holder design. The groove (A) is designed to house the load cell, while the hole is designed to house the electrical connection for the charge signal. b) Load cell shape (®TE Connectivity). c) Load cell holder mounting.

The electrical connectors of the load cell can be connected through the hole created by the groove, while the electrical connection for the charge measurement is connected to the measuring circuit through the vertical hole (labelled as B in the schematic in Figure 3.5). The cable housing is critical in order to reduce the electrical noise coming from cable vibrations in the electro-magnetic field generated by the electro-mechanical exciter. Moreover, all the cables used inside the Faraday cage were shielded with braided sleeves connected to ground.

The force sensor and the electro-dynamic exciter are equipped with suitable lightweight electrodes fabricated with Aluminium (Figure 3.6) and electroplated with gold in order to avoid dielectric layers that would introduce spurious double-layer capacitances that interfere with the charge measurement. The top electrode is fastened to the force sensor head through a cyanoacrylate glue, that guarantees a

rigid constraint and the electrical insulation from the sensor. The bottom electrode is secured to the vibrating surface using four screws. The electrical cables between the electrodes and the measuring circuit are connected using screws, bolts and cable lugs. The bottom electrodes, connected to the vibrating surface, is grounded, while the top electrode is connected to the measuring circuit (which will be described in detail in Section 3.2.2).

a) b)

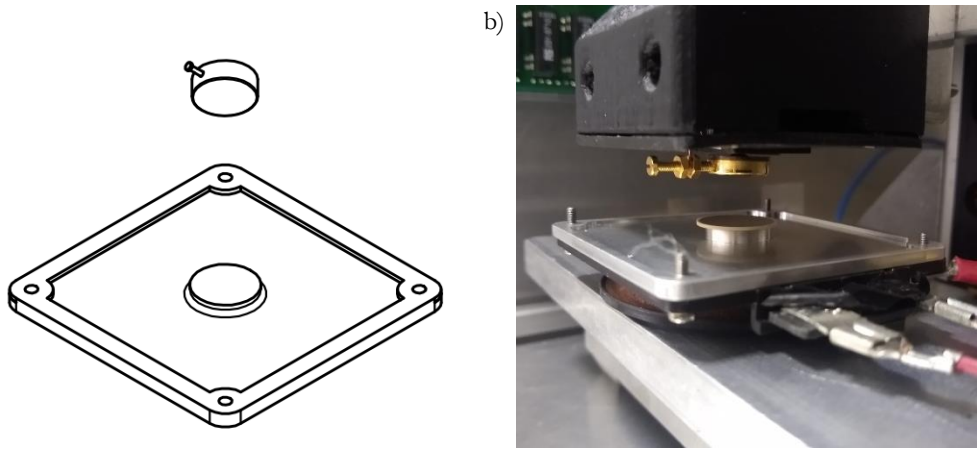

Figure 3.6: a) Top and bottom electrodes CAD design. b) Top and bottom electrodes before a measurement. As can be observed in the picture the system ensures the alignment of the two electrodes, sandwiching the sample.

The conditioning circuits converts the electrical charge into a voltage analog signal, and it is designed in an Arduino shield configuration (i.e. to be mounted directly on top of the Arduino board), in order to minimize the distances between the two components and therefore reduce the noise picked up by the connection. Arduino and the circuit are fastened to the Faraday cage next to the measuring head (Figure 3.7). The force and charge electronic signals are collected and converted by an Arduino Mega ADC, and then analysed by a dedicated LabVIEW program. The pre-load force can be selected manually by regulating a micrometric screw gauge, and the system allows to select the stimuli frequency and the dynamic force programmatically through the LabVIEW software, allowing to perform multiple measurements. This allows to reproduce the measurement procedure in a very simple way by defining a measurement protocol.

a) b)

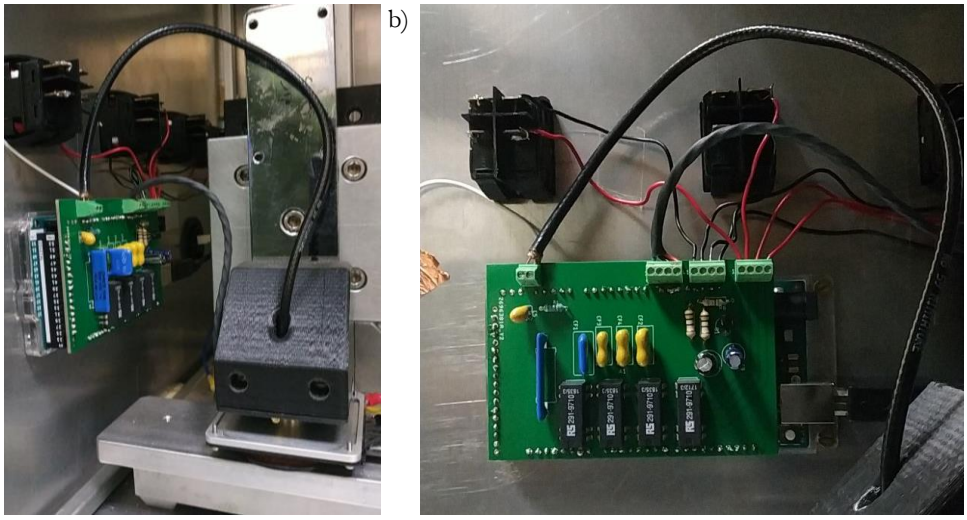

Figure 3.7: The electrical circuit on top of the Arduino MEGA. The electrical conditioning component is fastened to the Faraday cage wall next to the measuring head.

3.2.2 Electronics

The core of the instrument is the dedicated electronic circuit that allows to perform the measure of the output charge from the piezoelectric element. The signal conditioning, schematized in Figure 3.8 , is a charge amplifier circuit [147][148] with some alterations to the classic layout, introduced in order to filter out the DC signal coming from the natural polarization of the samples and avoid spurious charges' integration. A typical charge amplifier circuit is an operational amplifier with a feedback loop composed of a capacitor and a resistor in parallel. The high input impedance of the operational amplifier forces the charge to accumulate over the feedback capacitor. The output voltage is therefore equal to the voltage across this capacitor, which means that the input charge can be obtained as:

$$Q_{input} = V_{output} \cdot C_F$$

This implies that the feedback capacity and the ADC set both the instrument sensitivity and range. In order to be able to read charges as small as fractions of picocoulombs, feedback capacitors as small as 1pC are needed, which is also the magnitude of the stray capacities for a printed circuit board. These stray capacities not only enhance the noise, but, since they are parallel to all the elements (Figure 3.8), they also affect the gain by a factor $1 + \frac{C_{stray}}{C_f}$, which is not negligible since C_{stray} and C_f are comparable quantities. In order to diminish the electromagnetic noises picked up by the loops and to reduce as much as possible the stray

capacitances, the circuit board was equipped with a ground plane, and the layout was designed in order to minimize the distances between the components.

In this configuration the circuit behaves as a current integrator. For real amplifiers, any input bias current causes a saturation of the signal in a very short time. To avoid this, a feedback resistor is added in parallel with the capacitor, in order to discharge the capacitor periodically. Due to this addition the whole circuit has a lower cut-off frequency at:

$$f_{low} = \frac{1}{2\pi R_F C_F^*}$$

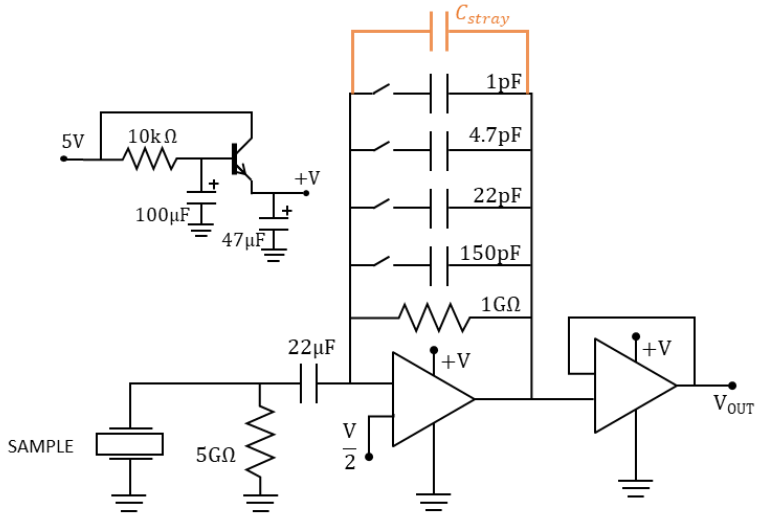

Figure 3.8: Charge amplifier circuit schematic with the stray capacitance that affects the gain. The inset shows the DC voltage stabilizer integrated on the board for a stable power supply.

The choice of the operational amplifier is crucial, as its input bias current might be amplified by the feedback. The operational amplifiers used were a LMC6062 on the prototype version, a precision dual amplifier with an extremely low input bias current (10fA) and offset voltage (100µV), and a LMP7721 on the PCB version, a surface mount precision dual operational amplifier with an input bias current of 3fA and an offset voltage of 26 µV. In order to incorporate different measurement ranges four feedback capacitors were used: 1pF (0.1÷2 pC/N), 4.7pF (1÷10 pC/N), 4.7pF (5÷50 pC/N) and 150pF (30÷750 pC/N).

The circuit was prototyped with through hole components on a double sided perfboard with a ground plane on the top side. The ground plane served to reduce the ground loops and avoid noises that would hide the signal. In this configuration the multi-range capability was achieved through female-male pin connectors soldered on the board. The circuit served as a proof-of-concept, but its behaviour was not stable in time, so a stabler prototype version was implemented.

a) b)

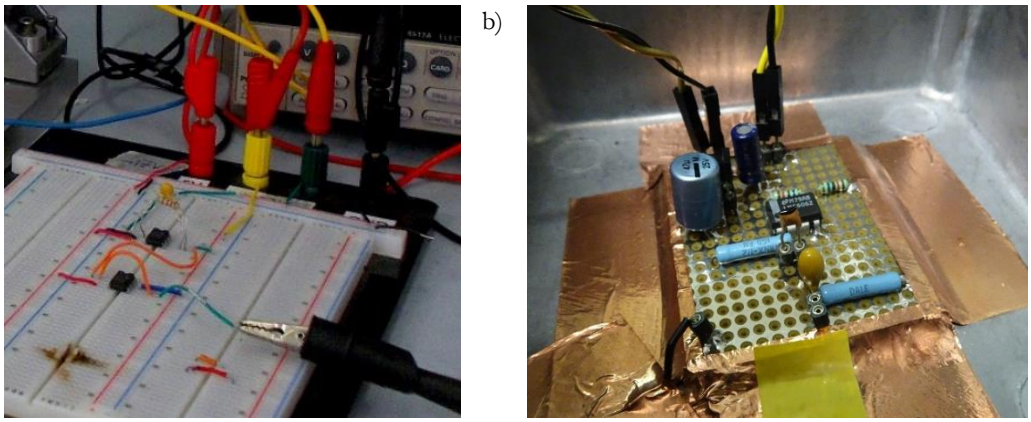

Figure 3.9: Circuit prototype on a breadboard (a) and a perfboard (b).

In Figure 3.10 and Figure 3.11 are reported the CAD designs of the board, implementing four switch-activated relays for gain selection. The circuit was realized in two different versions with improved precision and reduced noise. The first version of the circuit was first etched from a copper board by means of photolithographic process. The board (Figure 3.10a) was designed with a suitable software (Autodesk Eagle) and the negative of the board (Figure 3.10b) was printed on a transparent sheet and then impressed on the positive photoresist of a copper photoresist board via UV-light. The cured resist and the copper were etched with chemical acids, then the non-cured photoresist was cleaned and the holes for the electrical components were manually drilled, and the components were soldered on the two sides (Figure 3.10c). Once the functioning of the complete design was assessed, the circuit design was modified from 1-layer to 2-layer (Figure 3.11a) and the final PCB was fabricated on a standard FR4 support with a LeadFree HASL-RoHS compliant surface finish by a PCB manufacturer website. The different versions of the circuit board were calibrated in order to assess their performance and stability.

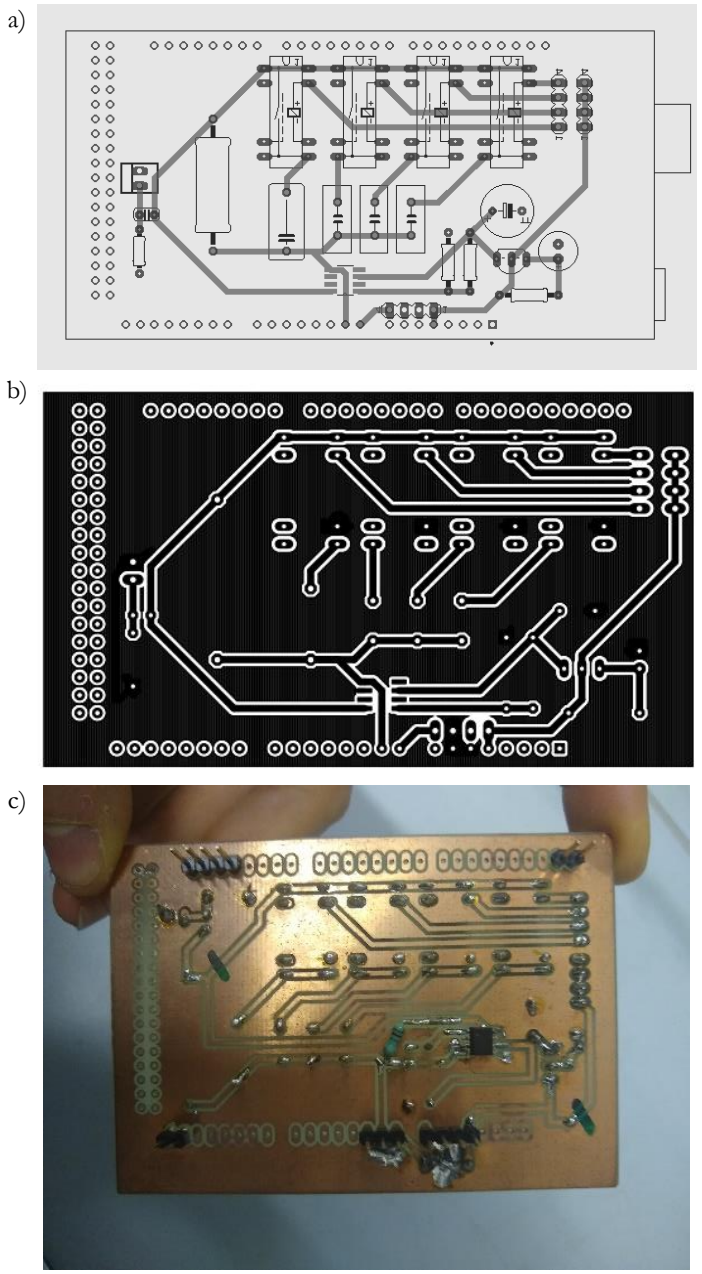

Figure 3.10: a) CAD design of the PCB, b) Photolitography mask, c) Final realization of the board photoengraved on a copper board.

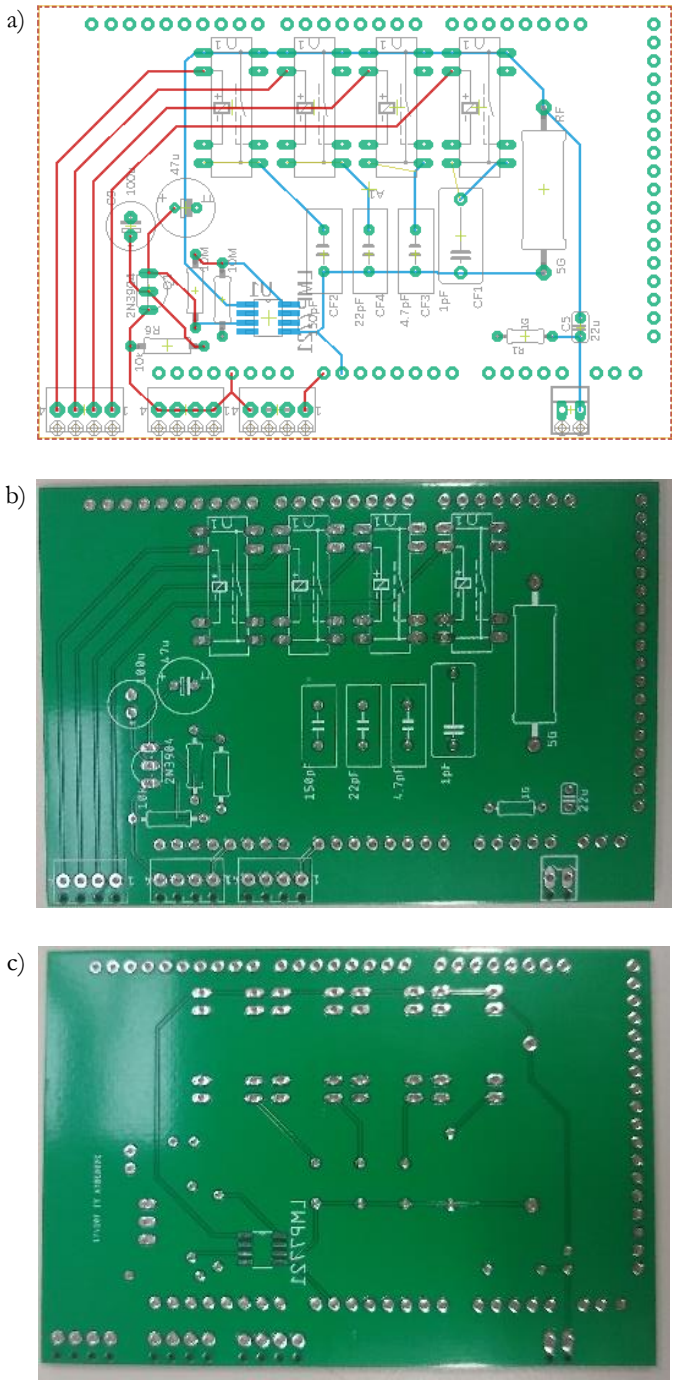

Figure 3.11: a) CAD design of the PCB and both sides of its realization printed by ®JLCPCB.

3.3 CALIBRATION

In order to obtain quantitative results, the electronic circuit was calibrated using a charge input signal obtained through an AC current, controlled in amplitude I_0 and frequency f, generated with waveform generator (Agilent 32210A) coupled in series with a bias capacitor, so that the input AC signal was integrated on the capacitor becoming an oscillating charge ($Q_{in} = I_0/2\pi f$), which served as an input for the electronic signal conditioning circuit, which read it as $Q_{in} = \Delta V C_F$ (Figure 3.12).

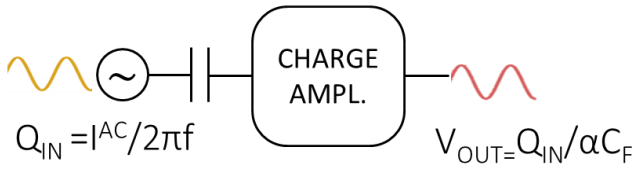

Figure 3.12: Experimental set-up for circuit calibration.

The calibration procedure was necessary to assess the effect of both the percentage charge loss due to contact resistance at interconnections between components and to evaluate the stray capacitance responsible for the error on the circuit gain. These contributions result in a linear loss factor, which is represented with a parameter α.

The prototype circuit in Figure 3.9b was calibrated at five different frequencies and the parameter α was evaluated. The first measure showed a good linearity between input charge and output voltage, with linear loss factors between 3 and 7, depending on the feedback capacity and the AC frequency. The repetition of the measurement after several months showed a considerable instability of the circuit (Figure 3.13b).

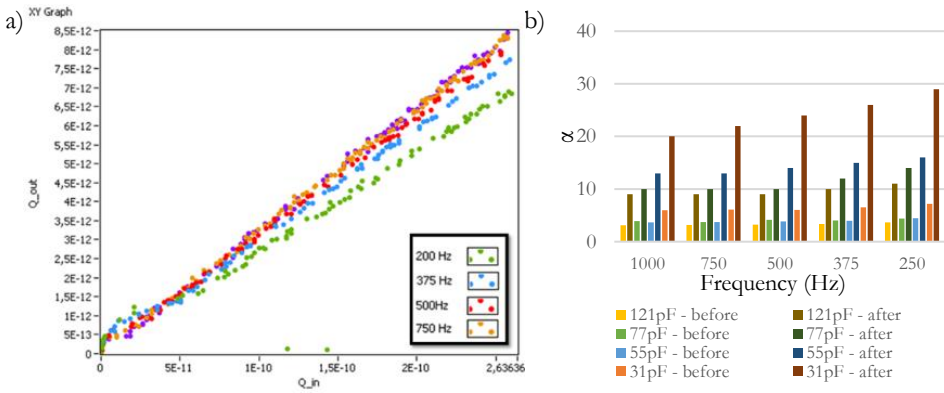

Figure 3.13: The calibration measurement the prototype circuit (a) repeated after seven months on highlighted a circuit instability (b).

The circuit fabricated through photolithography was calibrated with the same procedure, the result of one of these measurements can be observed in Figure 3.14a. Its better performance allowed to observe better the low-charge regime of the curves, where the function generator used to produce the input signal does not have a linear behaviour with the applied voltage due to a current limitation at 100nA. This was confirmed with a voltage-current measure on a10MΩ load (Figure 3.14b). The input charge could be therefore calculated from the 100nA current, and therefore it was possible to measure α for lower charges and, therefore, lower ranges.

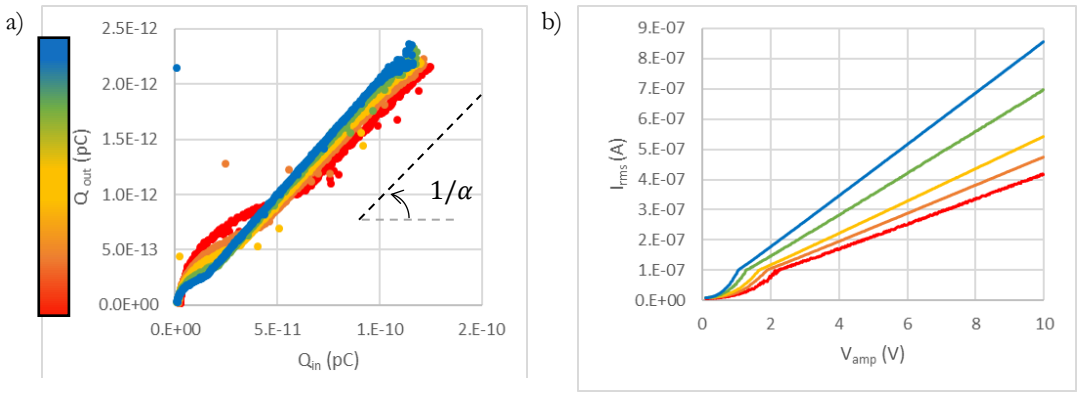

Figure 3.14: Calibration measurement of the etched PCB (a) and non-linear function generator

These measurements allowed to perform an evaluation of the stray capacitance in the feedback loop (Figure 3.15). It was possible to evaluate C_F^{stray} from measurements of the loss parameter using different feedback capacities, in fact:

$$V_{OUT} = \frac{Q_{IN}}{\alpha C_F} = \frac{Q_{IN}}{\alpha^*(C_F + C_F^{stray})}$$

$$\alpha = \alpha^* \frac{C_F + C_F^{stray}}{C_F} = \alpha^* + \alpha^* \frac{C_F^{stray}}{C_F}$$

By analyzing the curve α versus C_F^{-1} it was possible to obtain an approximate value for the stray capacitance and an absolute value for the loss parameter, not dependent from the feedback capacity. For the etched circuit the result were:

$$C_F^{stray} = 1{,}83pF$$

$$\alpha_{real} = 18$$

The value of stray capacitance was comparable with the value of the lower feedback capacity; hence its contribution was still considerably high.

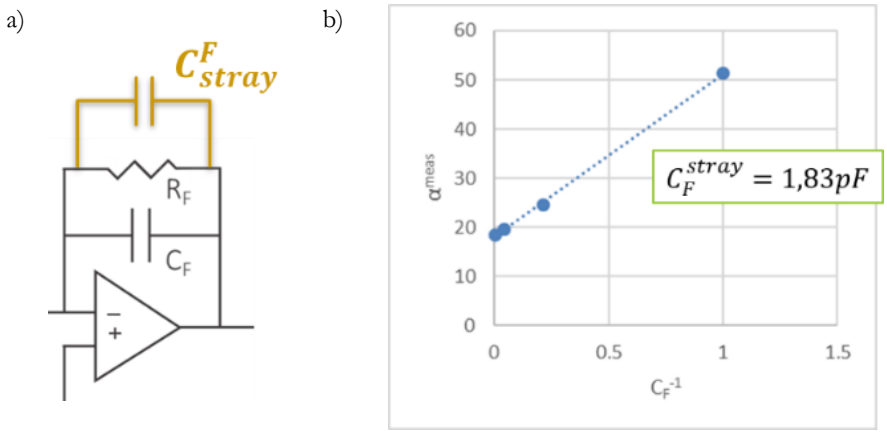

Figure 3.15: a) Circuit schematic with stray feedback capacitance, b) By fitting the α versus C_F^{-1} plot it is possible to obtain a value for stray capacitance.

The final circuit on the printed circuit board was calibrated for different frequencies, using four different feedback capacities, and the results are summarized in Figure 3.16. As can be observed the loss parameter α decreased with increasing frequency and for higher feedback capacities: this behaviour reflected the stray capacitance in parallel with the feedback capacitor and the gain behaviour near the low cut-off frequency f_{low} of the charge amplifier circuit.

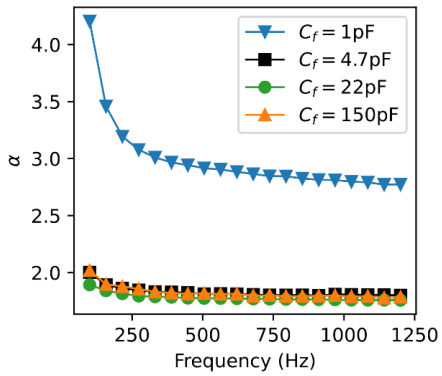

Figure 3.16: Through the calibration procedure the loss parameter caused by the stray capacitances and the linear resistances is measured. As expected, this parameter decreases with increasing frequency and is significantly higher for the lower feedback capacity, since it has the same magnitude of the stray capacitance.

3.4 VALIDATION

The measuring system was validated measuring the piezoelectric coefficient spectrum of a known sample, i.e. a commercial PVDF membrane (© Precision Acoustics, thickness $110\mu m$). The results are reported in Figure 3.17 and Figure 3.18.

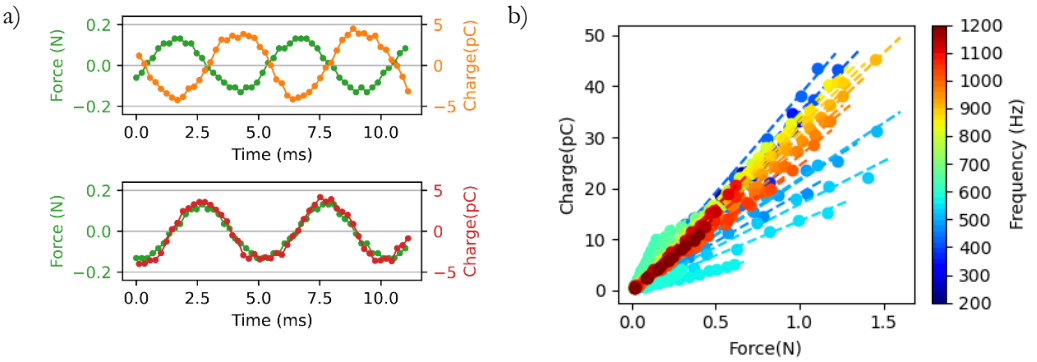

Figure 3.17: a) Phase inversion under sample switching for PVDF, b) Linearity of charge-force response at different frequencies for a PVDF sample.

These measures allowed to define the measurement protocol and to identify the resonant frequencies of the instrument, at which the measures are affected by a systematic error.

The first indicator of a piezoelectric reading is the phase inversion under sample switching. The presence of this switching can only be ascribed to the anisotropic behaviour of the sample, therefore it allows to exclude any other source, as, for example, the current induced on the electrode from the electromagnetic signal powering the exciter. The phase inversion for PVDF can be observed Figure 3.17a, while in Figure 3.18a the phase difference between the force and charge signal for the different frequencies is plotted. As it can be observed, except for some outliers and a small region around the frequency of 600Hz, the signals were definitely in phase or in counterphase, with a slight drift with increasing frequency. This drift, of roughly $7 \cdot 10^{-4} {rad}/{Hz}$ excluding the outliers, can be ascribed to the delay between the two signals readings. Since the two signals were sampled using the ADC of a single Arduino, the shift between the two readings is equal to the sampling rate of such ADC. In fact, the time delay measured from the phase drift is $\Delta t =$

$\frac{1}{2\pi}\frac{1}{f}\frac{\partial\theta}{\partial f} = 0{,}1ms$, and the ADC of the Arduino Mega has a 9600Hz sample rate, that is converted in a 0,1ms time difference between the two measurements.

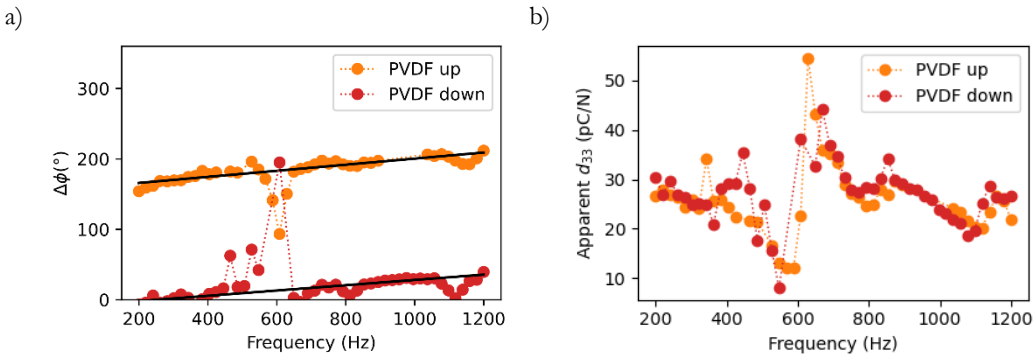

Figure 3.18: a) Phase difference between the force and charge signals for the measure in Figure 3.17a. The drift with increasing frequency can be ascribed to the delay between the two readings caused by the ADC clock. b) Piezoelectric coefficient spectra for PVDF in both the phase configurations. The difference between the two spectra can be ascribed to a sample anisotropy.

The second parameter investigated was the effect of the preload force imposed across the sample. In Figure 3.19 some PVDF d_{33} spectra with preload forces ranging from 1N to 10N are presented. As can be observed in the graph the spectrum was shifted down with increasing preload force, and this shifting was particularly evident for preload forces from 1 to 5N, while in the range 5-10N the signal was more stable. To analyze more accurately this behavior, the average piezoelectric coefficient versus the preload force were plotted (Figure 3.19b).

Another observation that can be made looking at the spectra plotted in in Figure 3.19a is that a sharp peak of the piezoelectric coefficient around the frequency of 600Hz is present in all the measures. The peak is slightly shifted towards higher frequencies with increasing preload force and in correspondence of the peak there is a particularly high deviation from the phase difference trend discussed previously. Since all the measured samples presented this sharp peak around 600Hz, and the phase difference between the two signals was significantly far from the phase/counterphase behavior discussed before, it was inferred that this peak was an instrumental resonance and does not reflect the real electro-mechanical response of the sample. Since the d_{33} values for the frequencies around 600Hz are not relevant to our analysis the stability evaluation done in Figure 3.19c was repeated excluding the frequencies around 600Hz. In order to find the conditions for a stable and

reproducible behavior, the average d_{33} coefficient was plotted with different cut-off widths (Figure 3.19d), and measurements were subsequently performed with a minimum preload of 5N and the frequencies between 550Hz and 650Hz were ignored.

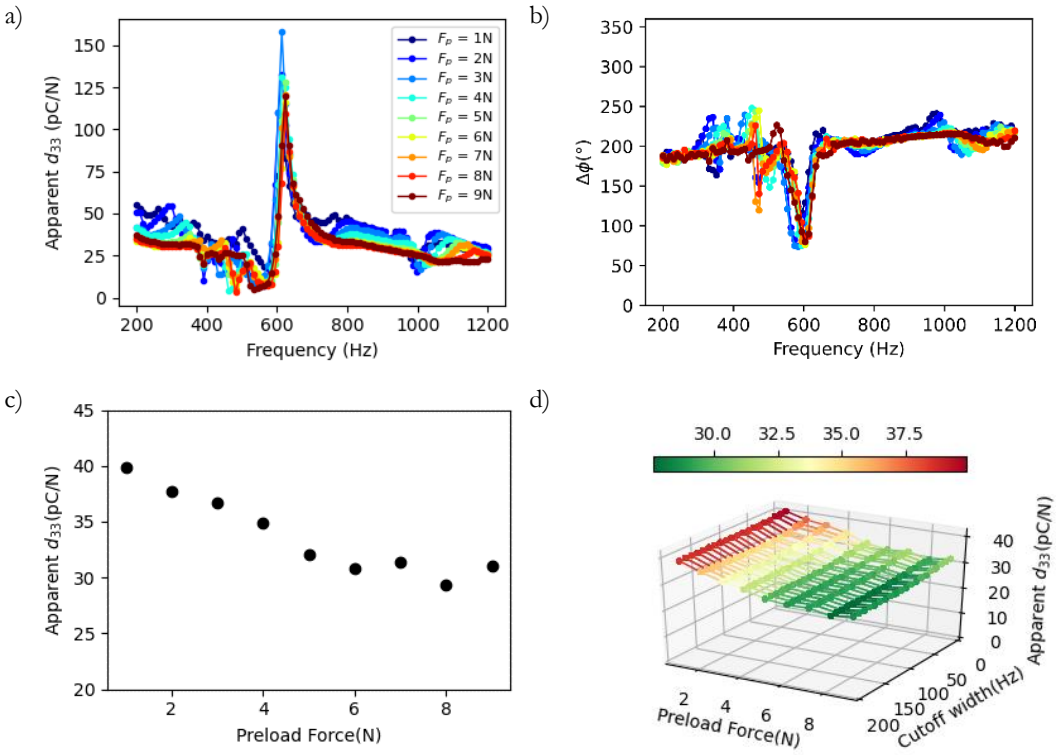

Figure 3.19: a) Piezoelectric coefficient spectra of PVDF with different preload forces. b) Phase difference between the force and charge signals for the measure in a. c) Average d_{33} of PVDF for different preload forces. In d) is represented the same as in c, but the average is computed excluding the spike around 600Hz which is an artifact caused by a mechanical resonance of the measuring instrument.

The averaged d_{33} coefficient obtained over the considered spectrum for commercial PVDF is (28,3 ± 0,3) pC/N on one side and (31,6 ± 1) pC/N on the other, which is compatible with the PVDF technical sheet (28-32pC/N). This measurement system allows to test the performance of a single side of the sample, allowing to distinguish possible anisotropies in the thickness direction of the material.

Averaging over 40 different measures made with different parameters (low forces, high forces, different feedback capacities) (Figure 3.20) a mean value of (30 ± 1) pC/N was obtained.

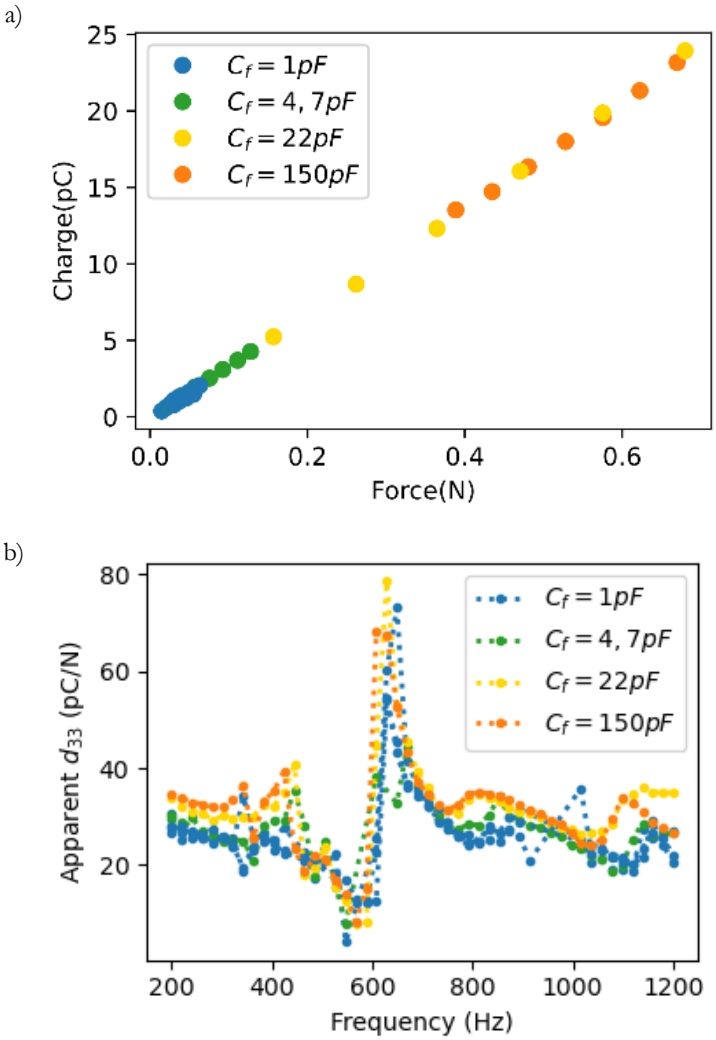

Figure 3.20 : Force-Charge measurement (a) and piezoelectric spectra (b) of PVDF, measured using the four different gains of the instrument.

3.5 CONCLUSIONS

In the context described at the beginning of the chapter emerged the need for an instrument and a technique to perform reliable and repeatable piezoelectric measurements on soft piezoelectric nanocomposites, also called nanogenerators.

The modular measuring system and characterization approach developed and described in this chapter enables the quantitative and systematic characterization on the electro-mechanical transduction ability of piezoelectric polymers and soft piezoelectric polymeric nanocomposites in the compression mode, with possible extension to the longitudinal mode. The measuring system allows to discriminate the piezoelectric contribution from the contact electrification charges [137]. Moreover, it allows to measure samples with a piezoelectric coefficient down to 0,5pC/N, and the measurements are performed under controlled and reproducible conditions for a selected range of stimuli frequencies. The bandwidth and the resolution of the measuring instrument are limited, but it can be scaled, and the reliability of the measurement can be controlled during the measure, allowing to exclude from the results spurious effects, such as mechanical system resonances and triboelectricity.

4. PIEZORESISTIVE: ELASTOMER/GOLD

The work presented in this Chapter is part of a project named "ASSIST – Smart valves based on active soft materials" funded by Fondazione Cariplo and Regione Lombardia. Politecnico di Milano, W.I.S.E. s.r.l. and Dolphin Fluidics were partners of the project. The final aim of the project was the redesign of a fluidic valve already on the market to include a flux sensor integrated in the stretchable membrane. The sensor was based on a piezoresistive metal/polymer nanocomposite layer integrated directly in the valve's membrane.

The work presented in the following chapter regards the process development of the nanocomposite for the integrated sensor, in particular for what regards the choice of the elastomer for the fabrication of the membrane and the optimization of the implantation process to produce a reliable strain sensor. A membrane mock-up integrated in the final device is presented in the last section.

4.1 ELASTOMER CHARACTERIZATION

Elastomer is a term used to define a material with rubber-like behavior, which at room temperature can be stretched repeatedly to at least twice its original length and which after removal of the tensile load will immediately return to approximately its original length [149]. This kind of materials are typically polymers above their glass transition temperature, thus having low value of Young Modulus (about 1MPa) and they are crosslinked chemically or physically.

The material mainly used in this work is polydimethylsiloxane (Sylgard® 184, Dow Inc.). The crosslinked PDMS has interesting physical and chemical properties most of them common to the siloxane polymers, it can be used in a wide temperature range (between -100 and about 200°C), it has low elastic modulus, it has low chemical reactivity, it has a hydrophilic behavior, it is transparent, it is biocompatible and has a low cost. This material is widely used in microfluidics, electronics, soft robotics and for biomedical applications.

4.1.1 Process development

In literature [150–152] it is highlighted the change in mechanical behavior of PDMS changing the production and curing conditions. In order to obtain a reproducible fabrication procedure, it is crucial to define a standardized synthesis and curing procedure that enables the production of samples with controlled mechanical and surface properties.

A Thermogravimetric analysis (TGA Q500 TA instrument) was performed to evaluate the material stability during the curing process. The liquid mixture of prepolymer and curing agent was subjected to two different thermal histories: a heating ramp (temperature increased from 30°C to 600°C at a rate of 5°C/min) and an isotherm (after a heating from 30°C to 150°C at 5°C/min the material was kept at 150°C for 180min). The thermal histories of the samples can be observed in Figure 4.1a. In Figure 4.1b is plotted the ratio between the mass of the sample and its initial value versus the temperature during the isotherm test, together with the relevant derivative curve. The corresponding for the heating ramp test is plotted in Figure 4.1c, with a zoom in Figure 4.1d.

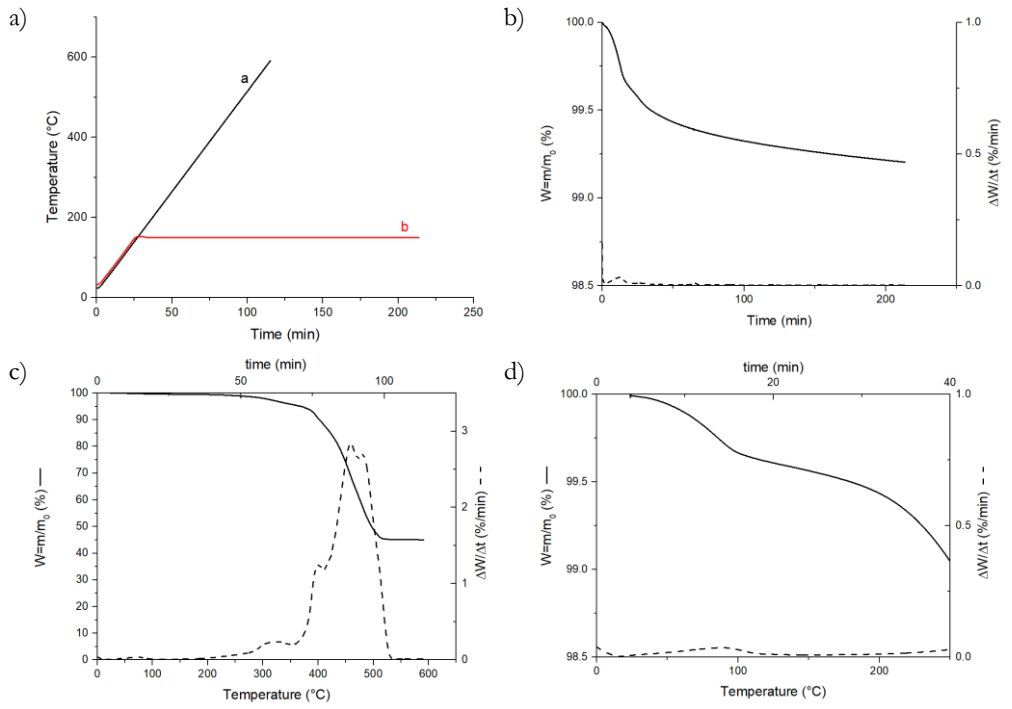

Figure 4.1: Thermogravimetric analysis of PDMS pre-polymer. Thermal history (a), isothermal test (b), heating ramp (c) and its zoom in the 0-200°C range (d).

From the results of the TGA test it was possible to state that the material is stable up to 200°C, and that most of the thermal degradation occurs between 300°C and 500°C. In the isotherm the weight loss is very small (about 0.8%) and similar to the one observed in the heating ramp, while during the isotherm step the weight loss is only 0.3%. These results suggested that the material can be considered thermically stable when the curing is performed under 200°C.

Rheological shear test during the curing process were performed with an Anton Paar Modular Compact Rheometer (MCR 502) in parallel plate configuration. A 1mm thick layer of uncured mixture wasd placed between the two plates that oscillated at 1Hz, while the sample was heated with an 8°C/min ramp up to 100°C or 150°C, followed by an isotherm step. In Figure 4.2 are plotted the two components of the shear modulus, the conservative component G' (storage modulus, solid line), and the dissipative component G" (loss modulus, dashed line), against time and temperature. The storage modulus is correlated with the structure of the polymer network thus its change with time reflects the cross-linking of the material. The so-called *gel point* is the crossover point between the storage modulus and the loss modulus, and it indicates the formation of a continuous network in the polymer. As can be observed in Figure 4.2 the gel point was reached for both curing temperatures after ten minutes of heating, and the final moduli depends on the curing temperature and not on the thermal history.

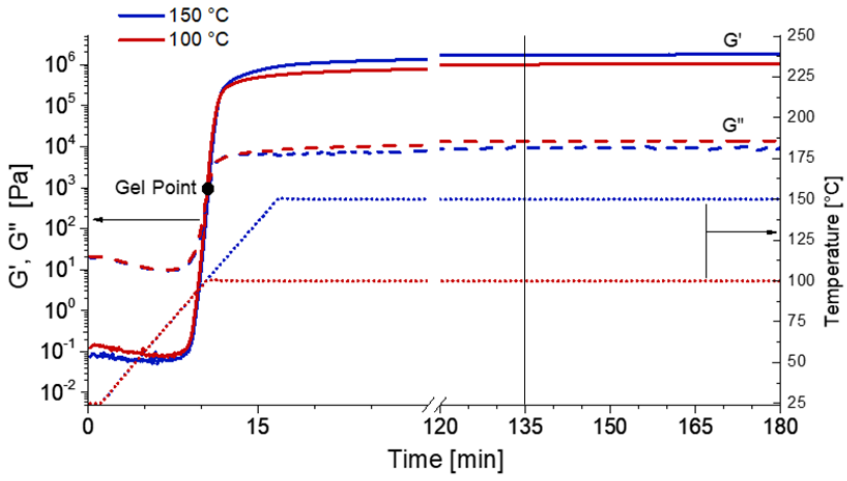

Figure 4.2: a) Parallel plates rheometer test (100°C and 150°C).

4.1.2 Mechanical characterization

For the uniaxial electro-mechanical tests the elastomer samples were cut in a dumbbell shape with 25mm gauge length (Figure 4.3).

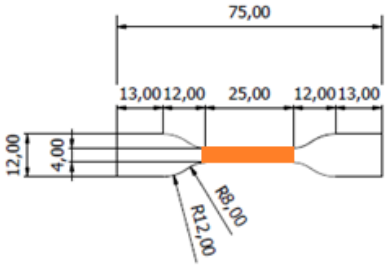

Figure 4.3: Sample shape for mechanical and electro-mechanical tests. Dumbbell (type2 ISO 37) (all quotes are expressed in millimetres).

Uniaxial tensile tests were carried out on a dynamometer (Instron 5967) with a 2kN load cell N. A nominal strain rate of $0.24mm^{-1}$ was applied. Normal forces and displacements were automatically recorded by the machine. Nominal stresses were evaluated as: $\sigma_n = F/A_0$, with A_0 is the undeformed cross-section of the specimens and F is the normal force. The tests were video recorded with uEye camera and photographic lens Nikon AF Nikkor 28-105mm in order to measure accurately the effective strains. Four equally spaced lines were drawn in the specimen length perpendicularly to the loading direction to compute the actual deformation of the gauge length, by evaluating the evolution of the lines' distance L during the test. The deformation was therefore computed as:

$$\varepsilon_n(t) = \frac{L(t) - L(t_0)}{L(t_0)}$$

As expected, the deformation resulted to be practically uniform in the gauge length.

A DOE (Design Of Experiment) performed by the project partners allowed to define the influence of the various curing parameters on the mechanical behavior of the elastomer. The curing condition were then defined as follows: the pre-polymer gel and the cross linker are mixed at a 20:1 (w/w) ratio. The mixture is poured into a metal mold and degassed thoroughly. The PDMS is cured in a pre-heated oven at 125 °C for 75 min and cooled down at room temperature. A 500µm film was obtained and tested mechanically through uniaxial strain tests. As shown in Figure 4.4 the material presented an elastic behavior up to a strain of 40%, while at larger strain the material had a hysteretic behavior. Further, the material showed the

Mullins effect typical of filled rubbers [153]: in each cycle, the loading curve overlaps the unloading one of the previous cycle. This represents a softening of the stresses up to the maximum strain value reached in the previous test.

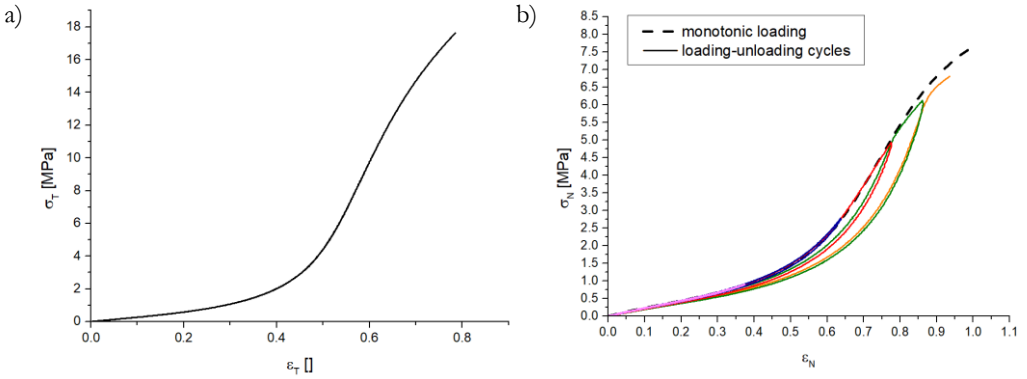

Figure 4.4: Monotonic loading and cyclic loading and unloading of a PDMS sample. In b) can be observed the Mullins effect, typical of elastomers.

For the purposes of the project, in particular the necessity of a bio-compatible material, a different material than PDMS was selected: silicon sheets of Sil540080T, an elastomer already cross-linked. The mechanical uniaxial tests were repeated on this material (Figure 4.5). As can be observed in Figure 4.5b this material exhibits the Mullin's effect up to the maximum strain reached in the previous cycle. Tests performed after 24h and after one month demonstrated that this softening is not reversible. Cyclic tests demonstrated that the softening of the matrix was completely reached after the first cycle.

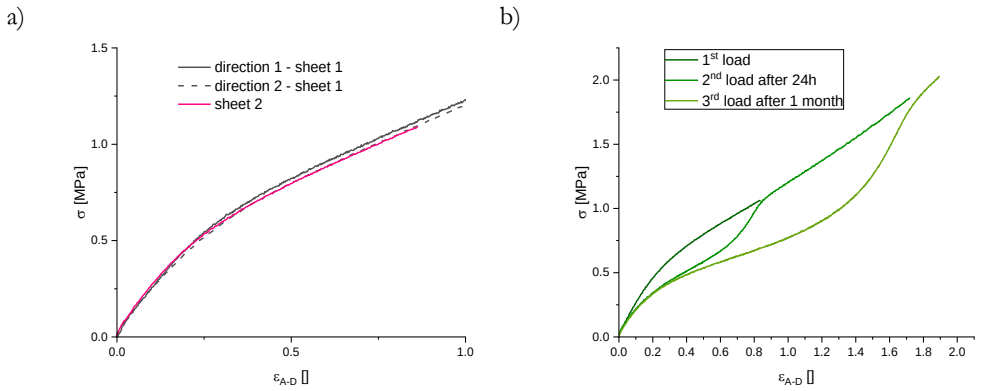

Figure 4.5: Monotonic loading and cyclic loading and unloading of a Sil540080T sample. In b) can be observed the Mullins effect, typical of filled rubbers.

4.2 SCBD AND PERCOLATIVE CURVES

The Supersonic Cluster Beam Deposition technique [154–156] is based on the implantation of neutral metal nanoclusters, accelerated by a supersonic aerodynamical flow using a carrier gas, into the polymer matrix. The deposition takes place at room temperature and low energy, a high deposition rate, high lateral resolution compatible with planar microfabrication technologies, and neutral particle mass selection process by exploiting aerodynamic focusing effects [157]. This avoids thermal or chemical damage of the samples. As a result, this leads to the formation of large surface area nanostructured electrodes with controlled morphology at the nanoscale. The electrodes deposited with this technique are excellently adherent to the polymer matrix and do not significantly alter the mechanical properties of the nanocomposite, which is a salient feature for the desired application.

4.2.1 Supersonic Cluster Beam Deposition

A typical SCBD apparatus is schematically shown in Figure 4.6. The source used to obtain intense and stable neutral supersonic cluster beams is the Pulsed Microplasma Cluster Source (PMCS) [158,159]. The PMCS principle of operation consists of the ablation of a metal target rod by a plasma ignited during the injection of a high-pressure pulse of an inert gas (Argon or Helium). The species resulting from the target ablation condense through collision with the inert gas to form clusters, then the cluster-gas mixture is expanded through a nozzle generating a supersonic seeded beam [160]. The cluster beam is focused by an aerodynamic lenses system [161] and directed on a substrate placed in a deposition chamber. The lenses force the gas flow lines to abruptly change when the gas passes through the orifice, obtaining a series of contractions and expansions during the passage through the focuser stages. Each metallic particle follows the streamlines of the flow originated at the lens nozzle depending on its inertial properties. A quartz microbalance periodically monitors the amount of deposited material and the deposition rate, and it allows to make an estimation of the nominal thickness of the films. High directionality, collimation, and intensity of aerodynamically focused supersonic cluster beams make them well suited for patterned deposition of nanostructured films through non-contact stencil masks or lift-off technologies [162,163].

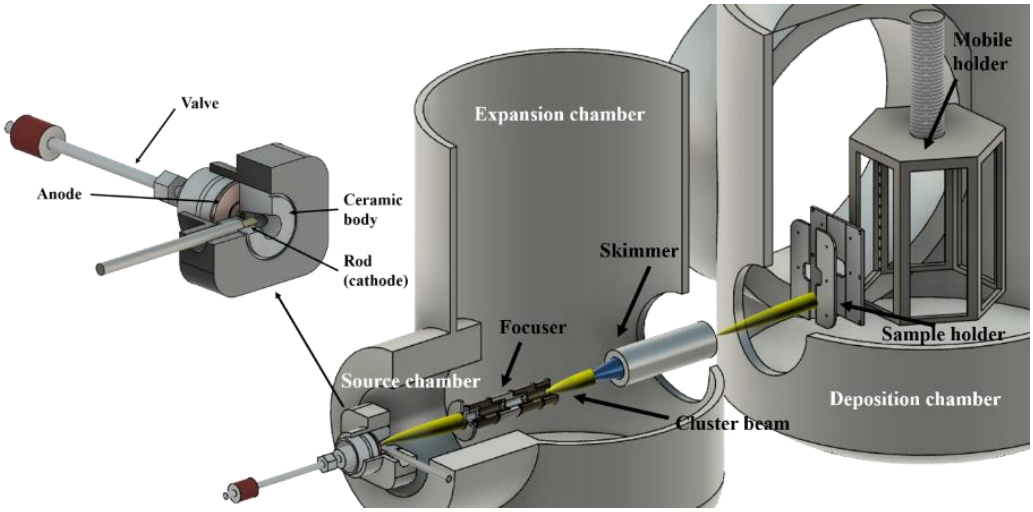

Figure 4.6: Scheme of the SCBD experimental apparatus. Clusters are produced in the source chamber and then extracted into the expansion chamber where they undergo a process of aerodynamical focusing. The focused beam arrives to the deposition chamber, passing through a skimmer. The cluster are deposited on the substrate mounted on the mobile holder. On the top left, an insight of the PMCS. The ceramic body consists in a cylindrical cavity where the gas injection is controlled by a pulsed valve. Between the ceramic body and the valve, a metallic disk, the anode is placed. The cathode, a gold rod, is inserted into the cavity through one lateral hole.

4.2.2 Percolation Curves

The percolation theory described in Section 2.2.2 can be applied both to the conduction mechanisms of the nanoparticles embedded inside the polymer matrix, and the growth of the conductive layer of gold nanoparticles across the polymer surface. The latter is of particular interest for process optimization purposes.

The evolution of the electrical properties of cluster-assembled films can be characterized in situ during the fabrication process: in Figure 4.7 is shown a scheme of the experimental setup. The PDMS sample is mounted on a holder equipped with electrical contacts for the in-situ characterization of the evolution of the electrical properties of the film during the deposition process. The electrical resistance of cluster-assembled films is measured in the two-probe configuration [164] through a digital multimeter (Agilent 34410A) remotely controlled by a computer and the measurement is automatized through a LabView script.

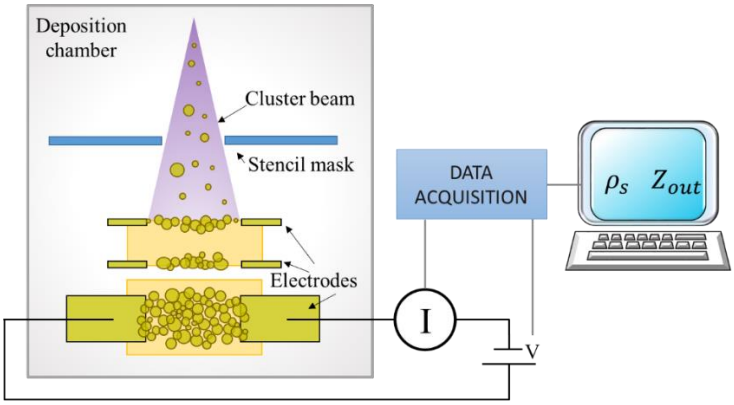

Figure 4.7: Experimental set-up used for in-situ resistance measurements during the Supersonic Cluster Beam Deposition process.

From the study of the percolation curve during the conductive layer's growth it is possible to derive some important insights on the growth process. The critical thickness for the electrical percolation threshold, corresponding to the film morphology, can be determined by the occurrence of the maximum slope of the conductivity vs. thickness curve [165]. Beyond the percolation transition, the cluster-assembled film is fully connected. In order to determine the thickness t_* at which the transition to an ohmic behaviour takes place, the minimum of the curve Rt^2 is searched, where R is the electrical resistance and t the thickness [166].

In order to highlight the differences that different processes can have on the percolation curve, in Figure 4.8 have been plotted the evolution of the electrical properties of some typical systems. The atom-assembled film on silicon (in blue) showed a percolation threshold below 10nm, the cluster-assembled film on the same surface (the two curves in green) showed higher percolation values, at thickness 10-20nm. A cluster assembled film deposited but not implanted in PDMS (in yellow) showed a threshold percolation value at nominal thicknesses of 10nm. Cluster assembled film implanted in PDMS (in orange and red) showed percolation values respectively at nominal thicknesses of 40nm, 140nm and 200nm depending on the PDMS mechanical properties and the deposition conditions. As can be observed from the comparison plot not only the percolation threshold wase different, but also the transition to ohmic behaviour and the critical exponent t introduced in Section 2.2.2 presented a significative difference from one curve to the other.

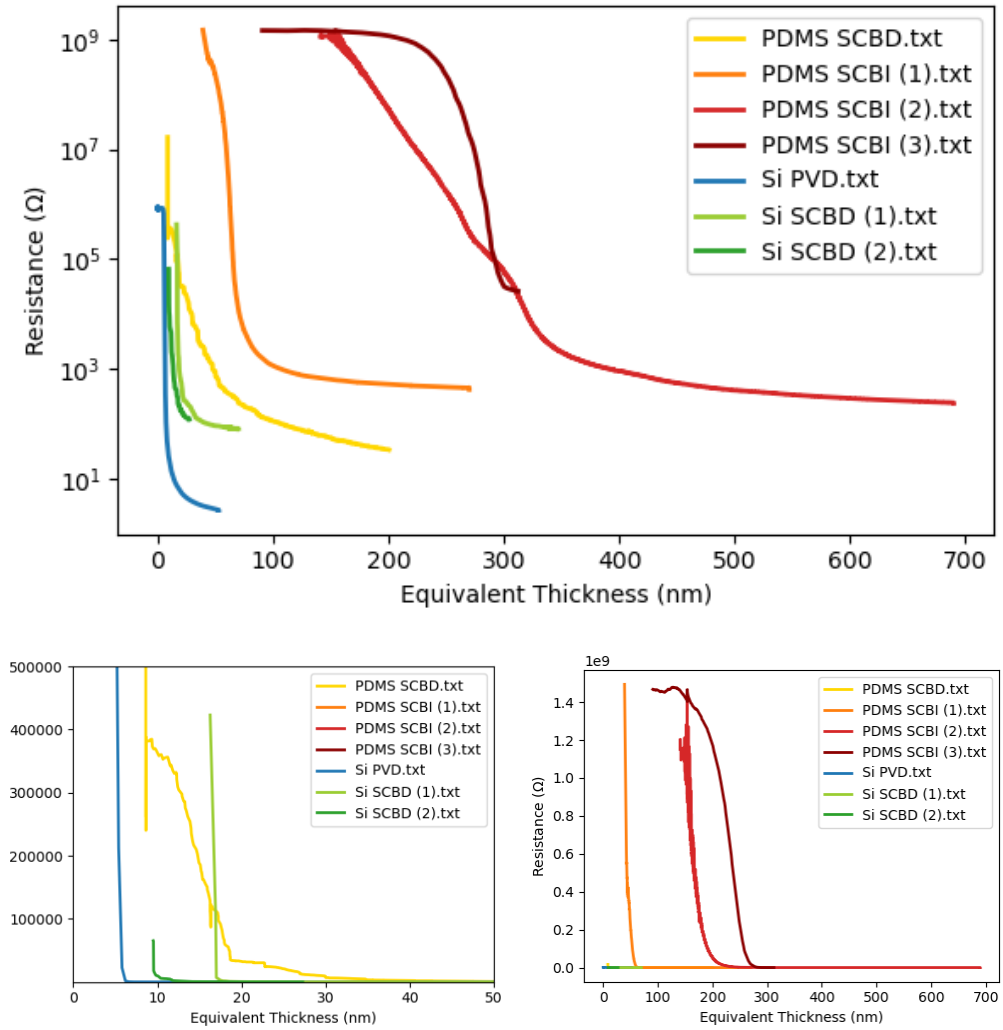

Figure 4.8: Comparison between different percolation curves in logarithmic scale (top) and linear scale (bottom).

The morphology of an atom-assembled film on PDMS is reported in Figure 4.9a, showing the typical structure expected for a film assembled by atoms [167], with evident differences with respect to the cluster film morphology in the continuous regime (Figure 4.9b). The images have been acquired using an Atomic Force Microscopy (AFM) in tapping mode, using rigid silicon cantilevers mounting single crystal silicon tip with nominal radius 5–10 nm and resonance frequency in the range 250–350 kHz.

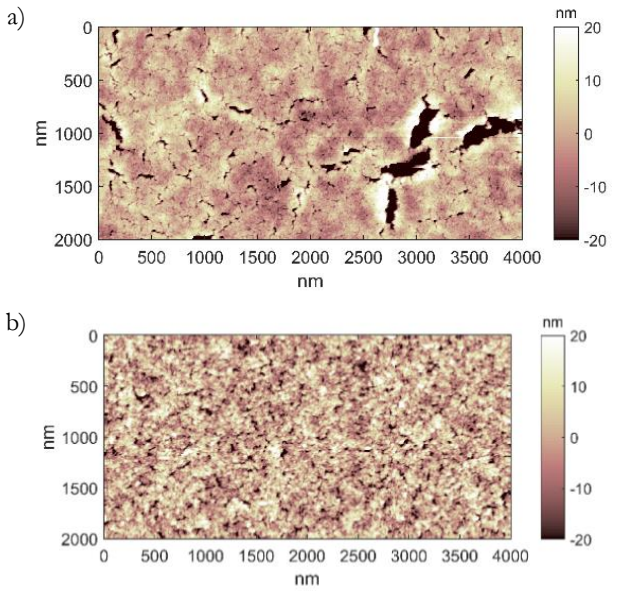

Figure 4.9: AFM maps of thin layer of gold deposited on PDMS through Physical Vapor Deposition (a) and Supersonic Cluster Beam Deposition (b)

In Figure 4.10 are presented some percolation curves acquired on different substrates and with different deposition parameters. In Figure 4.10a and b are plotted percolation curves acquired during different deposition with low deposition rates on PDMS with different mechanical properties. The PDMS in Figure 4.10a was softer (mixing ratio 1:20, curing temperature 125°C, curing time 75min), while the one in Figure 4.10b was stiffer (mixing ratio 1:10, curing temperature 80°C, curing time 135min). In Figure 4.10c and d are reported the percolation curves acquired using as target Sil540080T. In Figure 4.10c the deposition parameters are the same as in Figure 4.10a and b, while in Figure 4.10d a different metal was used (Platinum) and the process was performed with a high deposition rate.

As can be observed from the curves in Figure 4.10a, b and c the process was reproducible, as the percolation thresholds and behaviors were similar. The extreme difference in the percolation thresholds of the percolation curves reported in Figure 4.10a and b suggest that the matrix stiffness is a crucial element in the implantation process, i.e. the softer matrix allows a deeper nanoparticle implantation, therefore the percolation threshold is shifted to higher equivalent thicknesses.

The sample deposited with platinum, reported in Figure 4.10d, showed a percolation threshold before 20nm, therefore it is likely that there was none or very little implantation during the process. In Figure 4.10b the two curves were acquired

with different deposition parameters, and this explains the difference in their percolation behavior, which is furtherly analyzed in the next paragraph.

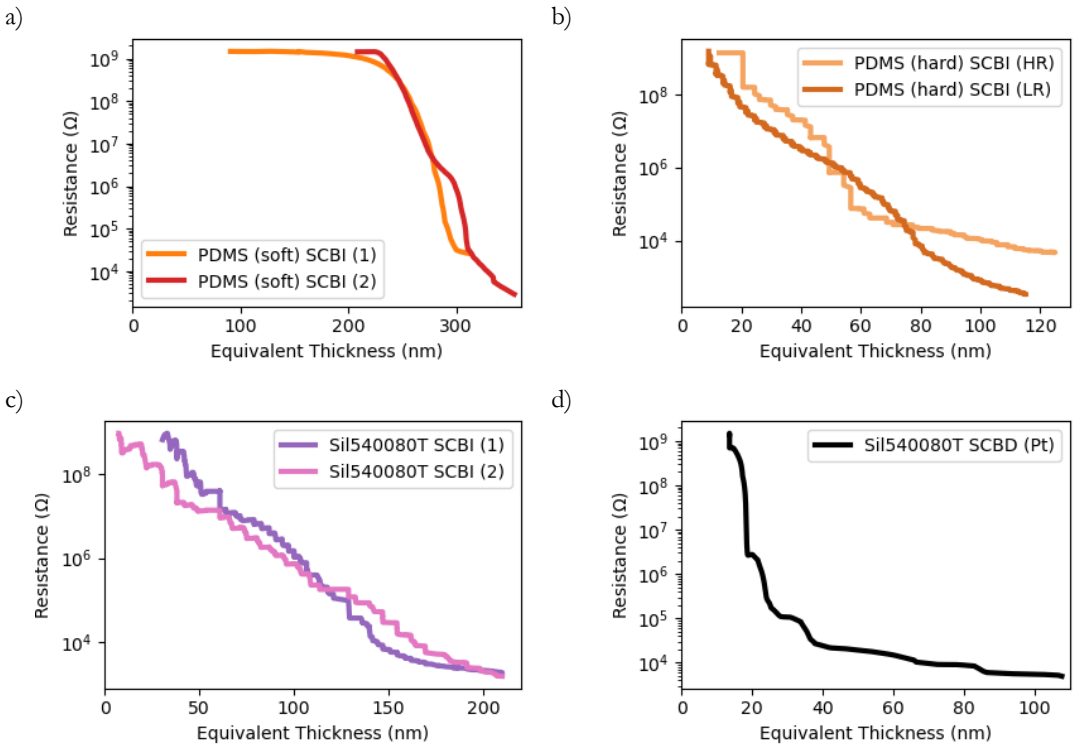

Figure 4.10: Some percolation curves, various conditions and different elastomers. a) Soft PDMS (base : curing agent = 1 : 20, cured at 125°C for 75 minutes), low deposition rate. b) Hard PDMS (base : curing agent = 1 : 10, cured at 80°C for 135 minutes), different deposition rates. c) Sil540080T, low deposition rate, d) Sil540080T, high deposition rate, platinum deposited.

The influence of the deposition rate on the percolative curve that can be observed in Figure 4.10b has been studied also in terms of roughness, by means of AFM.

	Roughness [nm]	Thickness [nm]
Glass high rate	9.7 ± 0.1	122 ± 8
Glass low rate	9.5 ± 0.1	115 ± 5
PDMS high rate	8.9 ± 0.1	210 ± 15
PDMS low rate	7.2 ± 0.1	240 ± 30

Table 4.1: Roughness and thickness, AFM measured, of gold nanostructured layers deposited on PDMS (the relative percolation curves are reported in Figure 4.10b) and glass.

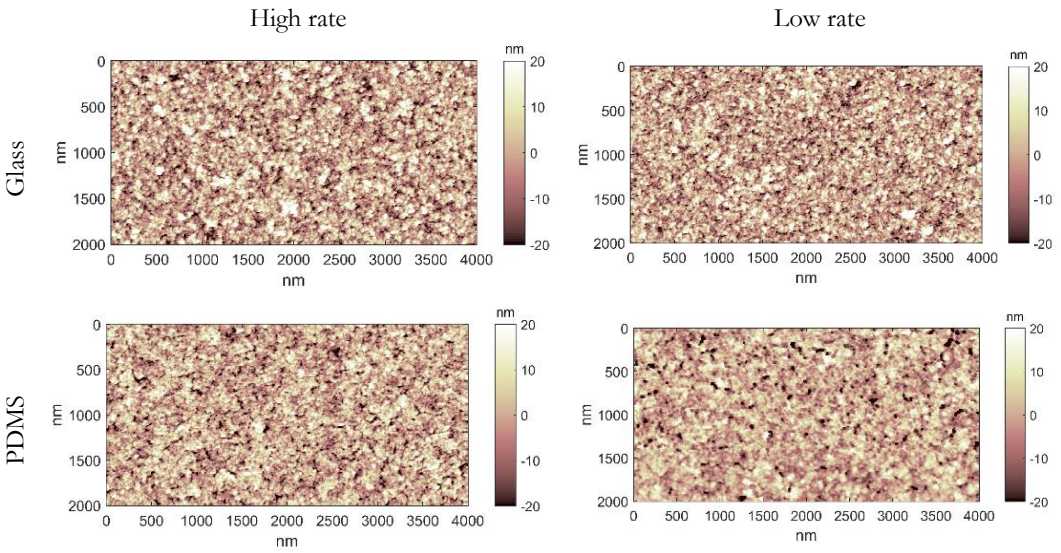

Figure 4.11: AFM maps of nanostructured gold deposited on glass and PDMS with two different rates.

As can be observed in Figure 4.11 and in Table 4.1 while the deposition conditions have little or no effect on glass sample (both the roughness and the thickness were very similar), in PDMS the deposition rate had a significant effect. A lower rate lowered the roughness (in this case the roughness is lowered of 20% compared to the 2% for glass) and increased the thickness (12,5% against 6%). This effect can be ascribed to a deeper implantation, that swells more the elastomer, increasing the thickness of the PDMS/elastomer interphase. Furthermore, it has been demonstrated that for this technique the thickness and the roughness of the nanostructured layer are strongly correlated [168]; therefore, the lower roughness of the sample deposited at low rate suggests that the emerged section of the nanostructured gold was thinner than the one for the sample deposited with a high deposition rate.

4.2.3 Conclusions

The percolation curves acquired allowed to observe the difference between deposition (2D percolation) and implantation (3D percolation). One indicator of the depth of the implantation is the shifting of the percolation threshold towards higher equivalent thicknesses, and another is the thickness necessary to reach an ohmic conduction, i.e. a continuous conductive network. It is probable that for this kind of materials other phenomena arise. In particular many surface effects can happen, that might generate two different percolation thresholds: one on the surface, and one inside the polymer matrix. The interplay between these two

percolations depends on the deposition conditions (in particular the deposition rate) and the mechanical and surface characteristics of the material. The surface roughness comes also into play, in particular for what regards surface percolation, even though for the materials reported in this chapter should not be a relevant factor. A deeper understanding of the deposition and implantation process requires further studies.

It should emerge from the discussion of these results how percolation curves are a useful tool to gain insights on what is happening at a nanoscopic level and to define the most appropriate conditions for the conductive nanostructured level growth process. For the purpose of the project a conductive material was needed, so it was crucial to reach a continuous layer, i.e. the third phase of the percolation process as defined in Section 2.2.2. At the same time, in order to improve the sensitivity of the piezoresistive sensor, depositing too much after the reaching of the ohmic regime would have been ineffective. Therefore, the optimal thickness was expected to be around the end of the percolative curve.

4.3 ELECTRO-MECHANICAL CHARACTERIZATION

The mechanical tests were performed as described in Section 4.1.2, with a nominal strain rate of $0.24mm^{-1}$ and a 2kN load cell. The electrical resistance of the sample was measured through a digital multimeter (Agilent 34410A) in two-probe configuration. The measure was automated by a dedicated LabView program. The three acquisitions (force, displacement, resistance) were synchronized with a data sampling of 10Hz. Thin steel wires were secured on the nanostructured gold layer with a conductive silicone based on Nickel particles (Soliani EMC S.p.a.) in order to assure electrical contact (Figure 4.12a).

4.3.1 PDMS

The first sample tested was a soft PDMS (mixing rate 1:20, curing 75 minutes at 125°C) with a 200nm Au layer deposited with high rates. A single load test up to 60% strain was performed, in order to assess the influence of the implanted gold nanostructured layer on the material's mechanics, the shape of the resistance response and the stability of the electrical contacts. As expected, the gold implanted layer did not change the mechanical response of the material (Figure 4.12b). The resistance of the material evolved significantly with the applied strain, reaching a

maximum resistance of 14kΩ at 60% strain from the initial 430Ω. The gauge factor at maximum strain for this first cycle can be calculated as:

$$GF = \frac{(R_{max} - R_0)/R_0}{\varepsilon_{max}} = \frac{(14000\Omega - 400\Omega)/400\Omega}{0.60} = 57$$

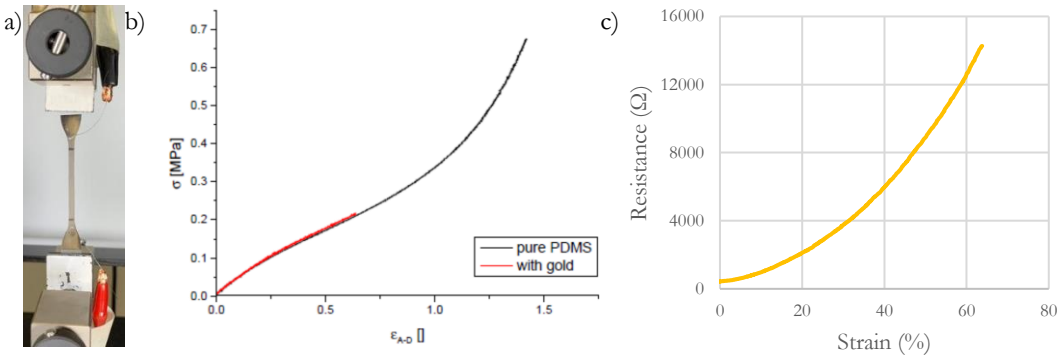

Figure 4.12: a) Test set-up b) Strain-stress curve for pristine PDMS and PDSM with an implanted gold-layer. c) Load cycle: strain-resistance curve.

A first multi-cycle test, up to a nominal deformation of 20% (Figure 4.13), showed a decrease in the piezoresistive response. This effect had already been reported in [169] and has been explained as a rearrangement of the nanoparticles inside the polymer matrix, and, as can be observed in Figure 4.13c, the gauge factor decreases with increasing cycle number. It is expected that with increasing number of cycles a stable conductive path can be formed and a maximum resistance plateau, and therefore a stable gauge factor, can be reached. A small hysteresis is also present. The response of the sensor with strain was not linear, but it is monotonic and has a non-zero slope in every point, so it was suitable for sensor applications.

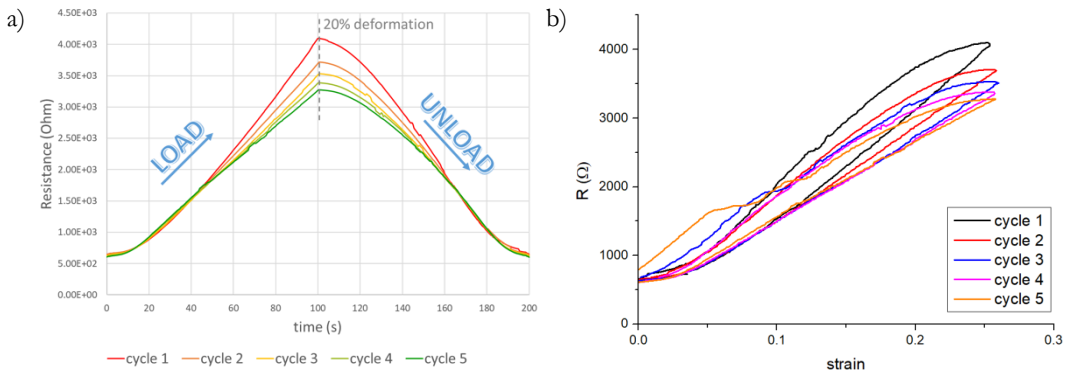

Figure 4.13: Uniaxial strain cyclical measurements. a) Resistance-time, b) resistance-strain.

4.3.2 Sil540080T

In order to define the best implantation protocol on Sil540080T some tests were performed with different implantation conditions and similar thicknesses, in particular at the end of the percolation regime as discussed in Section 4.2.3. The samples were tested with 10-cycle uniaxial strain measurements, which results are reported in Figure 4.14, in order to assess their piezoresistive performance. The gauge factors at 45% strain at the 10th cycle presented similar values (Table 4.2). The conditions that provided the most stable response was chosen for the production of samples for multiple cycle measurements.

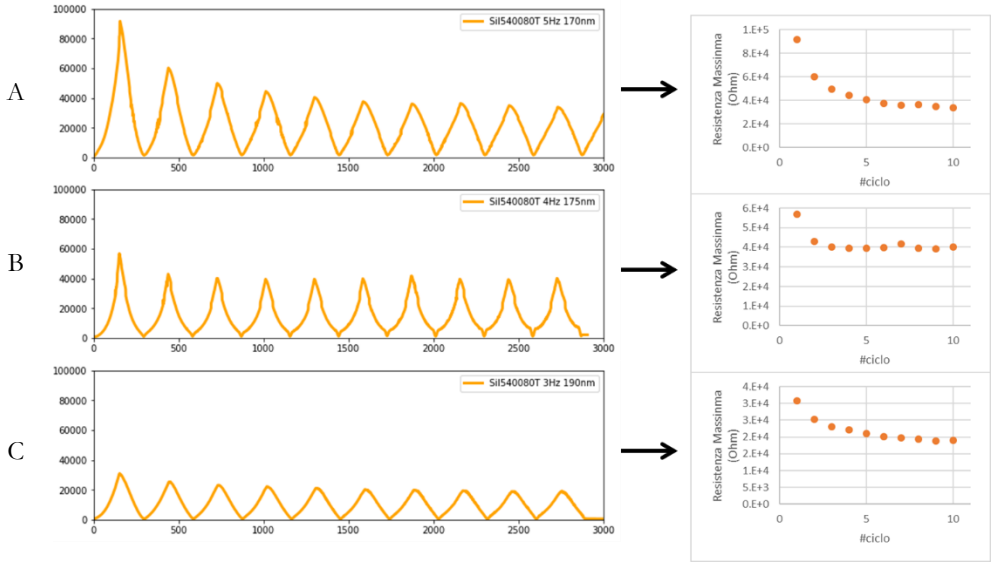

Figure 4.14: 10-cycle strain-resistance measurements with Sil540080T implanted with different deposition parameters.

Sample	Cycle	R/R0	ε max	GF =[R-R0/R0]/ ε max
SIL540080T - A	1	118.05	0.47	251.17
	10	53.7	0.47	114.25
SIL540080T - B	1	68.43	0.42	162.93
	10	48.01	0.42	114.31
SIL540080T - C	1	79.84	0.42	190.09
	10	47.55	0.42	113.21

Table 4.2: Gauge factor at 1st and 10th of strain-resistance measurement up to 45% strain for Sil540080T implanted with different deposition parameters.

In order to decouple the piezoresistive response reading from the stretching of the electrical contacts, and therefore to be able to isolate the resistance change occurred in the gauge section of the sample, a new shape for the specimen under test was studied, in order to position the electrical contacts in sites that are subjected to a low stress during the test. The chosen shape was a double T specimen with 18mm gauge length (Figure 4.15), and the contacts were positioned along the gauge length axis, separated by 30mm, compared to the 13mm of the gauge length. The mechanical simulation reported in Figure 4.15a was performed using the Mooney-Rivlin model with a 5mm displacement along the gauge length axis.

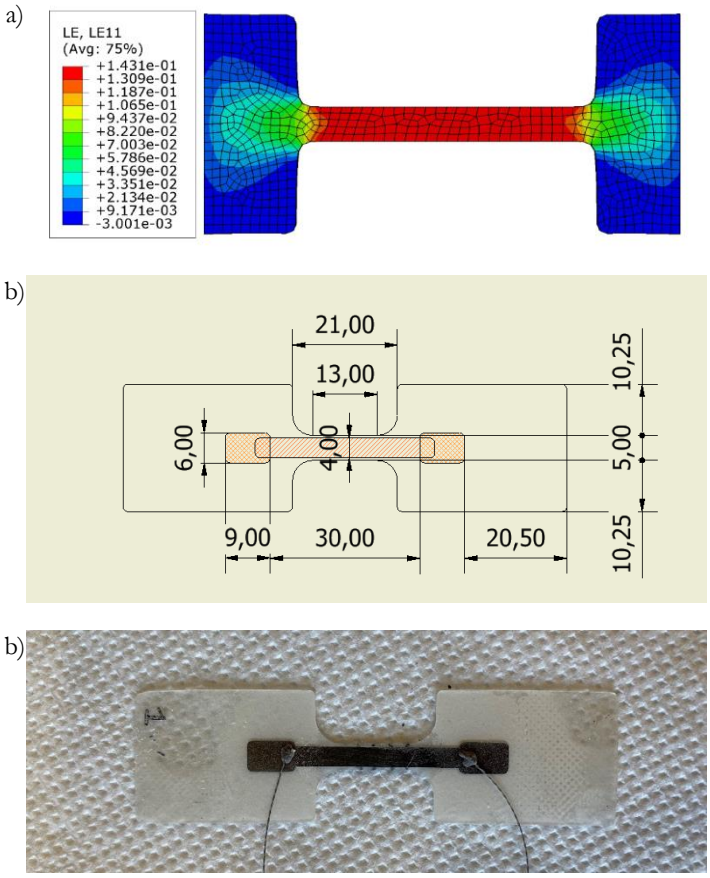

Figure 4.15: a) Mechanical simulation of the specimen design, b) Schematic of the sample, in orange the deposited layer, c) photograph of the sample with electrical contacts placed in the designated spots.

With this configuration it was possible to obtain a stable electrical signal. The sample was tested for 50 cycles (Figure 4.16a), and then after 2 hours for other 150 cycles (Figure 4.16b). The acquired signal remained stable for all the 200 cycles and it

appeared to be reaching a plateau value for the maximum value of resistance. In Figure 4.16c can be observed, superimposed, the three curves of stress, strain and relative resistance for this test. As can be observed the piezoresistive response was almost linear, and the correlation between the three curves was really promising for a sensor application.

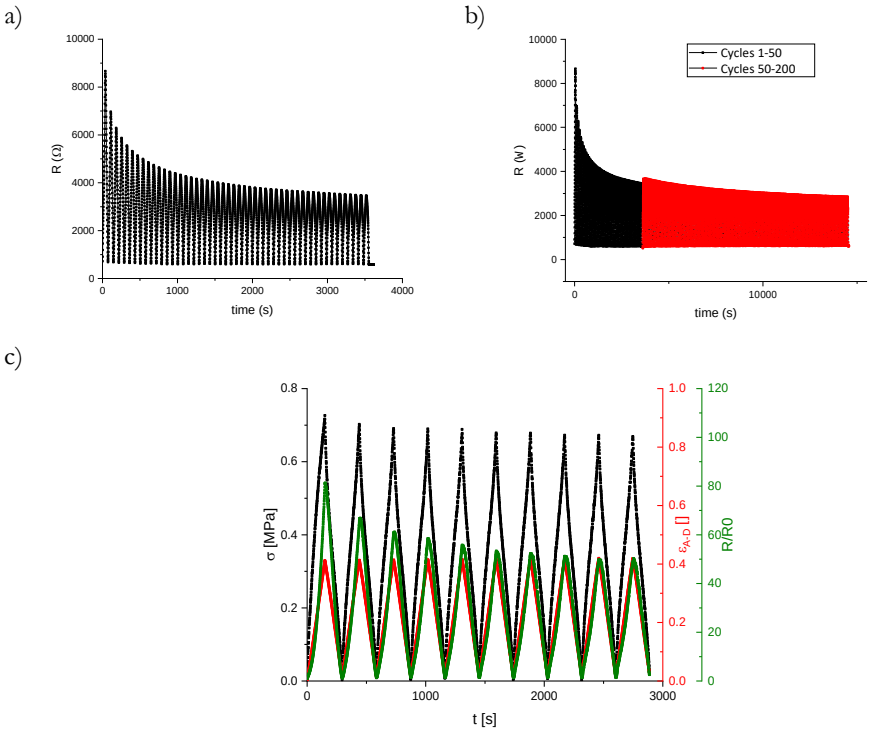

Figure 4.16: a) 50 load-unload cycles b) 150 load-unload cycles c) correlation between resistance, strain and stress.

4.3.3 Sil540080T-Platinum

For biocompatibility and scalability of the process in already operating industrial facilities, it was performed a trial with Sil540080T implanted with Platinum (Pt) with high thicknesses. The results, reported in Figure 4.17, were not particularly promising, mainly because of the shape of the resistive response. In particular at high strains the resistivity reached a plateau (in this case the material was tested up to 15% strain); moreover, the resistive response had a zero-slope around the beginning of the curve (low strains) and therefore gave the sensor a low resolution. Another observation that can be made from Figure 4.17 is that resolution of the sample with a higher quantity of platinum was significantly lower than the one with less platinum, which is in accordance with the hypothesis that depositing over the

ohmic regime is ineffective because it minimizes the resistivity change for low strains, which is inadequate for sensing applications. The gauge factor was not calculated for these two samples due to their high dependence on the applied strain.

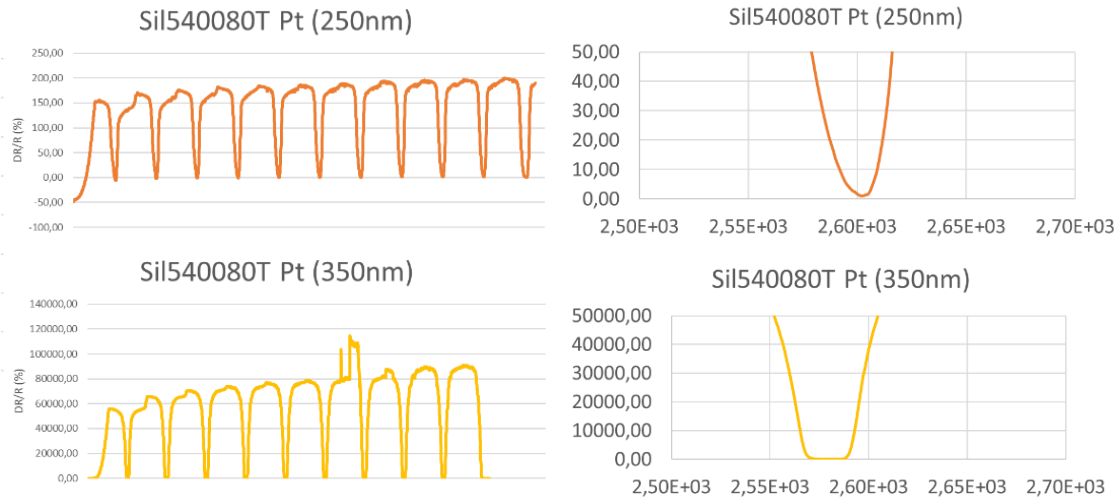

Figure 4.17: 10-cycle strain-resistance measurements with Sil540080T implanted with platinum (high thickness).

4.3.4 Device mock-up

In the framework of the project a mock-up of the functioning device was implemented and tested, in order to verify the functioning of the sensing membrane integrated in the fluidic valve concept.

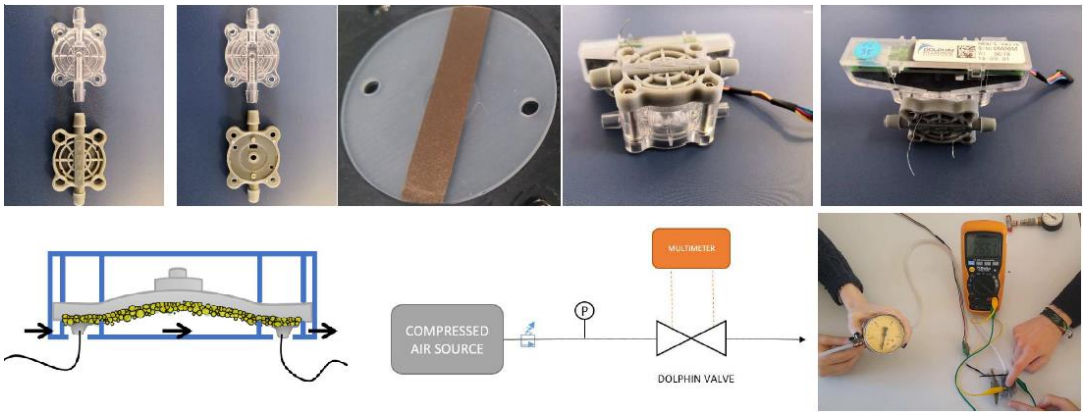

Figure 4.18: Photographs and schematic representation of the system and the mock-up membrane (top row), functioning principle of the valve (bottom left) and schematic (bottom center) and photograph (bottom right) of the test set-up.

The membrane with the gold implanted layer was integrated in the valve (Dolphin Fluidics 18-00-01) and contacted with the outside through thin wires passing through two holes in the 3D printed scaffold. The resistance was measured with a MM01 digital multimeter while the fluidic circuit was activated with compressed air, controlled through a mechanical pressure reducer and measured with a Bourdon manometer (0÷4 bar). The test was performed by increasing gradually the pressure from 0 to 1.6bar and back and reading the resistance response on the multimeter.

The resistance varied coherently with the pressure from. 265.1Ω to 285.8Ω, and back to 270.6Ω, with a variation of 8% on one way and 6% back. The strain of the membrane was not known so it was not possible to calculate the gauge rate for this test.

The results of the mock-up test were promising and demonstrated the concept of the sensorized membrane integrated in the valve.

4.4 SUMMARY AND CONCLUSIONS

The work presented in this chapter regards the process development of the fabrication of a sensorized membrane to be incorporated inside a commercial fluidic valve for integrated pressure sensing. In particular the work presented was focused on the choice of a suitable bio-compatible elastomer, and the optimization of the implantation process to fabricate a reliable strain sensor.

An optimized procedure for the production of mechanically reproducible PDMS samples with the desired mechanical properties was developed. The study of percolation curves during the thin film growth of Supersonic Cluster Beam Deposited metal on various elastomer matrixes allowed to gain insight on the implantation process on such materials. Furthermore, it was crucial in order to develop an optimized process for the fabrication of an elastomer/metal nanocomposites for the piezoresistive membrane. The electro-mechanical measurements performed on sample specimens and a membrane mock-up showed promising results and demonstrated the concept of the sensorized membrane.

4.5 FEMTOLASER / SCBD GOLD MICROELECTRODES

The process optimization and standardization presented in the current Chapter was exploited for the production of electrically and mechanically reproducible substrates

for the fabrication of soft and flexible microelectrodes. In this work, femtosecond (fs) laser ablation was used for patterning a PDMS/Au nanocomposite film. Ultrashort laser ablation is unique in its capabilities of high spatial precision, minimal collateral thermal damage, high material removal rate, selective ablation of thin layers and the capability of processing a large range of materials. Microelectrodes were fabricated with a width down to 3μm. The printed metal line sheet resistance was 480 Ω /sq for the 100 nm thick film and 210 Ω /sq for the 200 nm thick film. The calculated average film specific resistivity was found to be 2.5–2.6mΩ·cm. It is ~3 orders of magnitude higher than that of physical vapor deposited gold; therefore, it was not suitable for high current interconnects but sufficient for low-current signal transmission such as for electrical and electrochemical biosensors. For a deeper discussion see Appendix B (ref. [170]).

5. $BaTiO_3$ NANOCOMPOSITES

As presented in Sections 2.1.3.3 and 3.1.3 the field of piezoelectric polymeric nanocomposites is widely researched, and many materials are reported each year, usually varying the different ingredients (polymeric matrix, nanofiller, electrode types and other additives). The use of large volume fractions of the piezoelectric nanofiller usually involves a drastic decrease in compliancy and flexibility of the composite with respect to the pristine polymer and often results in a nonhomogeneous dispersion of the nanostructures in the polymer matrix.

In this section will be presented a procedure to fabricate piezoelectric nanoparticles with surface functionalization that makes them well dispersible in aqueous solutions (5.1.2) and lipophilic solvents (5.1.3), and three different kinds of nanocomposites fabricated and/or characterized during the PhD project employing such nanoparticles. The Barium Titanate nanoparticles were synthetized and provided by the research group of Professor Mauro Comes Franchini, within Università Statale di Bologna (UNIBO).

5.1 PIEZOELECTRIC NANOPARTICLES FABRICATION

Ferroelectric perovskites nanoparticles, such as barium titanate nanoparticles ($BaTiO_3$ NPs) are one of the most exploited systems since they are easily prepared with good yields, and they present a net polarization due to their polar structure. Unfortunately, $BaTiO_3$ NPs showed poor dispersion properties in common solvents, mostly due to aggregation induced by surface instabilities, which severely limits their incorporation in polymer matrices. To overcome this issue the surface of the nanoparticles may be coated with suitable ligands: hydrophilic or lipophilic depending on the desired application. A catechol functionality presents great affinity for $BaTiO_3$ NPs surface [171], thus stabilizing the nanoparticles against aggregation, whereas a long-chain tail is of great help in redispersion of nanoparticles in solvents. By mixing these features a suitable ligand could be obtained.

5.1.1 $BaTiO_3$ nanoparticles

The nanoparticles' size and crystallinity are very important features to confer piezoelectric behaviour to polymer-based nanocomposites [61,136][61]. $BaTiO_3$ NPs were synthetized according to the literature with small modifications [173] via the sol-precipitation method at atmospheric pressure and were obtained as a fine white powder.

In a typical procedure, 938 μL of titanium tetraisopropoxide (900 mg, 3.17 mmol) were dissolved under inert atmosphere in 1.5 mL of isopropanol at room temperature in a 5 mL round bottomed flask equipped with magnetic stirrer. Then, 1 g of $Ba(OH)_2 \cdot 8\ H_2O$ (3.17 mmol) was added, and $BaTiO_3$ NPs have been allowed to form by heating up to 80°C in 30 min and leaving the solution at 80°C for 1 h. After the reaction is cooled down to room temperature, the obtained nanoparticles were centrifuged (15 min at 6000 rpm) and repeatedly washed with H_2O to remove solvent and by-products. Finally, $BaTiO_3$ NPs have been dried under vacuum to afford a fine white powder stored under inert atmosphere to avoid the formation of carbonates on the surface.

5.1.2 Hydrophilic functionalization: $BaTiO_3$-HCA

The $BaTiO_3$ NPs synthetized as described in the previous section showed poor dispersion properties in water, mostly due to aggregation induced by surface instabilities. Hence, the surface of the nanoparticles was coated with HCA, by exploiting the catechol functionality of the ligand: HCA acts both as stabilizer and as water-dispersing agent (Figure 5.1).

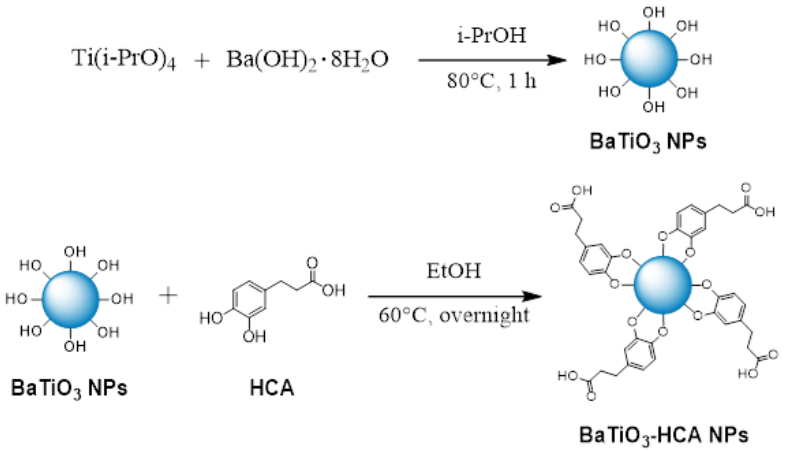

Figure 5.1: Schematic representation of the synthesis of $BaTiO_3$ NPs (top) and the ligand exchange reaction with HCA (bottom).

The reactive surface of $BaTiO_3$ NPs has been covered with 3,4-dihydroxyhydrocinnamic acid (hydrocaffeic acid, HCA). 0.577 g of $BaTiO_3$ NPs have been redispersed in 50 mL of absolute ethanol. In order to ensure complete disaggregation of the NPs, the suspension has been treated with tip-probe ultrasonicator (600W, 70% amplitude) for 1 min. Then, 0.860 g of HCA have been added to the suspension, which has been further ultrasonicated for another 1 min. Hence, the mixture has been stirred at 60°C overnight to ensure the HCA attachment. Purification of the final mixture was performed by repeated centrifugation (15 min at 6000 rpm) and washed with ethanol/water mixture (1:1), until colourless supernatant was obtained. Finally, the obtained $BaTiO_3$-HCA NPs have been collected in 5 mL of H_2O, leading to a uniform orange suspension of NPs.

Indeed, after surface functionalization, the particles showed higher dispersibility in aqueous media. Thermogravimetric analysis and dynamic light scattering (DLS) on the NPs were also performed to assess the ligand exchange reaction and the formation of an organic layer bearing deprotonated carboxyl groups.

Transmission electron microscopy (TEM) imaging was performed by an aberration-corrected probe in a TEM (JEOL JEM-ARM200F). TEM revealed the presence of particles of 30-50 nm in size (Figure 5.2a), with the crystal planes clearly visible (Figure 5.2b). The crystalline structure of the obtained NPs was confirmed by powder X-ray diffraction (XRD) on the dried NPs (Figure 5.2c). However, the small size of the $BaTiO_3$ crystal domains caused XRD peaks broadening, thus limiting the possibility to distinguish between the cubic and the tetragonal crystalline phase, the latter being the most stable at room temperature.

DLS measurements were performed on a Malvern Zetasizernano-S working with a 532 nm laser beam. ζ potential measurements were conducted in DTS1060C-Clear disposable zeta cells at 25 °C. DLS analysis of $BaTiO_3$-HCA NPs revealed an average hydrodynamic radius of 296.1 ± 3.9 nm, high monodispersity (PDI = 0.112 ± 0.014) and negative surface Zeta potential (- 37 mV), confirming the presence of deprotonated carboxylic residues on the NP surface.

As reported in Table 5.1, differences in the XRD reflections of cubic and tetragonal phases are only related to the peak splitting observed in the tetragonal phase due to the decrease in crystal symmetry; hence, due to the small crystallite size, XRD peak broadening did not allow for the discrimination between cubic and tetragonal phases of $BaTiO_3$ NPs. However, the cubic structure is only stable above the Curie

temperature of $BaTiO_3$ (T = 133°C) and is not piezoelectric, while the synthetized $BaTiO_3$ NPs have shown good piezoelectric response at room temperature, suggesting the presence of mainly tetragonal structures [174].

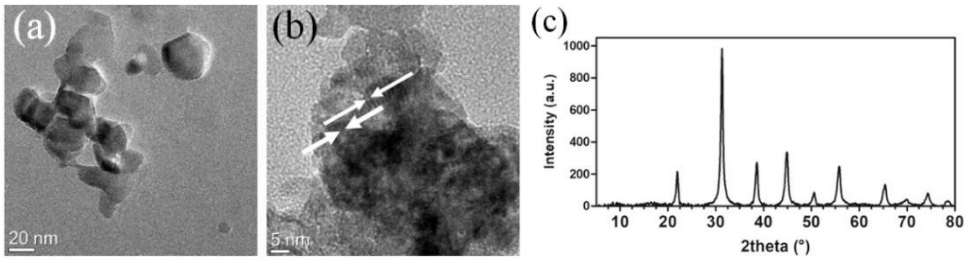

Figure 5.2: TEM images of $BaTiO_3$-HCA NPs. (a) Small globular particles (30-50 nm) grouped in bigger assemblies of 150-200 nm. (b) Detail revealing the $BaTiO_3$ crystal planes (indicated by arrows). (d) XRD pattern of $BaTiO_3$ NPs powder. X-ray source: Cu(Kα).

2theta (°)	d spacing (Å)	Relative Intensity (experimental)	Relative Intensity (tetragonal) [175]	Relative Intensity (cubic) [175]
22.26	3,994	206.4	209.3	206.6
31.61	2,831	1000	1064.9	1057.1
38.89	2,316	265.7	263.2	259.4
45.17	2,007	342.8	345.2	344.7
50.85	1,796	78.2	88	95.9
51.17	1,785	/	10.7	
56.1	1,639	244.2	278.6	356.4
56.4	1,631	/	79.5	
65.72	1,421	138.3	118	118.5
66.03	1,415	/	39.2	59.3
66.19	1,412	/	19.8	
74.67	1,271	79.6	69.5	89.7

Table 5.1: Experimental XRD reflections with the corresponding reference parameters for cubic and tetragonal BaTiO3.

Average crystallite size has been estimated as 20.2 nm by applying the Scherrer equation on the most intense and resolved peaks:

$$D = \frac{k \cdot \lambda}{\beta \cos\theta}$$

where D is the mean size of crystallites (nm), k is crystallite shape factor (a good approximation is 0.9), λ is the X-ray wavelength, β is the full width at half maximum

(FWHM) in radians of the X-ray diffraction peak and θ is the diffraction angle [176]. A k value of 0.94 has been chosen as it usually applies for quasi-spherical particles. This result totally agrees with TEM images, which show bigger particles but crystalline domains around 20 nm.

5.1.3 Lipophilic functionalization: BaTiO3-DDA

The $BaTiO_3$ NPs synthetized as described in the previous section showed poor dispersion properties in solvents, mostly due to aggregation induced by surface instabilities. Hence, the surface of the nanoparticles was coated with DDA, by exploiting the catechol functionality of the ligand.

DDA synthesis In a 500 mL round-bottomed flask equipped with a magnetic stirrer and under nitrogen flow, 2.49 g (13.2 mmol) of dopamine hydrochloride were dispersed in 100 mL of dry THF, then 4.5 mL of triethylamine (32.3 mmol) were added. The solution was cooled to 0°C with an ice bath and a solution of lauryl chloride (3.00 mL, 13.0 mmol) in 150 mL of dry THF was added dropwise in 3 hours. After complete addition of the acyl chloride, the mixture was stirred at room temperature for 45 minutes then 25 mL of water were added, the organic solvent was removed by rotary evaporation and the aqueous phase was extracted 3 times with ethyl acetate. The organic phase was then dried over dry Na_2SO_4 and concentrated under reduced pressure to afford DDA as a white solid (Figure 5.3). Yield = 85%. The product underwent NMR and ESI-MS analysis to assess purity and to confirm the structure (see Figure 5.3).

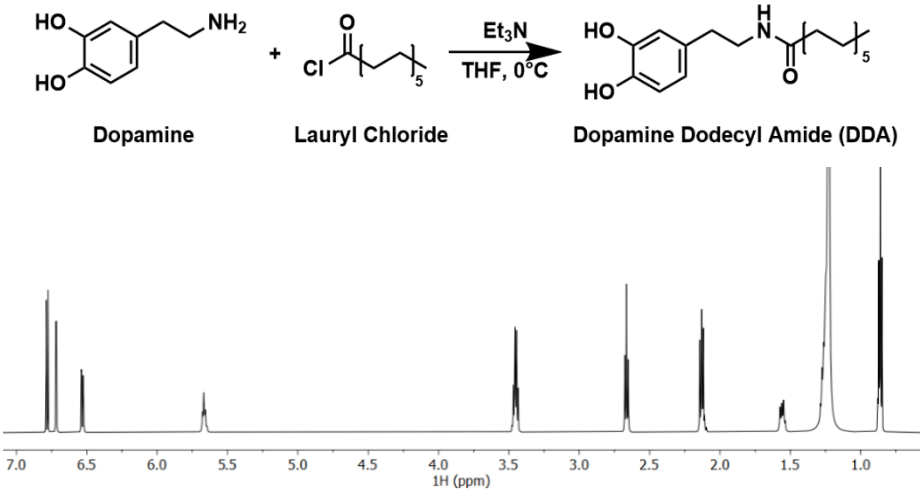

Figure 5.3: Reaction scheme for the synthesis of the lipophilic DDA ligand 1H-NMR spectrum of the ligand.

The reactive surface of $BaTiO_3$ NPs has been covered with dopamine dodecylamide (DDA) by exploiting the catechol functionality of the ligand. In a 250 mL beaker, 0.577 g of $BaTiO_3$ NPs have been redispersed in 50 mL of absolute ethanol. In order to ensure complete disaggregation of the NPs, the suspension has been treated with tip-probe sonicator (70% amplitude) for 1 min. Then, 1.15 g of DDA have been added to the suspension, which has been further ultrasonicated for another 1 min. Hence, the mixture has been then placed in a 100 mL round-bottomed flask and stirred at 60°C overnight to ensure the ligand exchange.

Purification of the final mixture was performed by repeated centrifugation (15 min at 6000 rpm) and wash with ethanol two times then with hexane until colourless supernatant was obtained. Finally, the obtained $BaTiO_3$-DDA NPs have been collected in 5 mL of hexane, leading to a uniform brown suspension of NPs.

The solution was drop casted a perforated carbon film supported by a copper grid. The preparation was then dried at 100 °C. The Transmission Electron analyses were performed with a FEI TECNAI F20 microscope operating at 200 keV. The instrument was also equipped with a dispersion micro-analysis of energy (EDS) and the STEM accessory. The TEM image were taken in the phase contrast mode and Selected Area electron diffraction (SAED). STEM pictures were recorded using an High Angle Annular Dark Field (HAADF) detectors: in this imaging mode the intensity I is proportional to $Z^{1.7}t$, where Z is the mean atomic number and t is the thickness of the specimen

The crystal structure of the prepared $BaTiO_3$ nanopowder was assessed by powder XRD giving identical results to the ones already reported in the previous section for $BaTiO_3$-HCA. Similarly to that case, the XRD peak broadening due to the small crystallite size of the nanopowder did not allow for the assessment of the tetragonal crystal phase of $BaTiO_3$ nanoparticles.

After ligand exchange reaction (Figure 5.4b) the $BaTiO_3$-DDA nanosystem showed good dispersibility and colloidal stability in organic solvents such as hexane, chloroform and THF, revealing the effectiveness of the surface modification with the synthetic catechol ligand.

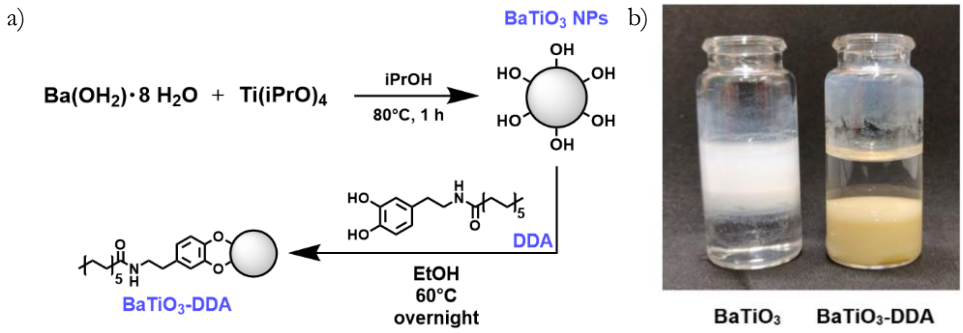

Figure 5.4: a) Reaction scheme for the of lipophilic barium titanate nanoparticles by coating with dopamine dodecyl amide (DDA). b) Optical camera picture demonstrating the efficient stabilization of BaTiO3-DDA nanoparticles in chloroform. While pristine BaTiO3 nanoparticles (left) are efficiently dispersed in the upper aqueous phase and do not diffuse into the lower organic layer, lipophilic BaTiO3-DDA nanoparticles show better dispersibility and inverse solubility properties.

The obtained nanosystem was therefore deeply studied by TEM analysis which first revealed the presence of crystallites having a size between 20 and 50 nm (Figure 5.5). The organic coating was also visible from TEM images as a thin layer that wraps the surface of the entire nanoparticles.

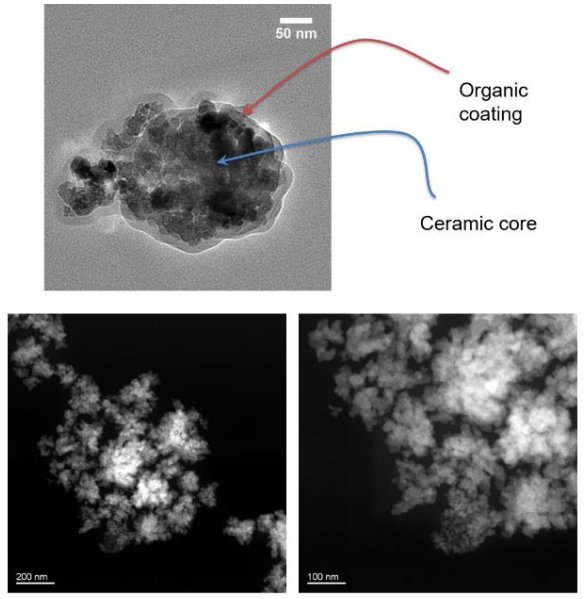

Figure 5.5: TEM (top) and STEM (bottom) images of the prepared $BaTiO_3$-DDA. The organic coating is visible in TEM mode as casing the ceramic cores.

Moreover, selected-area electron diffraction (SAED) analysis was performed over a 200 nm^2 area of the sample, revealing some crystal plane reflections (Figure 5.6). Then, by software manipulation of the SAED pattern, it was possible to extract a pseudo-diffraction spectrum where the *x*-axis is attributed to the reciprocal of the distance between crystal planes. The contribution from the amorphous organic coating can be assigned to the diffuse light from the centre of the SAED pattern while the clear spots represent well-distinct crystal plane reflections. At this point, the position and relative intensities of the SAED diffraction peaks were extracted from the pseudo-diffractogram and compared to the literature values for tetragonal $BaTiO_3$ reflections, giving a good degree of match between the two. As well as for XRD analysis, the small crystallite size did not allow for the analytical determination of the degree of tetragonality of the prepared nanopowder. However, the piezoelectric properties that will be shown next reveal good piezoelectric response (and thus high tetragonality) of the nanopowder.

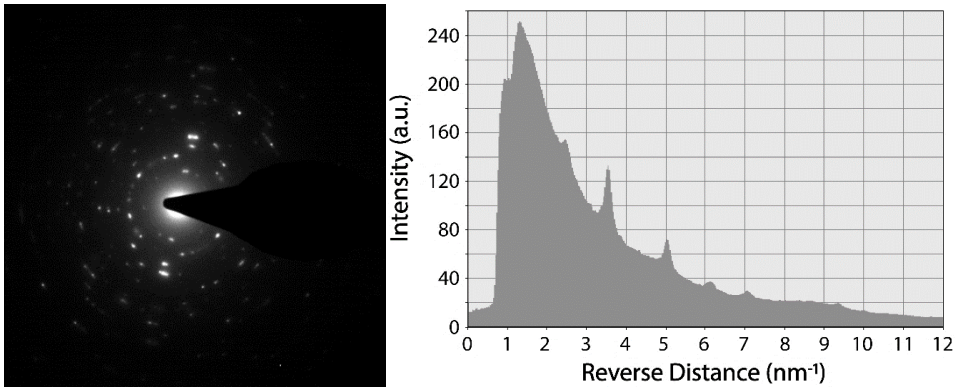

Figure 5.6: TEM analysis. Left: selected-area electron diffraction (SAED) pattern of a crystalline $BaTiO_3$ nanoparticle. Right: integrated spectrum revealing main diffraction peaks obtained by the SAED analysis.

Finally, the elementary chemical composition of the nanopowder was assessed by energy-dispersive x-ray spectroscopy (EDX) (Figure 5.7). The irradiation of the sample by high-energy electron cause for the formation of inner electron vacancies in the specimen atoms, which then relax emitting characteristic x-ray lines that can be unambiguously attributed to the element that generated them. The Ba and O peaks are displayed. The Ti K-peak is superimposed on the Ba L-lines, but it is possible to confirm the presence of titanium by observing the presence of the Ti L-line to the left of the oxygen peak, just above the background. The Cu characteristic line are due to the support grid.

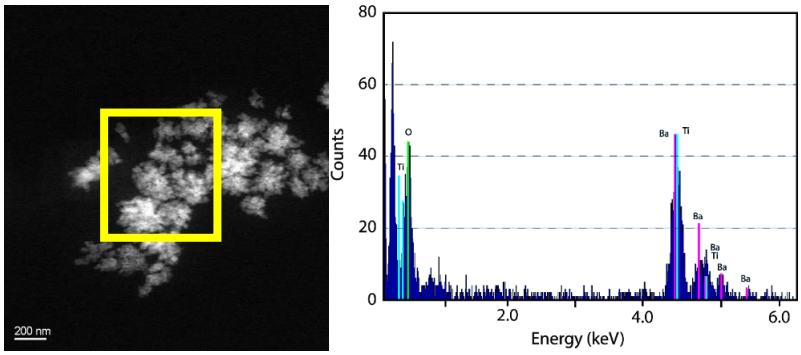

Figure 5.7: Energy-dispersive x-ray spectroscopy (EDX) of the region highlighted by the yellow box in the upper STEM image. Tabulated spectral lines for barium (pink), titanium (blue) and oxygen (green) are reported for comparison.

5.2 PIEZOELECTRIC/PIEZOIONIC: IONOGEL/BATIO3

The hydrophilic nanoparticles were employed in a nanocomposite based on a chemically cross-linked gel incorporating a highly conductive ionic liquid. This system was engineered to respond to mechanical stimulations by combining piezoionic and piezoelectric activity, generating electric charge due to a redistribution of the mobile ions across the polymer matrix and to the presence of the electrically polarized ceramic nanoparticles, respectively.

5.2.1 Nanocomposite Fabrication

The ionogel/$BaTiO_3$ nanocomposite (IG/BAT-Nc) was fabricated using a one-pot synthesis approach, by means of a free-radical UV photo-crosslinking reaction and a simple molding process. The photo-polymerization process is cost-effective and enables to print polymeric nanocomposite layers (1mm thick) in a simple, controllable, and reproducible fashion, with potential for future implementations in UV-assisted 3D printing technologies (e.g. digital light projection-based stereolithograpy [177]). The polymeric matrix was composed by polyvinylpyrolidone (PVP, 40000 Mw), physically intertwined with a chemically cross-linked polymer network, constituted by a random copolymer of highly hydrophilic (hydroxyethyl)methacrylate (HEMA) and acrylonitrile (AN), namely poly-HEMA-co-AN. PVP was introduced as a toughening agent for the ionogel, reinforcing the poly(HEMA-co-AN) matrix through the formation of an interpenetrating network (IPN) between the two polymers. The relative ratio of the compounds was set as PVP : HEMA : AN = 1 : 12.7 : 8.3 wt. After addition of the ionic liquid and $BaTiO_3$ NPs, in order to trigger the cross-linking reaction the photoinitiator solution (ethylene glycol dimethacrylate, EGDMA, 5.5% wt with respect to the PVP and acrylic monomers weight) was added to the mixture. This network structure was engineered to allow the polymer to retain a large amount of suitable ionic liquids and to incorporate hydrophilic piezoelectric nanostructures, responsible for the piezoionic and piezoelectric effect respectively. As ionic liquid 1-(2-hydroxyethyl)-3-methylimidazolium tetrafluoroborate (HoEMIMBF_4, uptake equal to 45% wt) was used, due to its good solubility in water, affinity with hydrophilic compounds and high ionic conductivity[178]. A water suspension of custom-synthesized $BaTiO_3$-HCA nanoparticles ($BaTiO_3$-HCA NPs, 2.5% wt with respect to the total polymer mass) was also added (see Section 5.1.2 for details of $BaTiO_3$-HCA NPs). The pre-polymer was then poured into a simple molding constituted by two glass slides and a silicone spacer (1mm thick). The radical polymerization process was then activated by means of UV light, generated by a Blackray B100-AP lamp (100W, 0.15 W/cm^2).

The exposure time was set to 45 minutes. After the cross-linking, the polymeric film was demolded and dried in vacuum overnight to remove water residuals. The optimal formulation and synthesis procedure were determined empirically, by qualitatively evaluating the uniaxial stretching of the material. All reagents were purchased from Sigma Aldrich, except the ionic liquid that was purchased from Io-Li-Tec. After demolding, the polymeric film was dried in vacuum overnight to remove water residuals. A detailed analysis of the materials water uptake properties is reported in next section (5.2.2).

The optimal formulation and synthesis procedure were determined empirically, by qualitatively evaluating the uniaxial stretching of the material. The soft nanocomposites exhibited elastomeric-like properties, which are beneficial to enhance their electromechanical response under low frequency stimulations in the quasi-static regime [179].

After samples preparation, the nanocomposites were poled at room temperature under an electric field of 3.3kV/cm for 7 hours in vacuum (10^{-5} torr) by clamping the materials between a pair of anticorodal aluminum slabs. The choice of these relatively mild polarization conditions was due to the low tolerance of the ionogel matrix to high intensity electric fields and harsh temperature conditions, which may induce the polymer backbone degradation [180]. At the same time, it should be feasible to obtain an adequate polarization of the piezoelectric material with lower coercive fields thanks to the presence of the ionic liquid, as previously demonstrated by Fukagawa et al. [181].

A schematic of the obtained poled piezoionic/piezoelectric nanocomposite is reported in Figure 5.8 along with a photograph of a typical sample. In Figure 5.9 are reported SEM pictures.

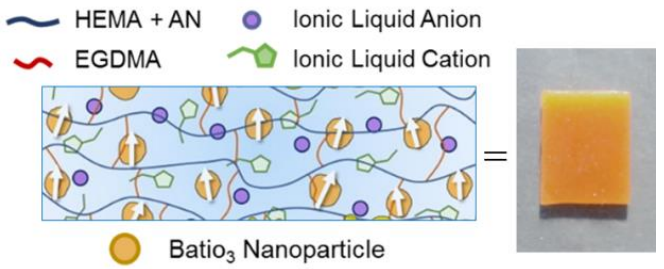

Figure 5.8: Schematic representation of the poled IG/BAT-Nc (white arrows indicate the nanoparticles electrical dipoles) and picture of a typical sample.

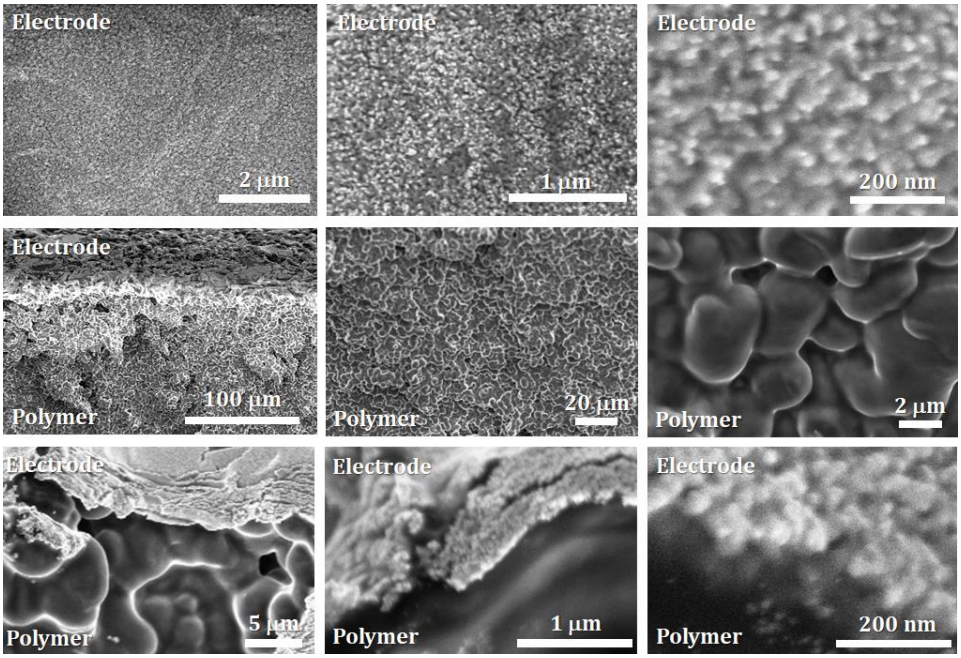

Figure 5.9: Schematic SEM imaging of the ionogel/$BaTiO_3$ nanocomposite provided with nanostructures gold electrodes produced by mean of SCBD. A top view of the electrode is reported on top, while a cross-section of the material, highlighting the morphology of the ionogel/$BaTiO_3$ nanocomposite, is shown at the middle row of the panel. Details of the electrode morphology in the cross-sectional view are reported at the bottom. SEM imaging was conducted at the Politecnico of Milan by the facilities of the group of Prof. Carlo Casari, who is greatly acknowledged. The scanning electron microscope used was a Zeiss Supra 40.

5.2.2 Water uptake characterization

A quantitative characterization of the water-absorbance properties over time for both the bare ionogel (IG) and the ionogel/$BaTiO_3$ (IG/BAT) nanocomposite was performed. Samples of both materials (surface area 20 mm x 10 mm, 1 mm thick and 25 mm x 15 mm, 1 mm thick) were weighed straight after synthesis, after drying overnight and after exposure of the specimen at laboratory ambient conditions (20 °C, 45% RH), every half an hour for 2.5 hours, then after 5 hours and 12 hours. In the relaxed state after synthesis the IG and IG/BAT weights were equal to 0.4167g and 0.5927g, respectively. The differential weight, expressing the water amount absorbed by the materials at different times, was calculated as $W_{diff} = (W_A - W_D)/W_A$, with W_D being the weight of the materials after drying and W_A the weight of the materials at ambient conditions. The water uptake of both the IG and

IG/BAT nanocomposite showed to be low, with W_{diff} ranging from 0.2 % wt up to 1.2 %wt. This quite poor moisture sensitivity could be probably due to an interplay of factors, such as the cross-linking degree of the poly(HEMA-co-AN) network and the high rate of the conversion reaction prompt by the amount of radical initiator employed, as well as from the specific fabrication conditions. The measured weights for the IG/BAT samples (S1 and S2) are presented in Table 5.2, along with a graph showing the material W_{diff} evolution over time (Figure 5.10).

$Time\ (h)$	$W_{diff-S1}(\%)$	$W_{A-S2}(\%)$	$W_{diff-S1}(\%)$	$W_{diff-S2}(\%)$	$error\ (\%)$
0.0	0.2287	0.3252	0.00	0.00	
0.5	0.2288	0.3256	0.04	0.12	0.2
1.5	0.2291	0.3260	0.17	0.25	0.2
2.5	0.2294	0.3263	0.31	0.34	0.2
5.0	0.2298	0.3272	0.48	0.61	0.2
12.0	0.2309	0.3292	0.95	1.22	0.2

Table 5.2: Weight of the IG/BAT nanocomposites after drying (W_D) and at ambient conditions (W_A) measured over time. The error, calculated propagating the microbalance instrumental error, is also reported.

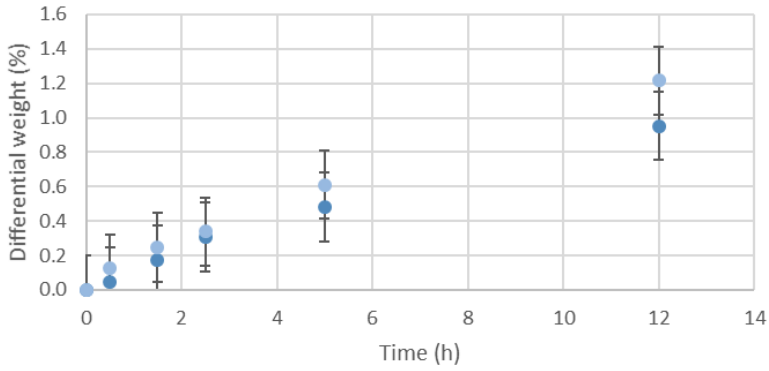

Figure 5.10: Water uptake curve expressed in terms of W_{Diff} over time for the IG/BAT S1 and S2 samples.

5.2.3 Electro-mechanical testing

The response to mechanical stimuli of both the pristine ionogel and the poled IG/BAT-Nc samples was assessed through open-circuit voltage measurements under a low intensity periodical driving force, at low frequencies. A quasi-static method was used, employing an earlier version of the custom-designed measurement apparatus presented in Section 3 (see Figure 3.3a for reference). In order to apply an oscillating component to the applied force, an electro-dynamical exciter controlled by a function generator was used as the mechanical actuator. The compressive load was measured by a digital dynamometer (Sauter FH50) mounted onto a micrometric translator and provided with a planar copper-based metallic electrode (surface area was 1cm x 1cm), operating as a charge collector. A second electrode was glued to the actuator, operating as the counter-charge collector. All measurements were performed with a static load of 0.5N to guarantee electrical contact between the samples and electrodes, and a periodic force of 0.5N. Voltage and force data were acquired in real time at a sampling frequency of 300Hz with a dedicated LabView program. The output voltage generated by the material was recorded using a digital multimeter (Agilent 34410A) connected to the electrodes.

Both ionogel and IG/BAT-Nc were tested for comparison at the frequencies of 100mHz, 500mHz and 1Hz. In order to verify the isotropy or anisotropy of the materials response, all groups of measurements were performed twice, by flipping the samples orientation with respect to the direction of the normal force, as schematized in Figure 5.11.

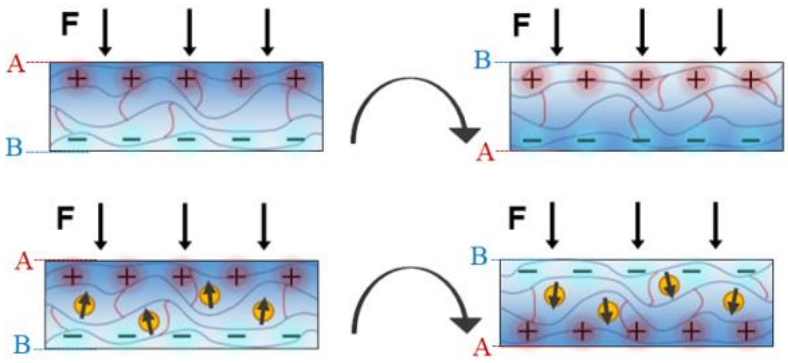

Figure 5.11: Isotropic piezoionic response of a pristine ionogel (top) and anisotropic piezoionic/piezoelectric response of a poled IG/BAT-Nc (bottom). Dark gray arrows indicate the nanoparticles electrical dipoles.

The electromechanical stability of the materials was assessed through cyclic measurements using the same experimental apparatus. The samples showed a good signal stability for over 20000 cycles (more than 15 hours of operation), preserving their responsive behavior for several months after fabrication.

5.2.4 Results

Both the pristine ionogel and IG/BAT-Nc responded to low frequencies, with no frequency-dependent output voltage in the range explored (Figure 5.12).

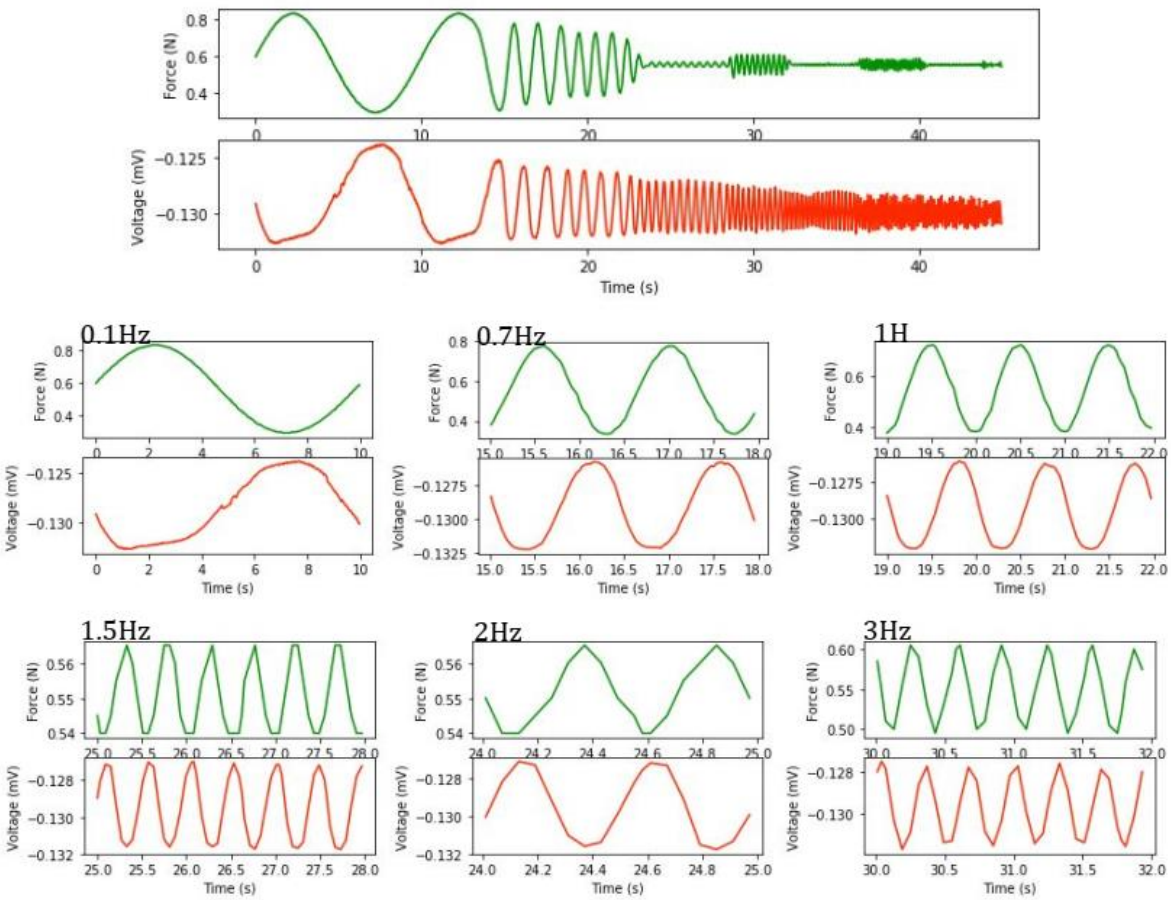

Figure 5.12: Ionogel/BaTiO3 nanocomposite response at stimulation frequencies ranging from 0.1Hz to 6Hz (top). The working mechanism and sampling frequency of the dynamometer used did not allow to measure the force over 1Hz. However, even at higher frequencies the response does not seem to weaken for increasing frequencies (bottom plots).

The electrical response was, for both sample types, out of phase with the mechanical stimulation, with a constant lag time corresponding to 180ms (Figure 5.13). This delay could be ascribed to an interplay between a material intrinsic property (i.e. the mechanical relaxation and ionic transport dynamics) and an instrumental error deriving from the data acquisition and communication rates between the multimeter and load cell.

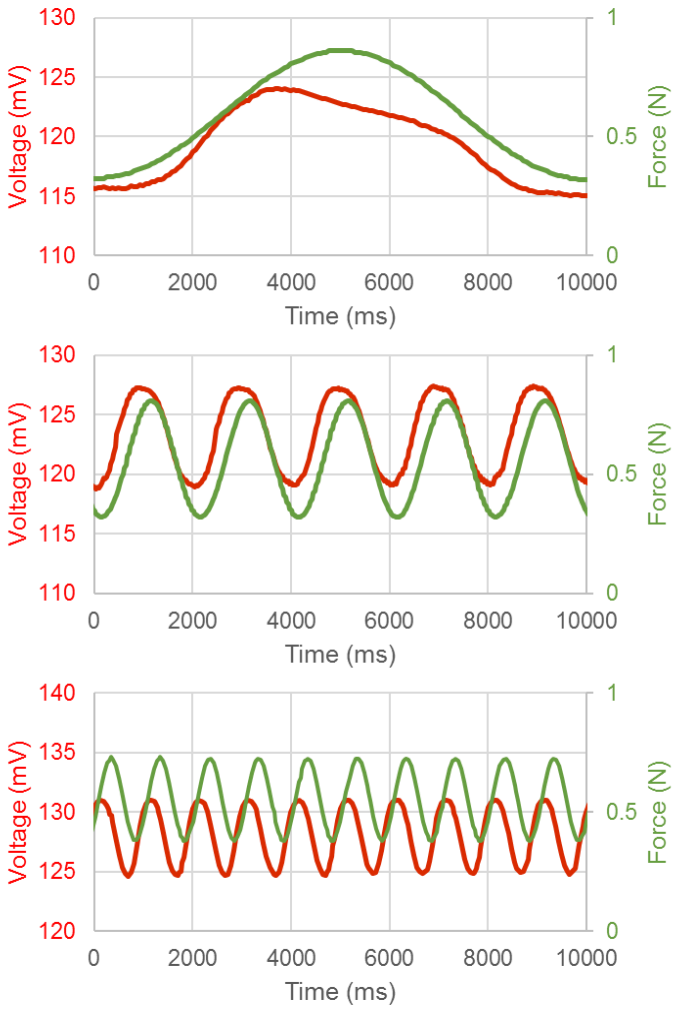

Figure 5.13: IG/BAT-Nc response at 0.1Hz (top), 0.5Hz (middle) and 1Hz (bottom).

As shown by the graphs (Figure 5.13) the presence of the poled nanoparticles enhanced the electromechanical performance of the material, allowing to reach a response of 8mV under a compressive force of 0.5N, corresponding to a pressure

of 5kPa. This value falls into the low-pressure range (< 10kPa, 1kPa being roughly the sensitivity of the human finger) as identified in the touch sensors framework [182] and it is adequate to monitor a variety of bio-mechanical motions, such as blood pressure changes between heartbeats [183]. Moreover, the poled sample showed a typical ferroelectric hysteresis [184], not shown by the piezoionic gel (Figure 5.14).

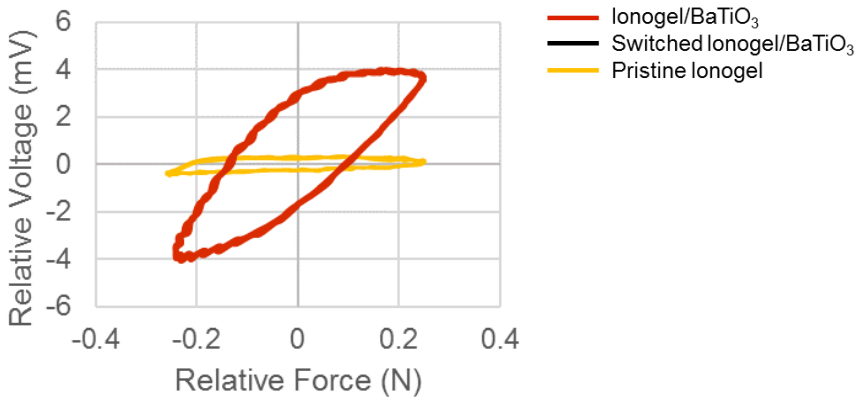

Figure 5.14: Hysteresis loop of pristine ionogel and IG/BAT-Nc, the latter showing the typical ferroelectric behavior.

The maximum output values reached by the nanocomposites were systematically higher with respect to that of the pristine ionogel for all of the frequency tested when the direction of the applied compressive force was the same as the electrical polarization of the nanoparticles (8mV to 7mV against 3.5mV to 1mV for 0.1Hz and 1Hz, respectively). This effect was damped down when the pre-load was applied in the opposite direction and no significant difference in the response between the samples was observed (3mV to 1mV for 0.1Hz and 1Hz, respectively). This anisotropic response can be ascribed to presence of the $BaTiO_3$ NPs, which confer to the ionogel the bias directionality typical of ferroelectric materials. This behavior was probably due to a cooperation between two mechanisms: the isotropic piezoionic effect and the anisotropic ferroelectric effect. While the pristine ionogel response remained almost unvaried in both amplitude and phase under sample switching (Figure 5.15b), the IG/BAT-Nc response exhibited both an anisotropic behavior (phase inversion) and an amplitude modulation (Figure 5.15b). The piezoionic and piezoelectric contributions showed the same phase in one configuration (the directions of pre-load and polarization are parallel), and an opposite phase when the sample was flipped with respect to the applied force (the

directions of pre-load and polarization are antiparallel), causing the observed amplitude modulation.

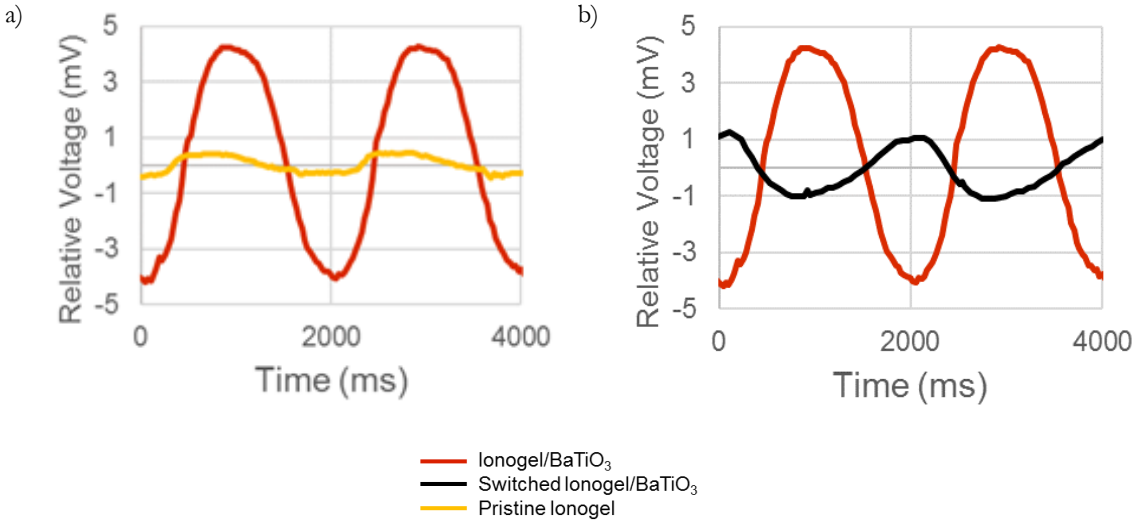

Figure 5.15: (a) Pristine ionogel and ionogel/BaTiO3 nanocomposite response at 0.5 Hz. (b) Anisotropic response of the ionogel/BaTiO3 nanocomposite at 0.5 Hz, observed by flipping the sample with respect to the normal force direction.

This remarkable feature is particularly interesting for applications in discriminative touch sensing and objects localization in physically unstructured environments [19,185–187]. In fact, ionic gels and ionogel-based materials are isotropic systems that allow to identify only the direction of the applied force by measuring the generated bias, despite the sample orientation [94,150,151]. On the other hand, the nanocomposite developed in the present work enables to discriminate the sensing element orientation with respect to the applied force, exploiting the anisotropy induced by the combination of the piezoionic and piezoelectric effect.

The characteristics of fatigue under cyclic stress are influenced by both polymer internal structure (as degree of cross-linking, molecular weight, water and ionic liquid content, filler fraction) and external stimuli, as well as by stress intensity, frequency, and temperature [190]. Stress frequency and intensity are of particular importance since polymers usually show viscoelastic behavior [190]. In Figure 5.16 is reported a graph showing the relationship between the electromechanical transduction performance (output voltage over stimulation force) and number of cycles for the last 6000 cycles of the durability tests. The decay in the material performance followed a logarithmic function, which is typical of polymeric materials

in which crack initiation is faster than crack growth [191]. Nevertheless, the material response was not entirely compromised along the last 6000 cycles, giving an output voltage of about the 7% with respect to the first cycles, but without exhibiting micro-cracking or observable physical damage over time.

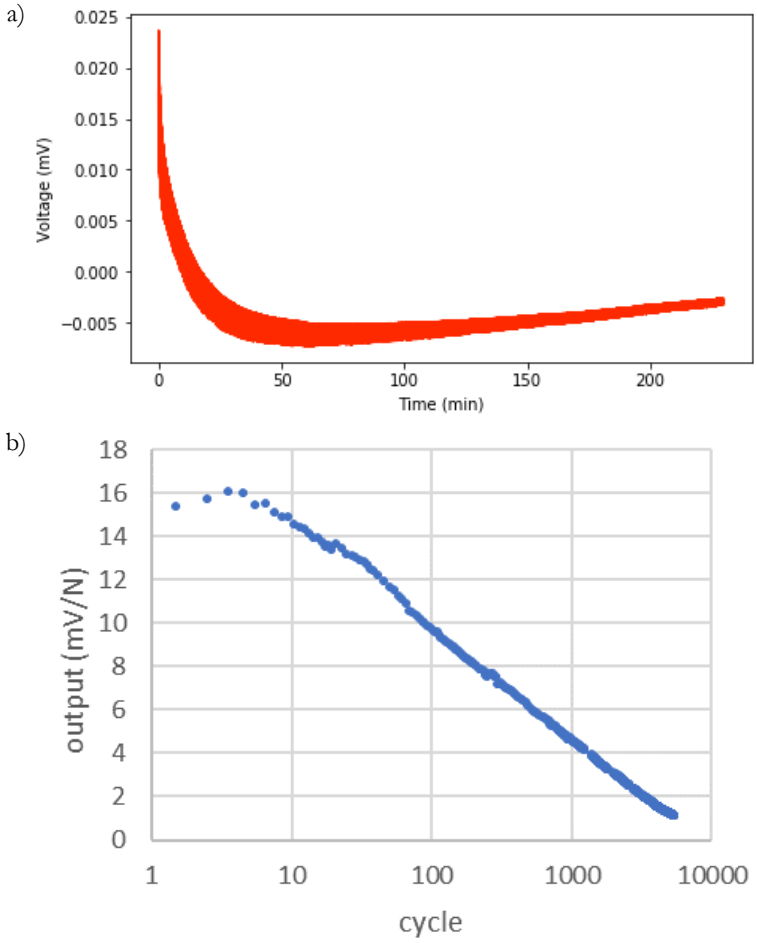

Figure 5.16: a) Single measurement of the last 6000 cycles of life. The measure was performed with a cyclical force of 0.522N at 0.4Hz. b) The output voltage decreases as the logarithm of the number of fatigue cycles.

5.2.5 Conclusions

In conclusion, the fabrication and electro-mechanical characterization of a novel piezoionic/piezoelectric polymeric nanocomposite material based on a chemically cross-linked ionogel with embedded barium titanate ($BaTiO_3$) ferroelectric nanoparticles was demonstrated. The composite responded to low frequency (0.1

Hz to 1 Hz) mechanical compressive stresses in the low-pressure regime (< 10 kPa) generating output voltages up to 8 mV. The combination of the piezoionic and piezoelectric activity resulted in an anisotropic electrical response to quasi-static mechanical perturbations, enabling to discriminate the sample orientation with respect to the load direction by monitoring the phase and amplitude modulation of the output signal.

The results suggest that the presented piezoionic/piezoelectric nanocomposites constitute an interesting solution for the development of smart devices for discriminative touch sensing and objects localization in physically unstructured environments for soft robotics and wearable electronics applications.

5.3 PIEZOELECTRIC: PDMS/$BaTiO_3$

The lipophilic nanoparticles were employed in a nanocomposite based on polydimethylsiloxane (PDMS). This material is one of the most used polymeric matrixes to embed piezoelectric particles is a silicone-based organic polymer; it is particularly convenient for several applications because it is hydrophobic, permeable to gases, physiologically inert and thermally stable. Moreover, it has good mechanical properties, such as high stretchability and deformability, it is optically transparent and a good dielectric [192]. Those characteristics make it suitable for a wide range of applications. PDMS' mechanical properties (e.g. stiffness) can be tuned during the fabrication process, and its piezoelectric properties are determined by the loading of piezoelectric particles and the poling process. For all of these characteristics PDMS has been widely used for piezoelectric nanocomposites development [193].

5.3.1 Nanocomposite fabrication

In order to achieve a uniform distribution of $BaTiO_3$-DDA nanoparticles inside the PDMS matrix, a common organic solvent was used to dissolve the elastomer base and to disperse the nanoparticles, and the two solutions were mechanically stirred together. After the complete evaporation of the solvent, when the nanoparticles were well dispersed in the PDMS base, the curing agent was added and mechanically stirred with the PDMS-nanoparticle dispersion (elastomer : curing agent = 10 : 1 w/w) [194].

The fabrication procedure followed is reported here. The silicone elastomer base was dissolved in chloroform, and the solution was mechanically stirred for 30 minutes (elastomer : chloroform = 2 : 5 v/v). Meanwhile, the chosen quantity of nanoparticles to be integrated into the nanocomposite was dispersed in chloroform. The mixture is mechanically stirred for 30 minutes. The two solutions of elastomer and nanoparticles were mixed together and stirred for 20 minutes with a magnetic anchor. The solution was then heated at 60°C in order to speed up the solvent evaporation process. The complete evaporation of chloroform leaves the $BaTiO_3$-DDA nanoparticles dispersed in the polymer base lasted about 1.5 hours. The curing agent was subsequently added, and the mixture was mechanically stirred for other 20 minutes. After stirring, the obtained mixture was degassed and poured into a prepared mould for nanocomposite casting. The mould consisted of an aluminium component, provided with a 0.5 mm deep recess produced by milling, in which the prepolymer solution was poured. After pouring the solution into the mould, it was

degassed in a vacuum chamber in order to eliminate air bubbles trapped in the mixture during the previous phases and other bubbles originated after casting. A second aluminium component serving as a lid for the mould was fastened on top of the bottom aluminium part to ensure a tight sealing of the casted solution. The nanocomposite material was cured at 150°C for 2,5 hours in a pre-heated oven. After curing, a 60mm x 70 mm, 0.5 mm thick, layer of the material could be easily demoulded from the recess.

The moulded samples were then cut into 16mm-diameter discs using punch-holes (Figure 5.17). In order to characterize the nanocomposite piezoelectric performance at different $BaTiO_3$-DDA concentrations, samples with 0%, 5%, 10%, 15% and 20% w/w nanoparticle loadings (named respectively PP5, PP10, PP15, PP20) were produced. The loading percentage is calculated with respect to the weight of the polymeric part employed. A pristine PDMS sample (PP0) was used as a reference, in order to recognize any additional contributions to the electro-mechanical effect different than the piezoelectric one [195], for example the triboelectric effect [196], electrostriction [197] or dielectric charging [79].

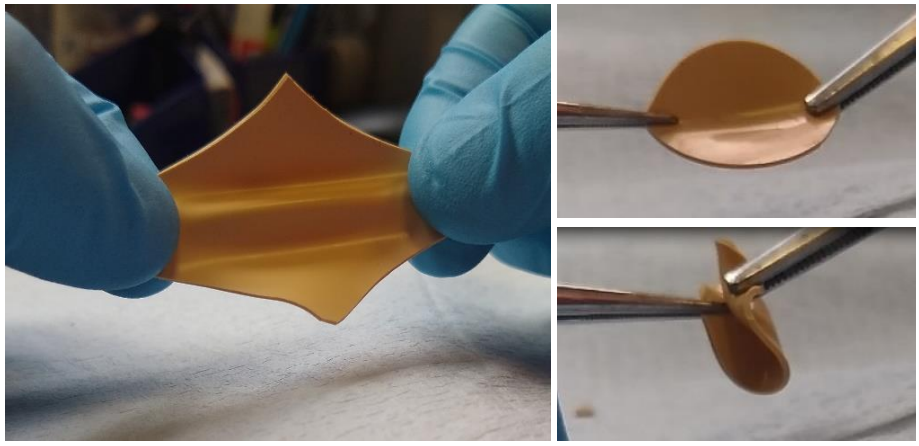

Figure 5.17: Example of a moulded PDMS-$BaTiO_3$ nanocomposite sample. The material resulted in a flexible and stretchable solid, with rubber-like response.

5.3.2 Poling

An optimized poling procedure was implemented in order to align the electrical dipoles within the ferroelectric domains of the nanoparticles and among different nanoparticles, enhancing the piezoelectric effect [145]. In order to efficiently align the dipoles and the ferroelectric domains, a common procedure is to heat the

material over its Curie temperature, and let it cool down under the action of an external electrical field (*field-cooling*).

A schematic representation and some pictures of the setup needed for the poling procedure are shown in Figure 5.18.

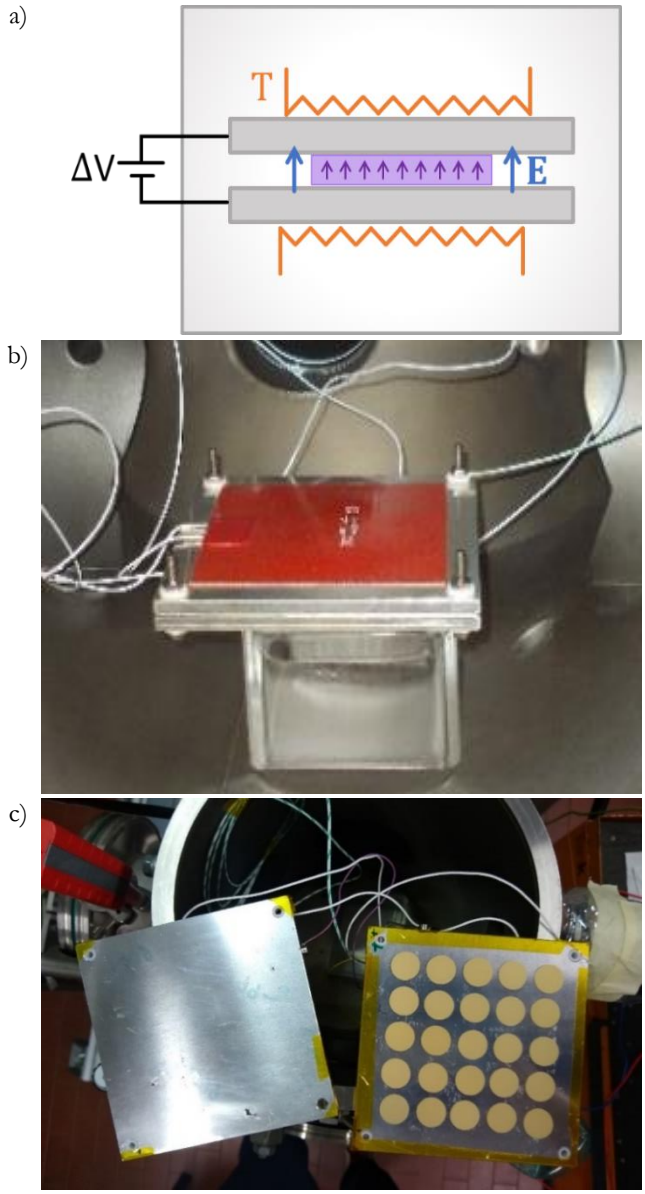

Figure 5.18: Poling schematic representation (a), experimental set-up (b) and a batch of samples before the poling procedure (c).

The nanocomposite samples were placed between two polished aluminium plates, forming a plane capacitor in contact with both sides of the samples, and equipped with input connectors, in order to be charged at the voltage difference needed using a power supply (LKB 3371E). The distance between the plates was adjustable through four screws, and Teflon spacers are used to avoid inducing a short-circuit between the plates. The dimension of the plates and the control on the distance between them were designed to set uniform and known electrical field across the samples. The plates were heated through two silicon heater mats (RS Pro Silicon Heater Mat, 10W) adherent to the metal plates up to 130°C, the temperature was controlled in real time by means of a type-K thermocouple. Once the plates reached the desired temperature, a voltage difference of 1.2kV was imposed between the two plates, generating an electrical field of 20kV/cm. The system was kept in this configuration for 2 hours. After this, the temperature was slowly decreased from 130°C to 110°C, under the imposed electrical field. This first cooling phase took two hours. The heaters were subsequently turned off, and the samples cooled from 110°C to room temperature, still under the effect of the electrical field. The second cooling phase took another 2 hours. In order to prevent ionization discharges in air the whole process was performed inside a vacuum chamber at the pressure of $3 \cdot 10^{-5} bar$. This allowed to condition the ferroelectric phase transition in the desired direction, while orienting the ferromagnetic domains.

5.3.3 Mechanical characterization

In order to quantitatively assess the mechanical behavior of the nanocomposite, mechanical measurements were performed, using a SAUTER Electric Test Stand with an SAUTER F50 dynamometer. The tests were performed on 24mm x 7mm x 0.6mm samples. For each sample 100 cycles of uniaxial tensile tests with a maximum deformation of 75% and a nominal velocity of 10mm/min were performed, in order to obtain the stress–strain curve and the Young's modulus at low strains, and to investigate the mechanical behavior repeatability and any fatigue effects. The last test was conducted up to the mechanical failure of the material, in order to measure the ultimate tensile strength of the nanocomposite material.

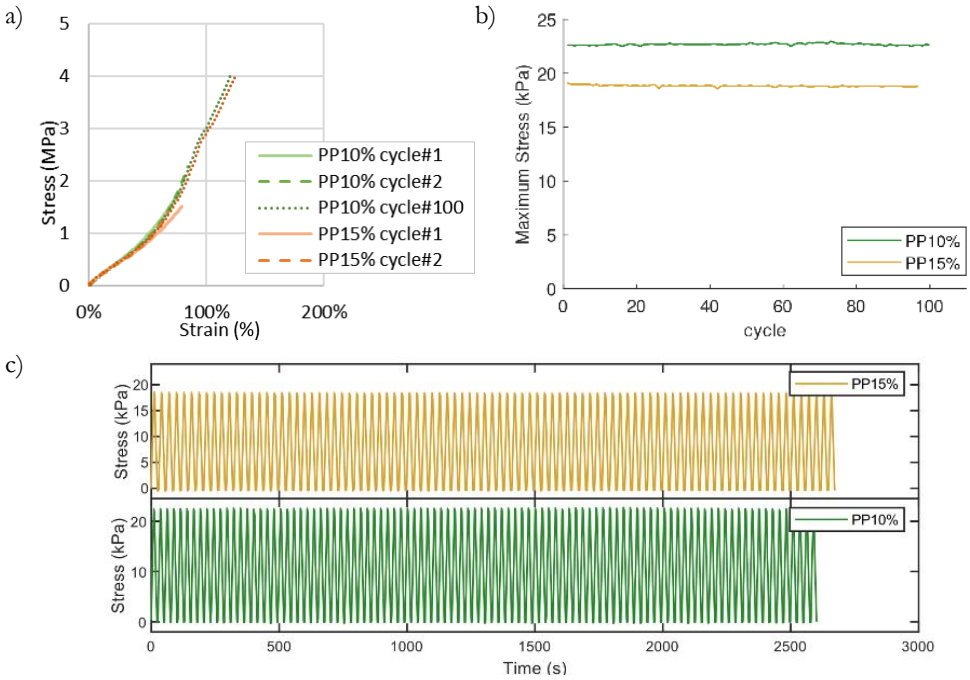

Figure 5.19: a) Stress-Strain measure performed over two different samples of the PDMS/$BaTiO_3$-DDA nanocomposite. The samples exhibit an elastic behaviour with a Young's Modulus of respectively 1.57MPa and 1.70MPa. b) and c) Mechanical stability evaluation through a100-cycle stress-strain measure. The mechanical response of the sample is stable and does not display a fatigue effect.

The mechanical measurements performed on the PDMS/$BaTiO_3$-DDA nanocomposite (Figure 5.19a) confirmed the expected elastic behavior for small strains (<10%) with a Young's modulus of respectively 1.70MPa and 1.57MPa for the 10%wt and 15%wt samples, which is in line with the results commonly obtained for PDMS with a base-curing agent ratio of 1:10 [198]. Compared with pristine PDMS cured at the same temperature, the nanocomposite material has a lower Young's Modulus, which represents the softening of the polymeric matrix caused by the nanoparticles embedded inside it [198]. The measures were highly repeatable, and a 100-cycles deformation measure (Figure 5.19b,c) confirmed the high mechanical stability of the material. The ultimate tensile strain of the material is respectively 121% and 125% for the 10%wt and 15%wt nanocomposite.

5.3.4 Electro-mechanical characterization

In Figure 5.20a and Figure 5.20b are reported the piezoelectric spectra of the different samples in both the orientation configuration. As can be observed in

Figure 5.20 all the measures reported show a peak at 600Hz: as described before this is an instrumental resonance and does not give information about the piezoelectric behavior of the nanocomposites. In order to identify a unique piezoelectric coefficient to investigate its dependence from the nanoparticle loading and the aging or fatigue effect after a long number of cycles an average was performed between the values found at all the frequency, excluding the interval 450-650Hz, which is the frequency interval where most of the electro-mechanical cross-talk and system resonances influence the measures as discussed before.

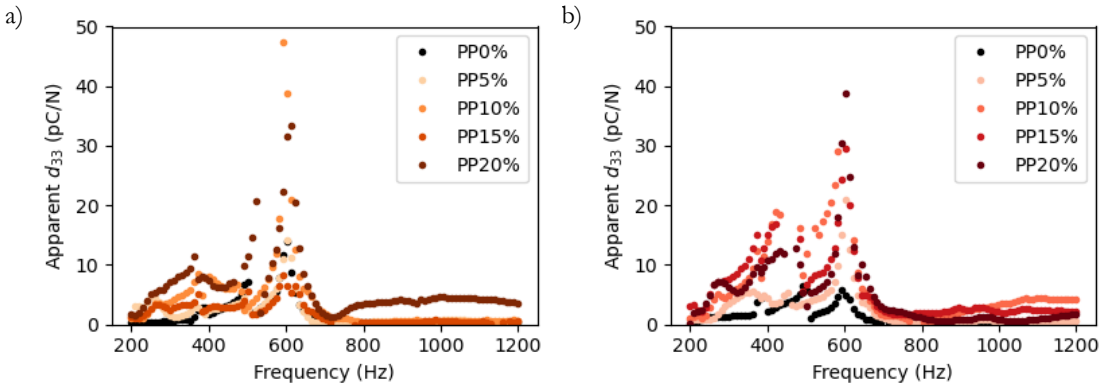

Figure 5.20: Piezoelectric spectra of PDMS-$BaTiO_3$-DDA nanocomposites measured in the two configurations (polarization ↑, in orange, and ↓, in red). The 600Hz peak is an instrumental resonance, it does not give information about the piezoelectric behavior of the nanocomposites.

In order to investigate the long-term stability of the piezoelectric effect in these samples multiple-cycle measurements were performed. In Figure 5.21a is shown a 10-cycle measurement for the same sample (PP15) before and after the poling procedure. As can be observed from the graphs even before the poling procedure the nanocomposite exhibited a piezoelectric behavior, but the effect was not stable, and the piezoelectric coefficient showed a 92% loss between the 1st and the 10th cycle. On the other hand, the poled sample's response was stable over the 10 cycles, displaying a maximum d_{33} variation of ±5%, depending on the tested sample. In Figure 5.21b is represented a 100-cycle measurement over a poled sample. The measurement lasted more than 24 hours of uninterrupted mechanical stimulation. As can be observed in the graph in Figure 5.21b the piezoelectric response was not significantly reduced over this span of time.

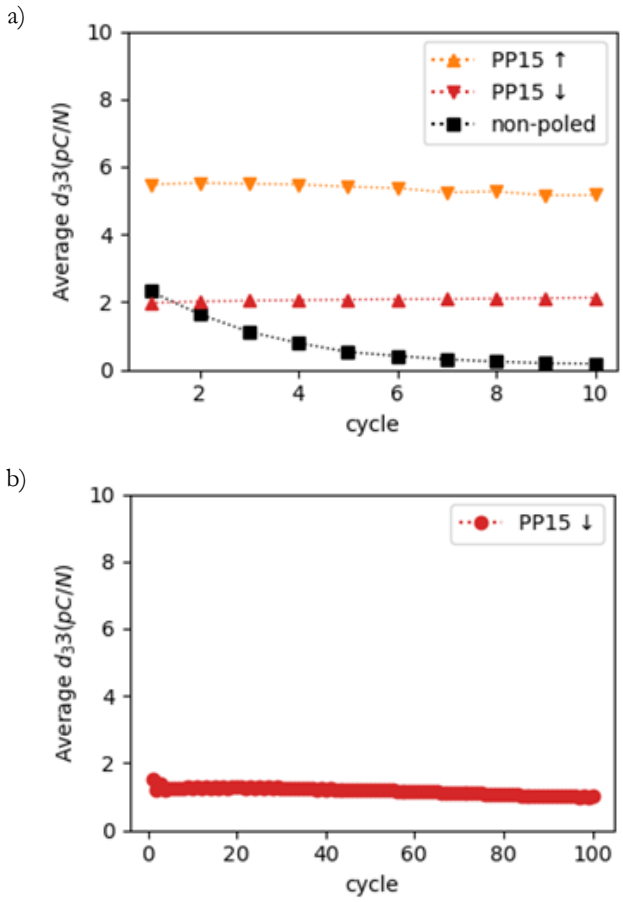

Figure 5.21: a) Performance loss over 10 cycles for the same sample before and after poling. During these cycles there is a 92% loss of the piezoelectric coefficient averaged across the different frequencies (excluding the peak between 400Hz and 700Hz). The measure is compared to an identical one done on the same sample gone through the poling process. b) A 100-cycle measurement over a poled sample. The measurement lasted more than 24 hours of uninterrupted mechanical stimulation. As can be observed in the graph on the right the piezoelectric response was not significantly reduced over this span of time.

In Figure 5.22 and in

Table 5.3 are reported the mean d_{33} values averaged over the whole spectra and at least 3 different measures.

Table 5.3 reports also the averaged d_{33} percentage loss from the first to the fourth cycle as a stability evaluation. As can be observed in Figure 5.22d the piezoelectric

coefficient increased with the nanoparticle loading in one of the two configurations, while it had a different behavior in the other. This could be ascribed to a structural anisotropy, similar to the one found in PVDF, which could be both originated by nanoparticle dispersion inside the polymer matrix and to a non-uniform poling.

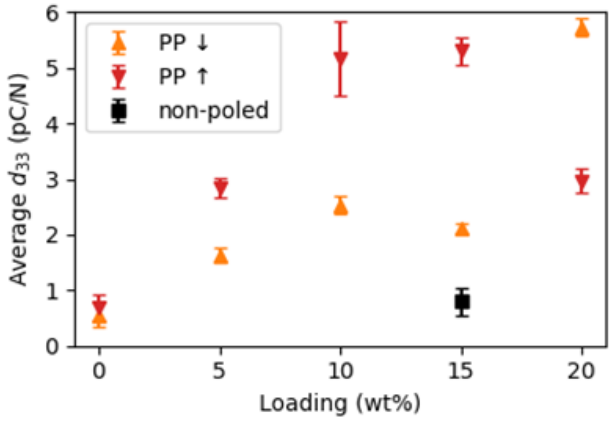

Figure 5.22: Mean d33 values averaged over the whole spectra and at least 3 separate measurements.

Loading	d33 ↑ (pC/N)	d33 ↓ (pC/N)	Stability
0% wt.	0,6	0,7	-80%
5% wt.	2,8	1,6	-20%
10% wt.	2,5	5,2	-1%
15% wt.	2,1	5,3	-2%
20% wt.	3,0	5,7	-1%

Table 5.3: Piezoelectric charge coefficients calculated averaging the piezoelectric response between the different frequencies, excluding the interval 450-650Hz where the response is highly influenced by the system resonances. Stability is represented as the averaged d_{33} percentage loss over 4 cycles.

In order to compare the performance this nanocomposite with the results obtained in literature some open-circuit voltage measurements were conducted using the same experimental set-up and protocol of the previous measures, by connecting the electrodes directly to the Arduino ADC converter, which has an input impedance of 20MΩ. The voltage coefficient spectra for the tested samples can be observed in Figure 5.23. Except for some mechanical resonances similar to the ones found in the charge coefficient, the samples exhibited a piezoelectric linear response between

50 and 200 mV/N depending on the stimuli frequency, with higher responses at lower frequencies (20Hz). The voltage response of the sample was not significantly influenced by the sample loading and is comparable to the ones found in literature for similar nanocomposites [61].

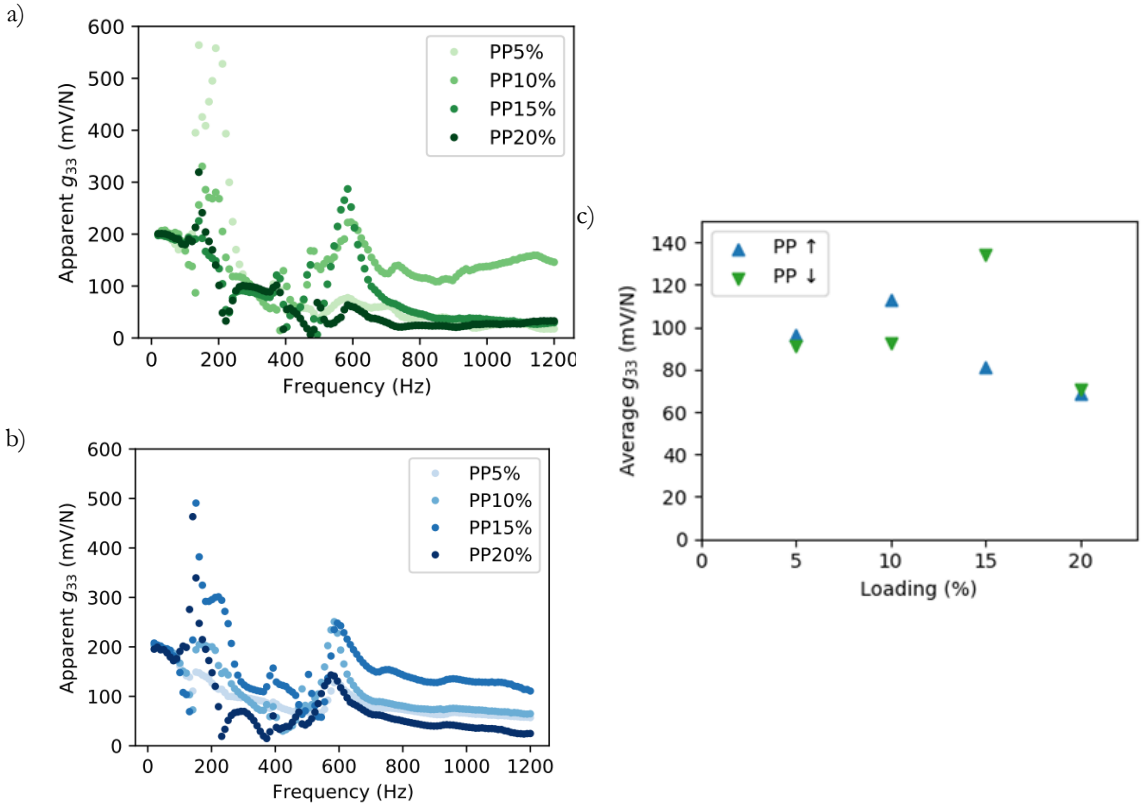

Figure 5.23: a) and b) Open circuit voltage coefficient spectra of PDMS-$BaTiO_3$-DDA nanocomposites, measured in the two configurations (same side facing up, in green, and down, in blue). The 600Hz peak is an instrumental resonance, it does not give information about the piezoelectric behaviour of the nanocomposites. c) Mean g_{33} values averaged over the whole spectra.

5.3.5 Conclusions

A novel piezoelectric PDMS/$BaTiO_3$ nanocomposite was fabricated and characterized. The material architecture is simple, the main novelty of the nanocomposite being the surface functionalization of the nanoparticles to improve their dispersion in the polymeric matrix. Nevertheless, the nanocomposite shows a voltage performance in line with similar nanocomposites in literature, although a comprehensive comparison is not possible due to the lack of reliable and

reproducible measurements in this field, as described in Section 3 and Appendix A. The material, due to its fabrication simplicity and output performance, is therefore a promising base for further developments, for example the implementation of better electrodes, an example of which will described in Section 5.5. The presented nanocomposite was also used to demonstrate the capabilities of the measuring instrument described in Chapter 3.

5.4 PIEZOELECTRIC: 3D PRINTED PIEZO RESINS

Additive manufacturing or three-dimensional printing (3D) is a computer aided production process that enables the creation of 3D pieces directly from digital models depositing the material layer by-layer. Since the advent of polymer-based 3D printing technology, the scientific community has directed great effort towards the development of new polymeric formulations that would allow applying this technique to various fields of application, ranging from materials science to tissue engineering. Among the various techniques that can be employed for the construction of 3D objects, stereolithography (SLA)[199,200] plays a major role, as it allows building structures by selectively photocuring layer-by-layer a well formulated monomeric liquid ink [201].

5.4.1 Nanocomposite fabrication

3D printed discs containing piezoelectric BaTiO3@DDA NPs have been manufactured at the Universidad de Cadiz (Spain) using a XYZ SLA resin as the polymeric matrix. The discs were printed in 16mm-diameter discs 1mm thick, with layer height of 0.1mm. To control the effect of height and layer height, 0.5mm thick discs and 1mm thick discs with 0.025mm layer height were printed as a control. The samples were subsequently UV-cured at 60°C for 1 hour.

In order to characterize the nanocomposites' piezoelectric performance at different $BaTiO_3$-DDA concentrations, samples with 0.5%, 1%, 3%, and 5% w/w nanoparticle loading (named respectively p3D_0.5, p3D_1, p3D_3 p3D_5) were produced. The loading percentage is calculated with respect to the weight of the polymeric part employed. A pristine sample (p3D_0) and a sample without post-curing (p3D_0*) were used as a reference, in order to identify any additional contributions to the electro-mechanical effect different than the piezoelectric one. Samples with poor dispersion (p3D_0,5*, p3D_3,5*) were used as a control for the effect of the nanoparticles' dispersion on the piezoelectric performance of the 3D printed piezoelectric nanocomposite polymer.

The samples were poled accordingly to the poling procedure reported in Section 5.3.2: the nanocomposite samples were placed between two metal plates, forming a plane capacitor in contact with both sides of the samples. The plates were heated at 130-140°C through resistive heaters. Once the plates reached the desired temperature, a voltage difference of (1kV, -1.2kV) was imposed between the two plates, generating an electrical field. The system was kept in this configuration for 2

hours. After this, the temperature was slowly decreased from 140°C to 110°C, under the imposed electrical field. This first cooling phase took three hours. The heaters were subsequently turned off, and the samples cooled from 110°C to room temperature, still under the effect of the electrical field. This second cooling phase took another 2 hours. In order to prevent ionization discharges in air the whole process was performed inside a vacuum chamber at the pressure of $3 \cdot 10^{-5} bar$.

Two different poling procedures were applied, one with a poling field of 10kV/cm imposed for a total of 5 hours and one with -12kV/cm imposed for a total of 7 hours. The poling procedure introduced a directionality in the samples. The samples orientation with respect to their polarization is notated as "↑" for concordant directions and "↓" for opposed direction.

5.4.2 Characterization and Results

The charge measurements were performed with the instrument described in Section 3 between the frequencies of 200-1200Hz with oscillating forces between 0 and 1N applied to the sample. The preload force imposed across the samples was 5N and it was necessary to keep the sample in place and to minimize the triboelectric contributions to the charge collected by the electrodes.

The linearity of the charge response was assessed by force-charge measurement (Figure 5.24). The software imposes force stimuli oscillating at a given frequency with increasing force. If the amplitude of the oscillating charge response is linear with the force amplitude the piezoelectric coefficient can be calculated as the angular coefficient of the force-charge line.

The sample with 0% loading that was not post-cured did not exhibit a significant piezoelectric behaviour (Figure 5.24b). The charges collected by the electrodes are considerably small (of the order of 10^{-14} Coulombs) and the electrical response does not have a significative linearity with the applied force, except for a correlation that can be ascribed to electromechanical noises. The sample with 0% loading (p3D_0) exhibited a linearity between force and charge with a low response for some frequencies, and a non-linear response for others. The samples containing Barium Titanate nanoparticles (p3D_0,5, p3D_1, p3D_3, p3D_5) exhibited a good linearity of the response at all the tested frequencies (one example in Figure 5.24a).

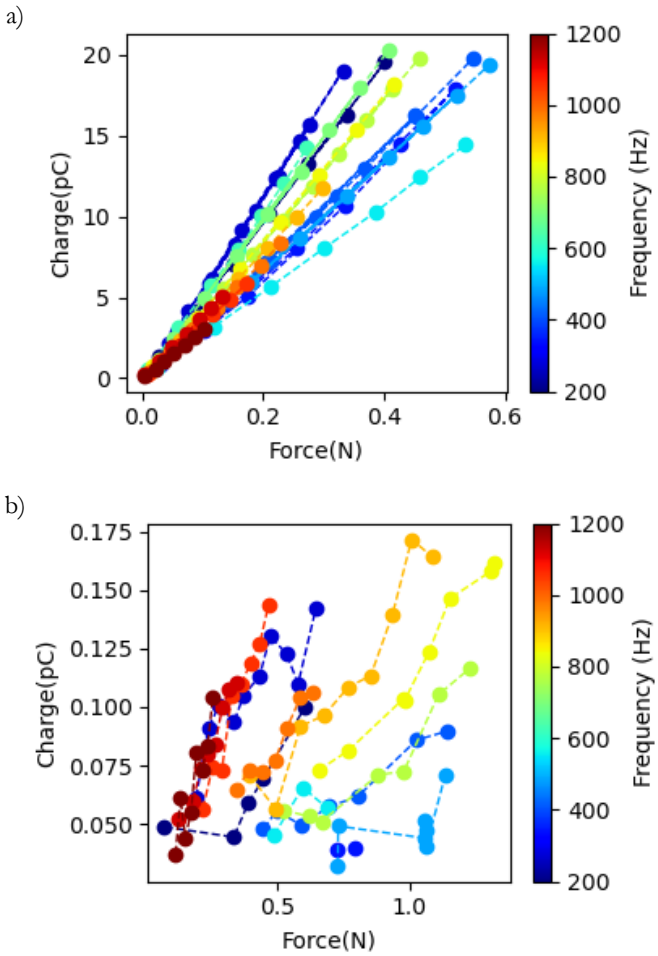

Figure 5.24: a) Linearity of charge-force response at different frequencies for two samples for p3D_3, b) The charge-force response for the sample without nanoparticles that was not post-cured is not linear.

One of the most important indicators of a piezoelectric response is the phase inversion under sample switching, that indicates the directionality of the sample polarization. In Figure 5.25 are depicted the phase difference for some of the tested samples. Before the poling procedure the samples were very different one from the other, since the electrical dipoles were randomly oriented. Some exhibited a phase inversion, some did not. The samples without piezoelectric nanoparticles did not exhibit a clear phase inversion for the sample switching (Figure 5.25b), while the samples with nanoparticles exhibited a clear phase inversion (Figure 5.25a) with rare exceptions to this trend relative to some critical frequencies.

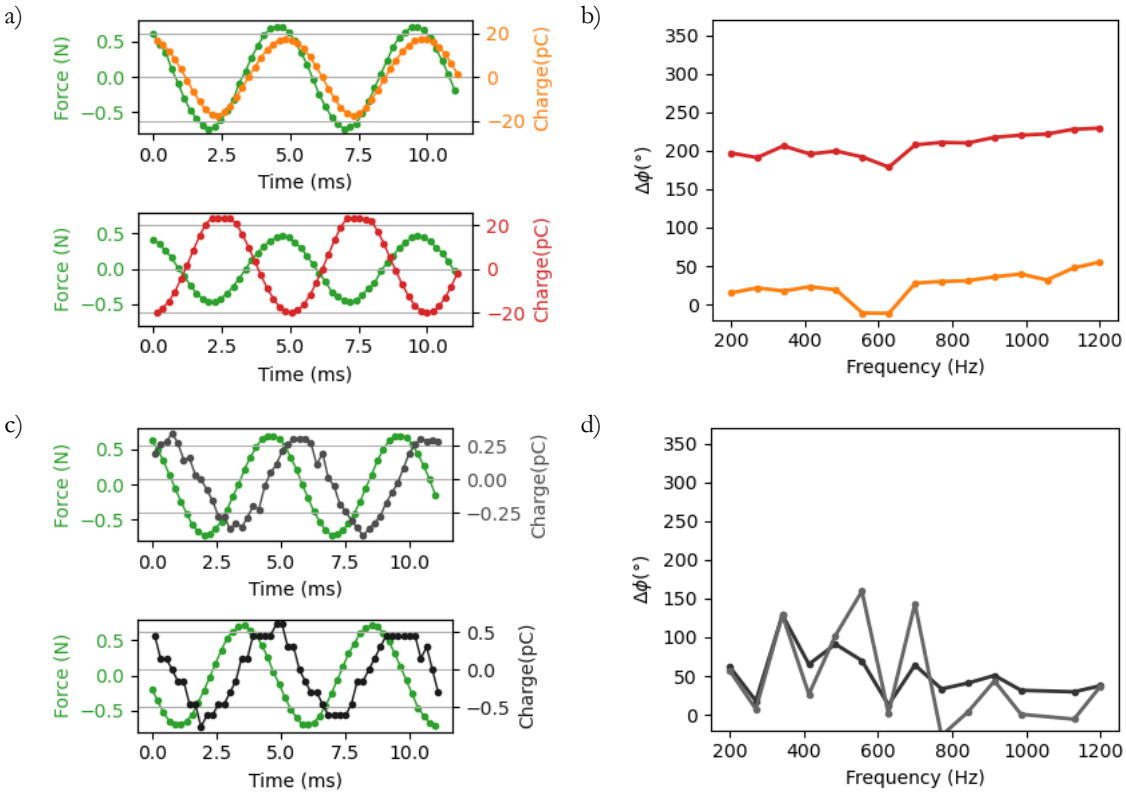

Figure 5.25: Phase inversion under sample switching for samples with and without piezoelectric nanoparticles. Force and charge signals (a: p3d_3, c: p3d_0), and phase difference between force and charge signals (b: p3d_3, d: p3d_0),).

For the linear response regime, the piezoelectric coefficient was computed for every tested frequency. In the figures in the following pages are reported these piezoelectric spectra. In particular in Figure 5.26 are depicted the piezoelectric spectra for some of the tested sample under different poling conditions. As can be observed in Figure 5.26a,b the samples that were not poled exhibited a small and casual piezoelectric behaviour, due to the random orientation of the single dipoles inside the matrix. In many cases it was not possible to compute a piezoelectric coefficient due to the absence of a measurable response. As can be seen in Figure 5.26c,d,e,f the samples without nanoparticles (in black) that went under the poling procedure exhibit a low electro-mechanical coupling behaviour, and, in some cases, they also exhibit a phase inversion under sample switching. By confronting the second and third row it should be apparent that the samples poled at -1200V/mm for 7 hours show generally a higher performance than the samples poled at +1000V/mm for 5 hours. This result suggests the increased efficacy of the poling

procedure conditions with poling voltage and time. In the following Figure are reported samples of different kinds that were poled together at -1200kV for 7 hours.

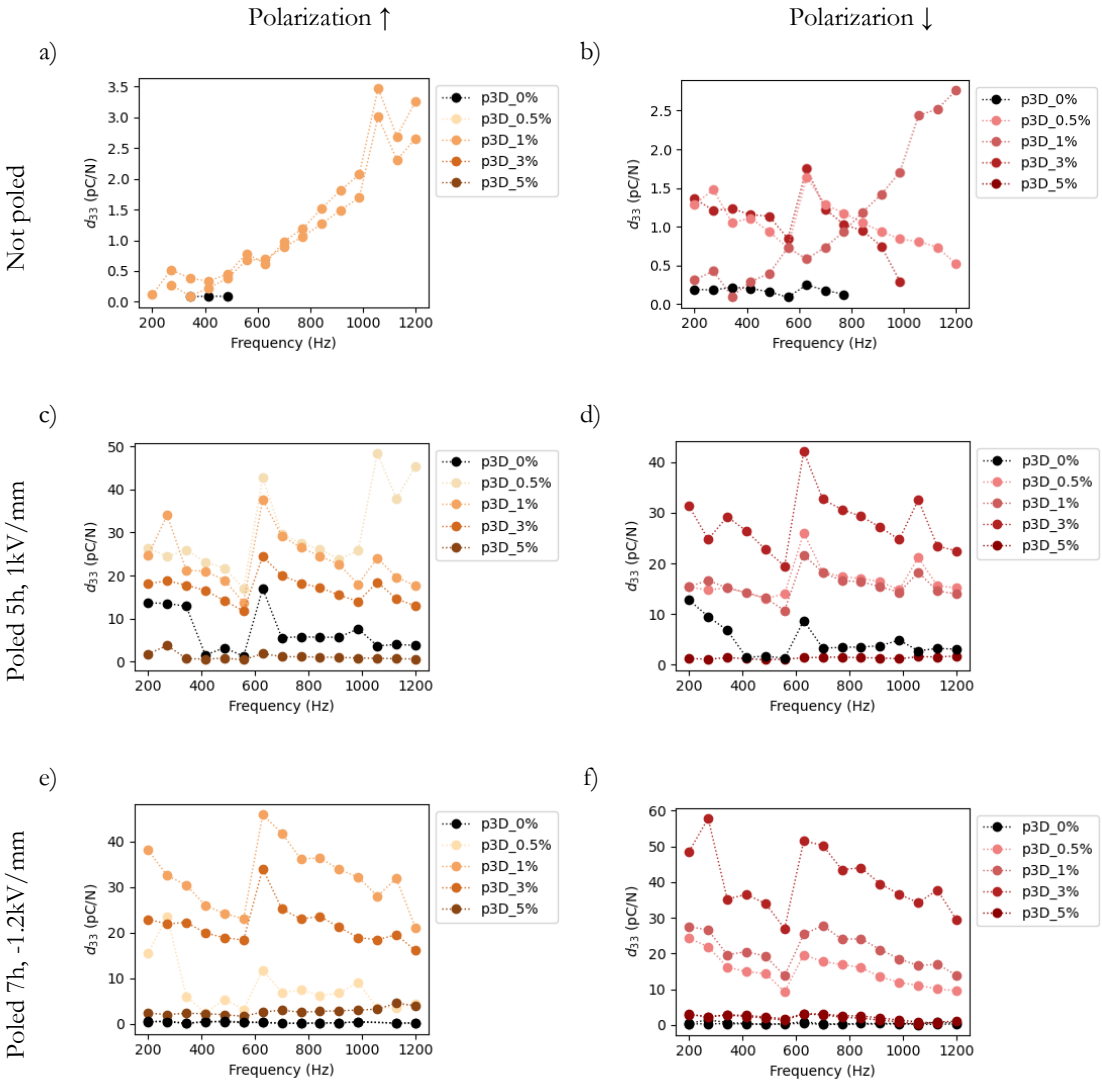

Figure 5.26: Piezoelectric spectra of similar samples under different poling conditions measured in the two configurations (polarization ↑, in orange, and ↓, in red). The data are not presented if the charge response is not linear, for example in some curves and points of a) and b). The 600Hz peak is an instrumental resonance, it does not give information about the piezoelectric behaviour of the nanocomposites.

In Figure 5.27 are reported different samples under the same poling conditions: in orange and red the standard samples (height 1mm, layer-height 0.1mm), in green samples with layer height of 0.025mm, in blue samples with height 0.5mm and layer-height 0.025mm, and in pink samples that showed poor nanoparticle dispersion.

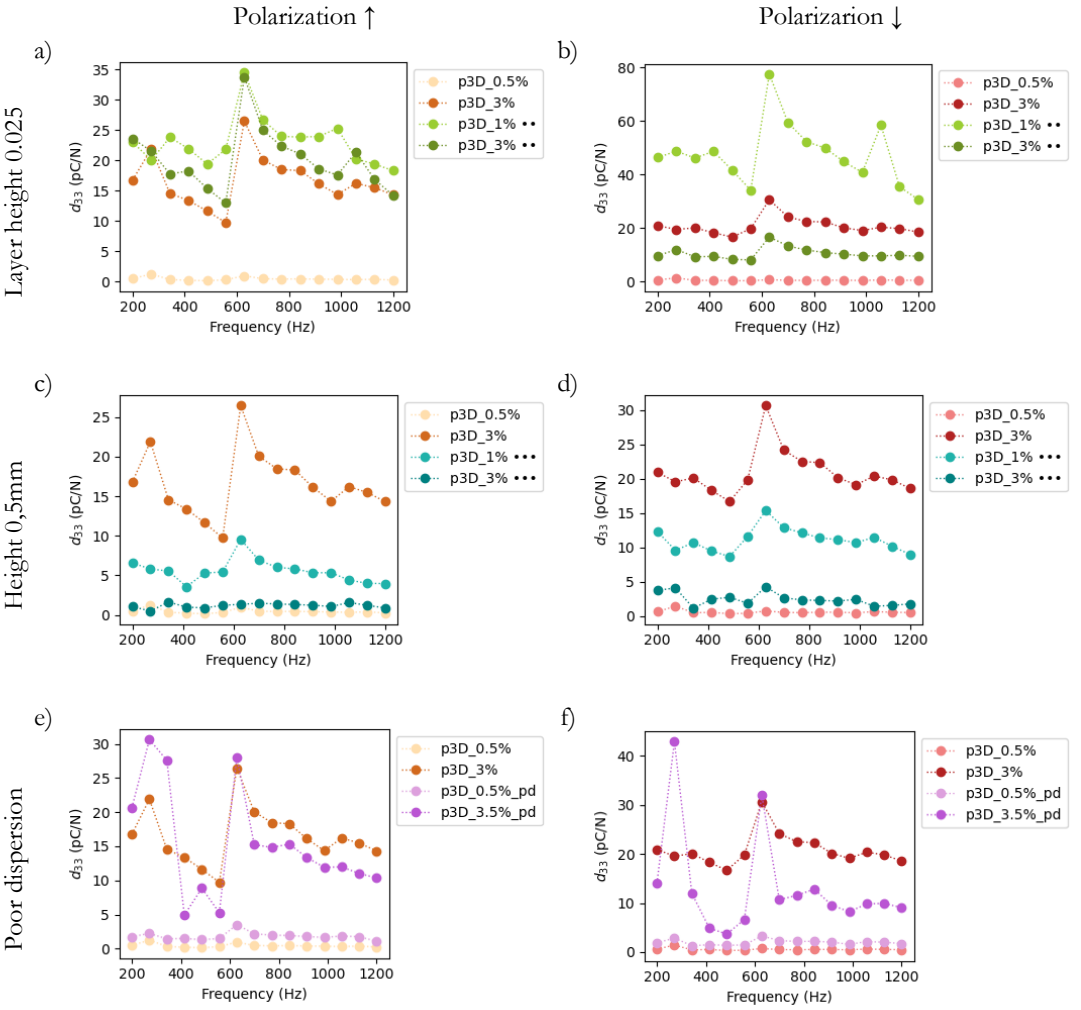

Figure 5.27: Piezoelectric spectra of different kind of samples under the same poling conditions measured in the two configurations (polarization ↑ and ↓).

In Table 5.4, Figure 5.28, and Figure 5.29 are reported the average piezoelectric coefficients obtained for the various samples. The measures reported are the average coefficients over the whole spectrum, excluding the resonant frequencies where the phase response is deviating from the general trend, where different effects affect the

measurement (in particular around 600Hz, as discussed in detail in Section 3). The observations made observing the piezoelectric spectra were confirmed by the average piezoelectric coefficients.

As can be observed in Figure 5.28 the piezoelectric coefficient of the samples increases with the nanoparticle loading up until a threshold, then decreases. The samples printed with 0.025mm layers exhibited a low piezoelectric behaviour compared to the ones printed with 0.1mm layers. The two tested samples with poorly dispersed particles showed a completely different behaviour. These results' high scattering can be ascribed to the poor dispersion of the nanoparticles, that can result in very different samples within the same batch. The 0.5mm thick samples showed a similar performance dispersion. This could be ascribed to poor poling due to the height of the samples, which did not assure contact with both the poling plates, and therefore a non-uniform poling and heating.

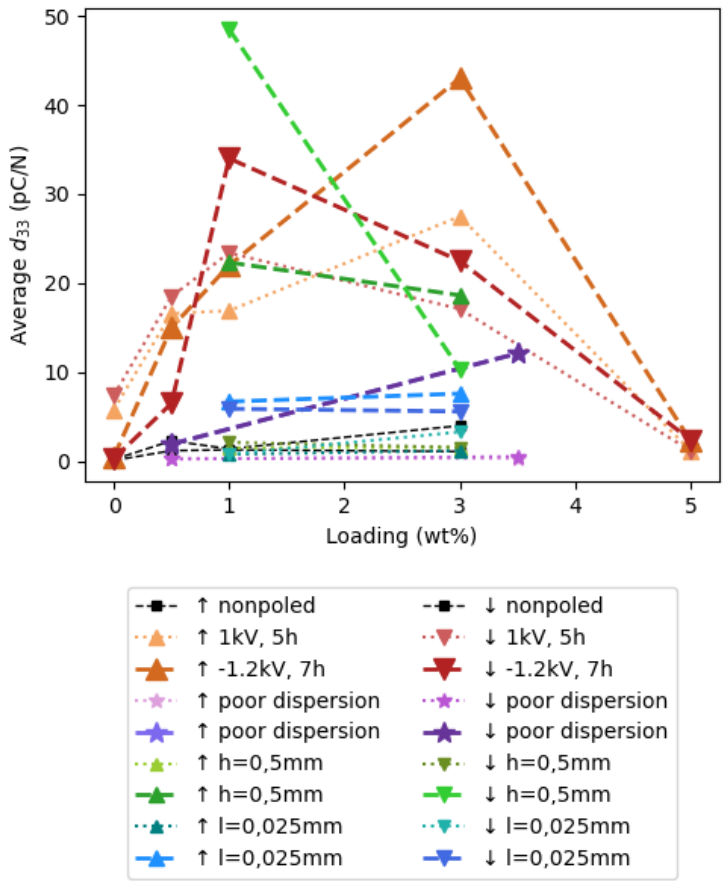

Figure 5.28: Average piezoelectric coefficient d_{33} for 3D printed piezo-resins.

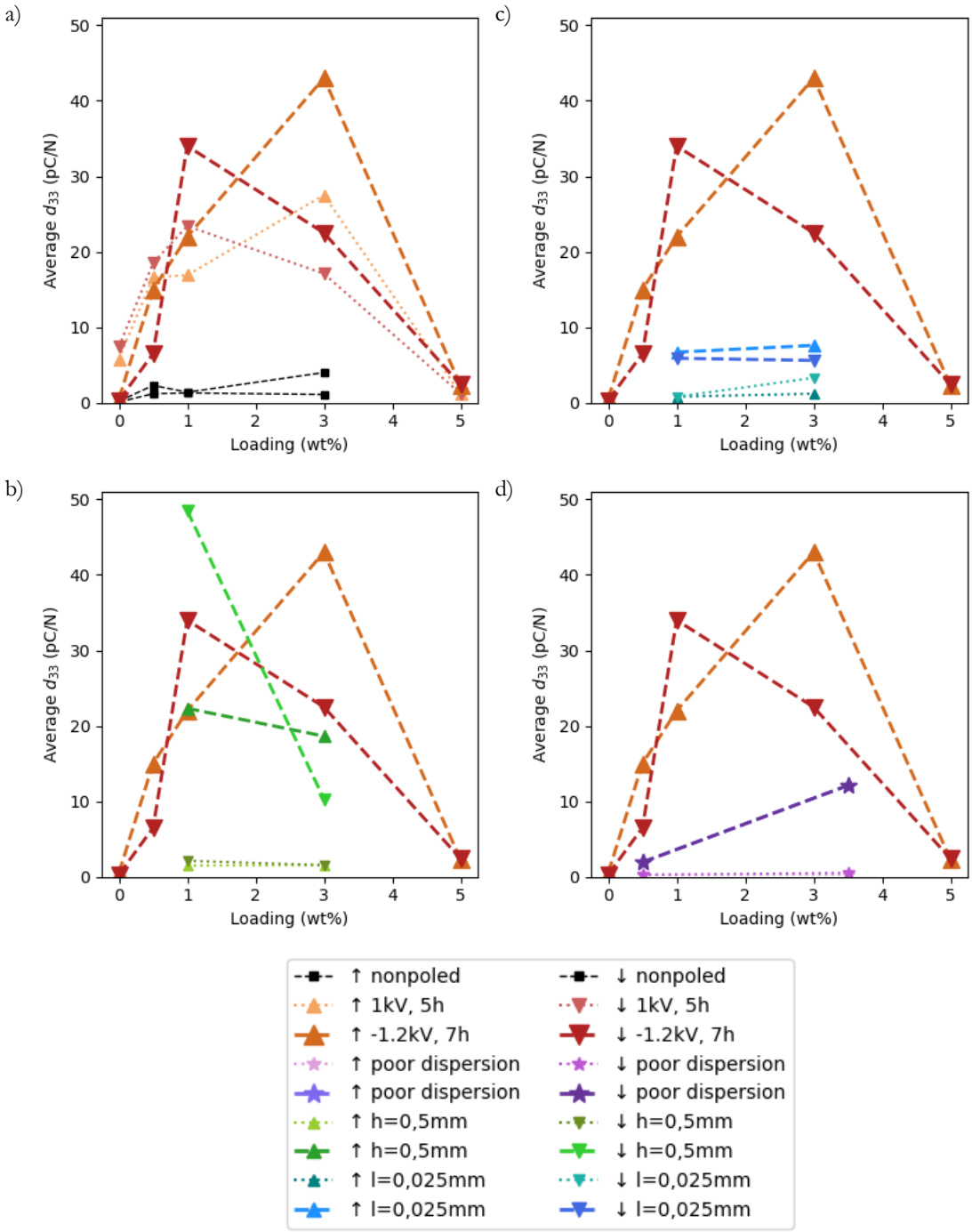

Figure 5.29: Average piezoelectric coefficient d_{33} for 3D printed piezo-resins, showed in different plots for more efficient comparison. The samples plotted two times are referred to replicas, fabricated under similar conditions.

	[BaTiO3] (wt%)	label	Post-curing	Poling	Disc thickness	Layer thickness	d33(pC/N) ↑	d33(pC/N) ↓	Δϕ inv
BATCH A - POLED 12/05/2021	0%	○	no	1kV/mm	1mm	0.1mm	0.14	0.16	no
	0%	•	60°, 1h	1kV/mm	1mm	0.1mm	5.8	7.4	yes
	0.50%	•	60°, 1h	1kV/mm	1mm	0.1mm	16.6	18.5	yes
	1%	•	60°, 1h	1kV/mm	1mm	0.1mm	16.9	23.4	yes
	3%	•	60°, 1h	1kV/mm	1mm	0.1mm	27.5	17.1	yes
	5%	•	60°, 1h	1kV/mm	1mm	0.1mm	1.2	1.2	yes
	1%	•••	60°, 1h	1kV/mm	1mm	**0.025mm**	**0.8**	0.8	yes
	3%	•••	60°, 1h	1kV/mm	1mm	**0.025mm**	**1.2**	3.3	vague
BATCH B - NOT POLED	0%	•	60°, 1h	**no**	1mm	0.1mm	0.2	0.1	no
	0.50%	•	60°, 1h	**no**	1mm	0.1mm	2.3	1.2	yes
	1%	•	60°, 1h	**no**	1mm	0.1mm	1.4	1.3	no
	3%	•	60°, 1h	**no**	1mm	0.1mm	4.0	1.1	yes
	5%	•	60°, 1h	**no**	1mm	0.1mm			-
BATCH B - POLED 31/05/2021	0%	○	no	-1.2kV/mm	1mm	0.1mm	0.08	0.07	no
	0%	•	60°, 1h	-1.2kV/mm	1mm	0.1mm	0.5	0.3	no
	0.50%	•	60°, 1h	-1.2kV/mm	1mm	0.1mm	15.0	6.5	yes
	1%	•	60°, 1h	-1.2kV/mm	1mm	0.1mm	22.0	34.0	yes
	3%	•	60°, 1h	-1.2kV/mm	1mm	0.1mm	43.0	22.5	yes
	5%	•	60°, 1h	-1.2kV/mm	1mm	0.1mm	2.3	2.4	yes
	1%	•••	60°, 1h	-1.2kV/mm	1mm	**0.025mm**	**6.7**	5.9	yes
	3%	•••	60°, 1h	-1.2kV/mm	1mm	**0.025mm**	**7.6**	5.6	yes
BATCH C - POLED 02/07/2021	0.50%	*	60°, 1h	-1.2kV/mm	1mm	0,1mm	0.35	0.25	yes
	3.50%	*	60°, 1h	-1.2kV/mm	1mm	0,1mm	0.31	0.53	yes
	1%	••	60°, 1h	-1.2kV/mm	**0,5mm**	0,1mm	1.5	2.13	yes
	3%	••	60°, 1h	-1.2kV/mm	**0,5mm**	0,1mm	1.56	1.56	yes
BATCH D - POLED 08/07/2021	0%	•	60°, 1h	-1.2kV/mm	1mm	0,1mm	0.67	0.75	yes
	0.50%	•	60°, 1h	-1.2kV/mm	1mm	0,1mm	0.53	0.58	yes
	3%	•	60°, 1h	-1.2kV/mm	**0,5mm**	0,1mm	16.22	20.00	yes
	5%	•	60°, 1h	-1.2kV/mm	1mm	0,1mm	0.48	0.27	yes
	5%	•	60°, 1h	-1.2kV/mm	1mm	0,1mm	16.87	17.09	yes
	0.50%	*	60°, 1h	-1.2kV/mm	**0,5mm**	0,1mm	1.96	1.94	yes
	3.50%	*	60°, 1h	-1.2kV/mm	1mm	0,1mm	14.90	12.11	yes
	1%	••	60°, 1h	-1.2kV/mm	**0,5mm**	0,1mm	22.32	48.50	yes
	3%	••	60°, 1h	-1.2kV/mm	**0,5mm**	0,1mm	18.64	10.33	yes
	1%	•••	60°, 1h	-1.2kV/mm	1mm	**0,025mm**	5.51	10.28	yes
	3%	•••	60°, 1h	-1.2kV/mm	1mm	**0,025mm**	5.74	10.45	yes

Table 5.4: Average piezoelectric coefficients obtained for the various samples with bars representing the piezoelectric performance (d_{33}). One of the 5% samples poled in the last batch showed a piezoelectric performance significantly higher than the other tested samples with the same loading: two poled in different batches, and another one that went under the same poling procedure. This higher performance could be caused by a difference between this particular sample and its copies, for example a lower actual nanoparticle loading or a higher cross-linking of the polymer matrix, which lead to different mechanical properties. This result cannot be replicated and is treated here as an outlier.

5.4.3 Conclusions

A 3D printed nanocomposite based on a photopolymerizable resin for stereolithography and surface functionalized BaTiO3 nanoparticles was developed and its piezoelectric performance was characterized. During this stage of the project a SLA commercial resin matrix was employed, but the results are encouraging for the application of the same methodology to different and novel polymeric matrixes, for example biodegradable and biocompatible resins [202,203].

The results indicate that the 3D printed discs were piezoelectric, and their piezoelectric coefficient is comparable to the one of PVDF. This good performance compared to the soft piezoelectric nanocomposites reported in the previous Sections can be in part attributed to the sample rigidity, which transmits efficiently the vibrations to the nanoparticles. The loading threshold observed in Figure 5.28 could be caused by the softening of the matrix, or by the efficiency of the nanoparticle dispersion inside the matrix.

The effect of the printing layer height and the non-zero piezoelectric behaviour of the 0% loading sample suggest that there might be a double effect: piezoelectric on one side (due to the nanoparticles) and triboelectric / voided charged polymer, due to micro air bubbles inside the 3D printed material charged during the poling procedure.

5.5 NANOSTRUCTURED SCBD ELECTRODES

For polymeric nanocomposites the choice of the electrodes is an essential aspect to be addressed during the fabrication process. Since piezoelectricity is an electro-mechanical effect, coupling adhesion and compliance between the polymeric nanocomposite and the electrode is pivotal to enhance the material response. In order to enhance the efficacy of the electro-mechanical conversion of these materials the nanocomposites were equipped with monolithically integrated nanostructured electrodes, fabricated by means of supersonic cluster beam deposition of gold nanoparticles (SCBD, [154–156]). The procedure is described in Section 4.2.

The use of SCBD allows to obtain large surface area electrodes, physically interpenetrating with the polymer, which morphology is expected to dramatically increase the electrode/piezo-polymer interface area [169,204]. This was expected in turn to significantly increase the charge collection and transportation in response to the application of compressive loads.

5.5.1 Ionogel

An electrical resistance of about $100\Omega/cm$ was reached at a thickness of the deposited gold layer corresponding to 150nm. The feasibility of the approach was preliminary assessed through a static measurement, performed by manually applying compressive loads at the sample. This was sandwiched between the two planar charge collectors previously employed. The load was applied by regulating the micrometric screw controlling the dynamometer motion using the apparatus described above. For comparison, an IG/BAT-Nc without the integrated electrodes was tested in the same conditions. The output voltage was measured by using a charge amplifier elaborating the signal acquired from the charge collectors, using a classical circuit layout as the one reported in [134]. Due to variations of the input resistance introduced by the presence of the ion conductive ionogel, the voltage output is affected by an undetermined gain factor. Therefore, the measurements readout has merely a qualitative and comparative meaning in order to investigate on the effect of the cluster-assembled electrodes on the nanocomposite response.

As shown in Figure 5.30 the static tests showed a significant difference in the response between the bare IG/BAT-Nc (Figure 5.30, top) and the same material provided with the integrated electrodes (Figure 5.30, bottom). In fact, the nanocomposite having gold nanostructured electrodes required the application of a

compressive load equal to one tenth of that applied to the bare material in order to reach the same output response. This increased sensitivity is related to the presence of the integrated electrodes, which probably both enhanced the charge accumulation at the nanocomposite/metal interface and favoured the electrical contact between the sample and the charge collectors, decreasing the overall charge dispersion. This enhanced response was also confirmed by subjecting the samples to the same compressive load and by recording the output voltage, as shown in Figure 5.30.

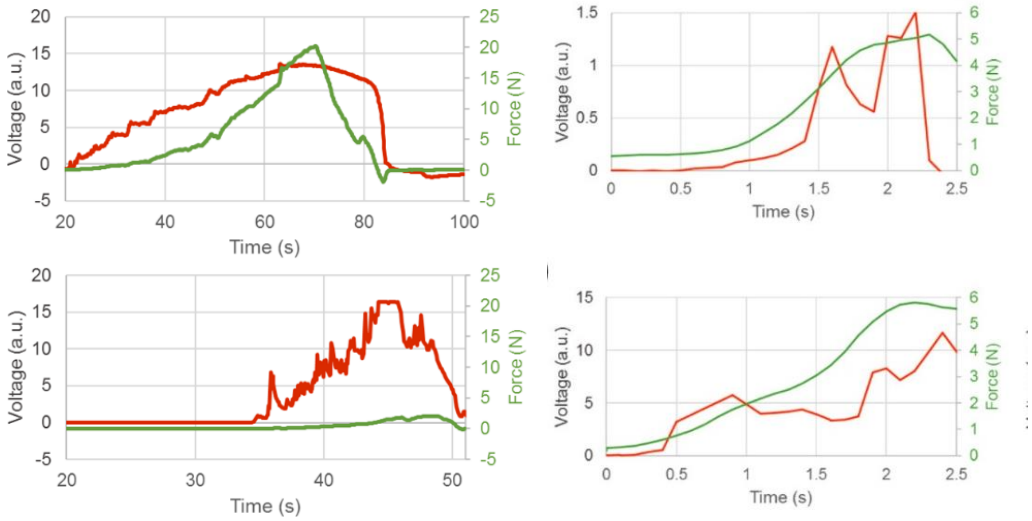

Figure 5.30: Static measurements to qualitatively evaluate the piezo-response of a bare IG/BAT-Nc (top row) and an IG/BAT-Nc provided with gold nanostructured electrodes (bottom row). Same output voltage with different compressive loads (left column), same compressive load different output voltages (right column).

A further assessment of the suitability of the SCBD approach was carried out by performing finger tapping measurements to obtain quantitative operative voltage values of the integrated electrodes conversion efficiency. For this purpose, the static load imposed by the dynamometer was removed and the upper charge collector was repeatedly tapped with a finger, exercising a force of about 1N, corresponding to a pressure of 10 kPa. The voltage readout took place by directly connecting the charge collectors to a multimeter and acquiring the voltage profile in time using a dedicated LabView program. An output voltage ranging from 30 mV to 40mV was measured Figure 5.31a.

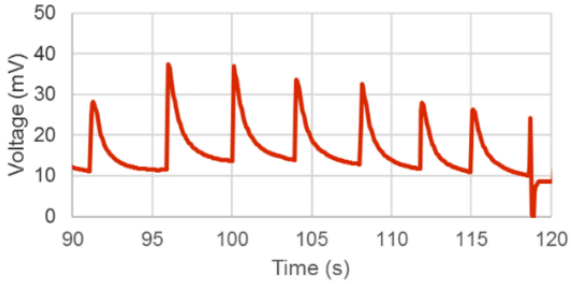

Figure 5.31: a) Finger tapping tests performed on an IG/BAT-Nc sample provided with integrated gold electrodes.

The observed output values were higher than those reported for purely piezoionic materials provided with nanocomposite surface electrodes, physically interlocked with the polymer [115,116,122]. Finger-tapping perturbations of the nanocomposite showed an improvement in the electromechanical transduction of the nanocomposite due to the presence of the metal electrodes, revealing an output voltage up to 40 mV for compressive stresses of about 10 kPa.

5.5.2 PDMS / BaTiO3 – Au

Gold nanostructured electrodes were deposited with the SCBD technique on the PDMS/$BaTiO_3$-DDA samples described in Section 0.

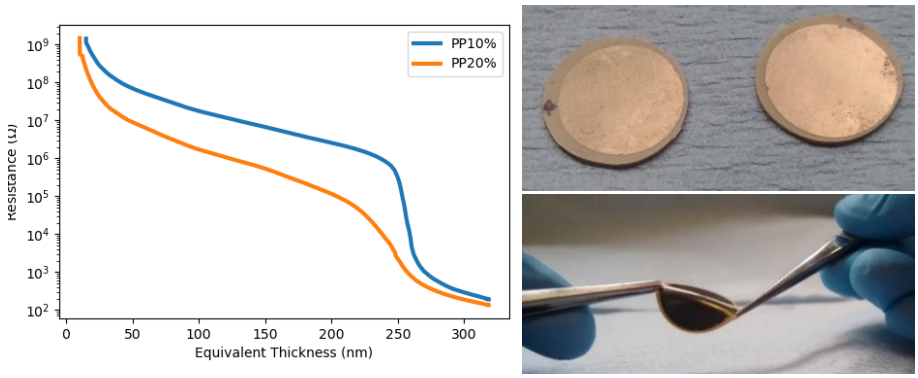

Figure 5.32: a) Evolution of the gold nanocomposite sheet resistance with deposited thickness. b) The PDMS-BaTiO3-DDA/Au nanocomposite is still a flexible and free-standing material. The nanostructured electrodes fabricated with this technique maintain the base material flexibility and stretchability without compromising their electrical properties. They are efficient in compression mode (minimal loss due to the nanostructure compression). They have several advantages in a free-standing environment in comparison with standard techniques electrodes because they maintain the mechanical characteristics of the substrate.

A resistance of about 100Ω was reached at a thickness of the gold layer corresponding to 320nm, and was maintained stable until the final thickness of 450nm. The percolation curve can be observed in Figure 5.32a. The thickness of the gold layer was measured using as a reference the gold nanoparticles deposited on a reference sensor (microbalance).

The nanostructured electrodes did not significantly alter the piezoelectric performance of the nanocomposites. This occurs due to the morphology of the nanostructured layer, which is compliant with the polymeric matrix: in the compression configuration of the characterization instrument the nanostructured electrode is not only compressed, but also stretched in the longitudinal direction, increasing its sheet resistance and dispersing part of the electrical charge generated by the nanocomposite. The nanostructured gold electrodes are particularly promising for free-standing applications since they allow to collect and transport the generated charges without limiting the nanocomposite flexibility and stretchability.

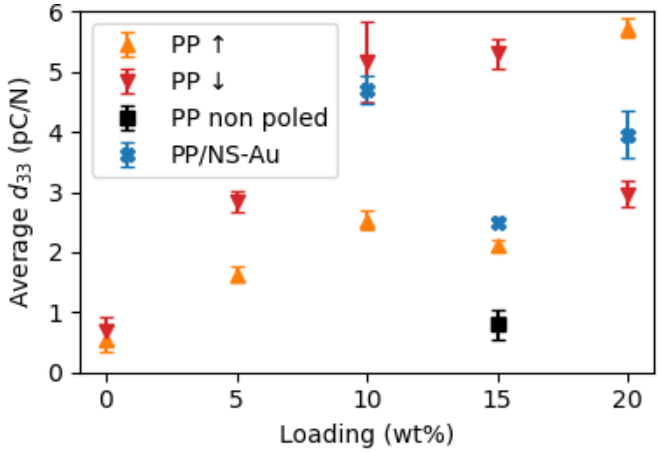

Figure 5.33: Mean d_{33} values averaged over the whole spectra and at least 3 separate measurements.

5.5.3 Summary and conclusions

The fabrication of cluster-assembled gold electrodes produced by SCBD was assessed for two different materials.

For the piezoionic/piezoelectric nanocomposite the integration of such electrodes resulted in an enhancement of the charge accumulation efficiency by a factor of ten, compared to the bare material, as demonstrated by static electro-mechanical tests. Finger-tapping perturbations of the nanocomposite also showed an improvement in the electromechanical transduction of the nanocomposite due to the presence of

the metal electrodes, revealing an output voltage up to 40 mV for compressive stresses of about 10 kPa.

For the PDMS/$BaTiO_3$ the integration of the nanostructured implanted electrodes did not significantly alter the piezoelectric performance of the nanocomposites, due to the morphology of the nanostructured layer, which, in the compression configuration of the characterization instrument, is compressed and stretched in the longitudinal direction, increasing its sheet resistance and dispersing part of the electrical charge generated by the nanocomposite. Nevertheless, the limited performance loss and the unaltered mechanical properties of the material are promising results in view of applications in free-standing configurations, in which the nanostructured electrodes are essential to obtain the mechanical compliance without sacrificing the electrical conductance.

CONCLUSIONS AND FUTURE OUTLOOKS

In this thesis work four different kinds of soft electro-mechanical transducers, based on different transduction mechanisms, have been fabricated and characterized and a dedicated instrument for their electro-mechanical characterization has been designed and developed.

The modular measuring system and characterization approach developed enabled the quantitative and systematic characterization on the electro-mechanical transduction ability of piezoelectric polymers and soft piezoelectric polymeric nanocomposites, which have potential applications for the development of wearable devices, distributed energy harvesting elements and soft robotic systems. The system allowed to measure samples with a piezoelectric coefficient down to 0,5pC/N, and the measurements were performed under controlled and reproducible conditions for a selected range of stimuli frequencies. Its modularity allows to expand the measurement range to higher frequencies if needed, by simply substituting the mechanical components, and it allows to increase the system functionalities by developing different signal conditioning circuits for other measurement types. For example a rectifier for charge accumulation, a voltage amplifier that amplify regardless of the input impedance, etc might be developed and integrated in the system. A damping of the mechanical resonant frequency of 600Hz that reduces the bandwidth of the instrument would furtherly increase the measurable frequencies.

An optimized procedure for the production of mechanically reproducible PDMS sample with the desired mechanical properties was developed. The study of percolation curves during the thin film growth of Supersonic Cluster Beam Deposited metal on various elastomer matrixes allowed to gain insight on the implantation process on such materials, and to develop an optimized process for the fabrication of an elastomer/metal nanocomposite, to be applied in a piezoresistive sensorized membrane. The electro-mechanical measurements performed on sample specimens and a membrane mock-up show promising results and demonstrate the concept of the sensorized membrane.

The fabrication and electro-mechanical characterization of a novel piezoionic/piezoelectric polymeric nanocomposite material based on a chemically cross-linked ionogel with embedded barium titanate ferroelectric nanoparticles was demonstrated. The composite responded to low frequency (0.1 Hz to 1 Hz) mechanical compressive stresses in the low-pressure regime (< 10 kPa) generating output voltages up to 8 mV. The combination of the piezoionic and piezoelectric activity resulted in an anisotropic electrical response to quasi-static mechanical perturbations, enabling to dis-criminate the sample orientation with respect to the load direction by monitoring the phase and amplitude modulation of the output signal. These results suggest that the piezoionic/piezoelectric nanocomposites constitute an interesting solution for the development of smart devices for discriminative touch sensing and objects localization in physically unstructured environments for soft robotics and wearable electronics applications.

A novel piezoelectric PDMS/$BaTiO_3$ nanocomposite was fabricated and characterized. The nanocomposite showed a voltage performance in line with similar nanocomposites in literature, although an effective comparison was not possible due to the previously discussed problematics of the characterization measurements in literature. The main novelty of this material lies in its thorough characterization, including charge and mechanical measurements, and in the description of the measuring methodology. Furthermore, the simple and straightforward material fabrication could be a useful base for further developments, for example for the integration of conformable implanted nanostructured electrodes, a topic that was discussed in a specific section of the thesis.

The 3D printed resins showed a piezoelectric behavior with a low nanoparticle loading, and their piezoelectric coefficient is comparable to the one of PVDF. This good performance can be in part attributed to the sample rigidity, which transmits efficiently the vibrations to the nanoparticles. The data collected suggest the possibility of a double transduction effect: piezoelectric on one side (due to the nanoparticles) and piezoelectrects on the other, due to micro air bubbles inside the 3D printed material charged during the poling procedure.

The fabrication of cluster-assembled gold electrodes produced by SCBD was also assessed for two different materials. For the piezoionic/piezoelectric nanocomposite the integration of such electrodes resulted in an enhancement of the charge accumulation efficiency by a factor of ten, compared to the bare material, as demonstrated by static electro-mechanical tests. Finger-tapping perturbations of the

nanocomposite also showed an improvement in the electromechanical transduction of the nanocomposite due to the presence of the metal electrodes, revealing an output voltage up to 40 mV for compressive stresses of about 10 kPa. For the PDMS/$BaTiO_3$ the integration of the nanostructured implanted electrodes did not significantly alter the piezoelectric performance of the nanocomposites, due to the morphology of the nanostructured layer, which, in the compression configuration of the characterization instrument, is compressed and stretched in the longitudinal direction, increasing its sheet resistance and dispersing part of the electrical charge generated by the nanocomposite. Nevertheless, the limited performance loss and the unaltered mechanical properties of the material are promising results in view of applications in free-standing configurations, in which the nanostructured electrodes will be essential to obtain the mechanical compliance without sacrificing the electrical conductance.

APPENDIX A: PIEZO-NANOCOMPOSITES

In the following table are reported some of the state-of-the-art piezoelectric nanocomposites presented in literature and their performance, with a focus on the characterization techniques used to assess their functioning. As can be clearly deduced from the table, there is currently no standard methodology for this measurement, and every research report different parameters to evaluate the behaviour of the presented material.

Year	Ref	Material	Output performance
2010	[132]	Polyetherimide / BaTiO3	Model ZJ-3A d33 piezometer, frequency fixed at 5Hz. The d33 value increased from 0.18 pC N−1 for pure PEI to 37.8 pC N−1 for the nanocomposite with 40 vol.% of BaTiO3. But the d33 value slightly decreased at higher filler content (>40 vol.%).
2012	[89]	BaTiO3 nanoparticles / CNT/PDMS composite	The NCG device generates an output voltage of ~3.2 V and a current of ~350 nA under periodic mechanical deformation to a strain of 0.33%.
2012	[131]	PVDF-TrFE / ZnO	Piezoelectric properties are measured by applying electric fields while measuring their response using a Sawyer-Tower circuit.
2012	[205]	PE / ZnO nanorods	Open-circuit voltage is 4 V and short-circuit current density is 0.15 μA/cm² when excited by acoustic vibrations at 100 dB.
2013	[206]	ZnO / SU-8	d33 = 5–8 pC/N for 20% wt. loading
2013	[207]	PMN–PT nanowire/PDMS nanocomposite	Output voltage up to 7.8 V and an output current up to 2.29 μA (current density of 4.58 μA/cm2);
2014	[134]	3D PEGDA / $BaTiO_3$ / TMSPM or CNTs	d_{33}~40 pC/N. Custom circuit, static measure.
2015	[208]	PVDF-TrFE / $BaTiO_3$	Output voltage up to 9.8 V and output power density of 13.5 μW/cm² under cyclic bending with tensile strain of 0.5%.

2015	[209]	P(VDF-TrFE) / NKN	Output voltage is 0.98 V and output current is 78 nA at 10 vol% NKN loading
2015	[210]	PVDF-HFP/Pt	Open-circuit output voltage is 18 V and short-circuit current is 17.7 mA under 4 MPa compressive stress.
2016	[211]	PDMS / MWCNT	Open circuit output voltage is ~30 V and short circuit output current is ~500 nA, and power density is ~9.0 μW/cm^3 under repeated human hand punching.
2016	[212]	P(VDF-TrFE) / GO	Output voltage is 4 V and power is 4.41 μW/cm^2.
2016	[213]	PDMS / $BiFeO_3$	Under human hand impacting, the output voltage is 3 V and current density is 0.12 μA/cm^2.
2017	[126]	PVDF-HFP / Ni-doped ZnO nanocomposites	A maximum generated output voltage of 1.2 V is achieved at 0.5 wt% Ni-doped ZnO.
2017	[133]	3D printed PVDF / $BaTiO_3$	d31=18pC/N calculated from peak-to-peak voltage at peak force. Excitation frequency of 45 Hz. Output 4 V upon gentle finger tapping.
2017	[136]	PDMS / ZnO / MWCNT / EGO	Qualitative studies: maximum voltage of 7.5 V Quantitative studies with bibrational apparaturs, maximum of 15.25 V is obtained Irregular finger assisted tapping, press-release operation and human footsteps yielding an output voltage of 36 V, 40 V and 50 V respectively
2018	[135]	PVDF / BTO-microstones / Ag nanowires	open-circuit voltage (VOC)of~14 V and short-circuit current (ISC)of~0.96 μA upon the application of a low pushing force of 3 N, cyclic pushing-releasing frequency of 5 Hz.
2018	[214]	P(VDF-TrFE) / $BaTiO_3$	Peak open circuit voltage (V_{oc}) of 9.3 V and short circuit current (I_{sc}) and 189 nA. 40% uniaxial stretching strain.
2018	[215]	PVDF / BT,GO	At 0.15 wt% graphene nanosheets and 15 wt% BT nanoparticles loading, open-circuit voltage is 11 V and electric power is 4.1 μW under a loading frequency of 2 Hz and strain of 4 mm. The peak voltage during a finger pressing-releasing process is 112 V.
2018	[216]	BT2 / PVDF	Output power density is 27.4 μW/cm^3 across 22 MΩ load at 10 g acceleration.
2019	[129]	PVDF-TrFE and filler NPs: niobium-doped $Pb(Zr,Ti)O_3$)	Enhanced remnant polarization of 9.1 μC/cm^2 at 100 Hz and high longitudinal piezoelectric coefficient of 101 pm/V. Output of 10 V in response to mechanical bending.

2019	[217]	Electrospun PVDF / ZnO / graphene oxide	Finger tapping 1.2V, mechanized tapping 2.5V. Input strain measured qualitatively. .
2019	[218]	PVDF / Fe-RGO	Output peak voltage is 5.1 V and short circuit current is 0.254 μA by human finger touch.
2019	[219]	P(VDF-TrFE) / BNNT	At 0.3 wt% BNNTs loading, the peak output voltage is 22 V and power density is 11.3 $\mu W/cm^2$ under 0.4 MPa maximum pressure.
2019	[220]	PVDF / Vitamin B_2	Output current is 12.2 μA and voltage is 61.5 V. The peak power density is 9.3 mW/cm^3 and energy conversion efficiency is 62%.
2019	[221]	BLF-PT / PI	Output voltage is 110 V and current density is 220 nA/ cm^2 at room temperature, with the impact from a human hand. The peak open-circuit voltage is 110 V and short-circuit current is 310 nA under 0.18 MPa pressure. The generator exhibited a voltage output 30 V at 300 °C
2020	[222]	P(VDF-TrFE) / (polydopamine-functionalized BT)	Output voltage is 6 V and current is 1.5 μA. Peak power density is 8.78 mW/m^2.
2020	[223,224]	PVDF / Ag-pBT	Peak output current is 142 nA and voltage is 10 V, which were 50% and 40% greater than those of PVDF/pBT-based scaffold, respectively.
2021	[128]	BCZT bioceramic and PLA biopolymer.	Open-circuit voltage and short-circuit current of 14.4 V and 0.55 μA, respectively, under gentle finger tapping. Maximum power density of about 7.54 mW/cm3 at a low resistive load of 3.5 MΩ.

APPENDIX B: SOFT AND FLEXIBLE GOLD MICROELECTRODES BY SUPERSONIC CLUSTER BEAM DEPOSITION AND FEMTOSECOND LASER PROCESSING

The results reported in this Appendix are reported in [170].

Contents lists available at ScienceDirect

Microelectronic Engineering

journal homepage: www.elsevier.com/locate/mee

Research paper

Soft and flexible gold microelectrodes by supersonic cluster beam deposition and femtosecond laser processing

Tali Dotan [a,b,*], Yuval Berg [a,c], Lorenzo Migliorini [d], Sara Moon Villa [d], Tommaso Santaniello [d], Paolo Milani [d], Yosi Shacham-Diamand [a,b]

[a] Department of Physical Electronics, School of Electrical Engineering, Faculty of Engineering, Tel- Aviv University, Ramat Aviv, 69978, Israel
[b] Department of Materials Science and Engineering, Faculty of Engineering, Tel- Aviv University, Ramat Aviv, 69978, Israel
[c] Additive Manufacturing Group, Orbotech Ltd PO Box 215, Yavne 81101, Israel
[d] CIMAINA and Physics Department, Università degli Studi di Milano, Via Celoria 16, I-20133, Milano, Italy

ARTICLE INFO

Keywords:
Microelectrodes
Micropatterning
Flexible electronics
Supersonic cluster beam deposition
Femtosecond lasers
Nanocomposite films

ABSTRACT

Soft and flexible microelectrodes are fabricated and patterned in a novel approach integrating supersonic cluster beam deposition (SCBD) of gold nanoparticles onto Polydimethylsiloxane (PDMS) followed by femtosecond (fs) laser processing. SCBD of gold nanoparticles in PDMS forms a nanocomposite film with mechanical properties similar to those of the elastomeric substrate. Electrically neutral metallic nanoparticles penetrate the polymeric matrix and distribute randomly up to a depth of a few hundred nanometers forming a path of ohmic conduction. High resolution patterning on soft substrates is a major challenge that was overcome by femtosecond laser ablation of micrometer lines with relatively very little thermal damage. Microelectrodes were fabricated with a width down to 3 μm. The printed metal line sheet resistance was 480 Ohm/square for the 100 nm thick film and 210 Ohm/square for the 200 nm thick film. The calculated average film specific resistivity was found to be 2.5–2.6mΩ-cm. It is ~3 orders of magnitude higher than that of physical vapor deposited gold; therefore, it is not suitable for high current interconnects but sufficient for low-current signal transmission such as for electrical and electrochemical biosensors.

1. Introduction

Soft and flexible electronics have been under intense research and development for various applications, e.g. wearables and bio-implants. Traditional electrodes are patterned on rigid substrates such as silicon or glass or on a flexible substrate such as polyimide. Those materials have mechanical characteristics that are very different than those of biologic surfaces. Therefore, placing electrodes on biological entities results in incomplete or ineffective contact deteriorating the signal and introducing noise. The signal deterioration can be in the form of attenuation and instabilities due to the relative movement of the electrodes and the biological entity, i.e. skin, leaf, etc. A possible solution to those problems is the use of soft and flexible electrodes mimicking the mechanical compliance of the biologic tissue. Such soft and flexible electrodes have already been applied in various applications using technologies such as neuroelectrodes [1], skin prosthesis [2], skin patchable electrodes [3,4] and electrochemical analysis by lab-on-a-chip on plastic, paper and textiles [5].

There are few candidates for soft and flexible electrodes, such as elastomeric polymers. Polydimethylsiloxane (PDMS) is the most obvious candidate today. PDMS is commonly used for biomolecular interfaces due to its elasticity, transparency, stability, biocompatibility, and its unique characteristics that allow surface functionalization, e.g. specifically modifying a material's surface functionality [6–8]. Gold electrodes on PDMS have been widely demonstrated in previous studies such as [1,9–19]. There are two main challenges in the integration of rigid metal film on the elastomeric substrate.

a. Mechanical incompatibility of the two materials. The difference of the Young modulus [20] and the coefficient of thermal expansion (CTE) [21] between the two materials cause mud-like cracking of the surface.
b. Processing incompatibility - Micro-patterning metallic layer on polymers.

* Corresponding author at: Department of Physical Electronics, School of Electrical Engineering, Faculty of Engineering, Tel- Aviv University, Ramat Aviv, 69978, Israel
E-mail address: talidot@gmail.com (T. Dotan).

https://doi.org/10.1016/j.mee.2020.111478
Received 15 July 2020; Received in revised form 3 November 2020; Accepted 7 November 2020
Available online 12 November 2020
0167-9317/

The mechanical problems appear in the form of cracking effects that may frequently occur in nanometer-thick metal films that are deposited, typically by physical vapor deposition (PVD) onto polydimethylsiloxane (PDMS) substrates. It was suggested by Baëtens et al. [22] that prior to the metal deposition, a thin, brittle silica-like crust is formed on the PDMS surface due to oxygen plasma. The deposition of a thin metal film subsequently generates cracks on the surface due to residual tensile stress with density dependent on the film's thickness. Additional studies have addressed this phenomenon, often referred to as "dry mud" islands [23]. Akogwu et al. have suggested that the cracks are formed by residual stress arising from the CTE differences between the elastomeric substrate and the gold thin film [21]. Seghir and Arscott proposed that the cracking of the silica-like crust and the metal film occurs if the residual tensile stresses are greater than the ultimate tensile strengths of layers [20]. In not-yet published work by Turjeman et al. [24], our group has developed a process to fabricate defect and stress-free metal thin film on elastomers through modelling their mechanical behavior. A few researchers have reported creating a percolating network that allows electrical continuity but suffer from high resistivity [21,23,25].

In this work, the electrodes on the elastomer were metallized by Supersonic Cluster Beam deposition (SCBD) of gold nanoparticles. This is a manufacturing technique relying on the use of supersonically accelerated beams of neutral metal clusters that can be directed onto a polymeric target to generate thin cluster-assembled metal layers physically interpenetrating with the polymer [26]. The process takes place at room temperature and involves low kinetic energies of the nanoparticles, avoiding thermal damage or chemical modification of the polymeric matrix under impact [14,27]. Using this method, the mechanical properties of the nanocomposite can be maintained close to that of the bare elastomer for significant metal volume concentrations [14]. Nanocomposite films with NP density above the critical value show electrical transport properties which are typical of thin metallic films [28].

The second integration challenge that needed to be resolved was gold line microscale patterning on the PDMS. Previous works on SCBD metallization over PDMS used stencil (shadow) masks for patterning where the acquired feature size was in the range of tens of microns [29]. The use of stencil masks has both resolution limits and also field size limits depending on the shadow mask span. Other candidates for printing small size features are transfer printing [19,30], laser induced forward transfer [31–34] and photolithography [1,10,18]. The latter is commonly used in thin film technologies on rigid and flexible substrates. However, photolithography on elastomers is a challenge and it is usually done when there is a rigid substrate under the soft material. Additionally, the large coefficient of thermal expansion and the swelling process of elastomers limit the minimum patterned feature size to about 100 μm [13] for conventional lithography.

In this work, femtosecond (fs) laser ablation was used for patterning the PDMS/Au nanocomposite film. Ultrashort laser ablation is unique in its capabilities of high spatial precision, minimal collateral thermal damage, high material removal rate, selective ablation of thin layers and the capability of processing a large range of materials. The ultrashort time of excitation allows the separation of the involved processes as excitation, melting, and material removal [35]. Ultrashort pulsed laser ablation stands out in the important role played by thermal effects. These include not only vaporization from the extreme outer surface and boiling from an extended near-surface region, but also phase explosion.

Thin film ablation on both planar and non-planar surfaces has been previously demonstrated [36–39]. The control parameters for providing ablation selectivity (i.e. complete removal of the thin film and leaving the substrate intact) are the laser fluence and scanning velocity (correlating to pulse overlap). The selectivity depends on the optical properties of both the substrate and the thin film.

The fabrication of soft and flexible electrodes with sub10 micrometer resolution faces severe problems emerging from both the materials' mechanical and surface properties, compatibility with conducting materials and also very often due to non-planar topography. The objective of this work was to develop a full integrated technology incorporating the metallization and patterning to achieve microelectrodes on flexible and soft polymers for various applications, e.g. electrochemical and electrical bio sensors, chemical sensors.

2. Methods and experimental details

The first step of the fabrication process is the PDMS substrate preparation. The pre-polymer gel and the cross linker (Sylgard® 184, Dow Inc.) are mixed at a 20:1 (w/w) ratio. The mixture is poured into a metal mold, and degassed thoroughly. The PDMS is cured in a pre-heated oven at 125 °C for 75 min and cooled down at room temperature. A 500 μm film was obtained. The PDMS substrate was mounted onto a sample holder and inserted into a vacuum chamber in the SCBD system.

The SCBD system consists of a pulsed micro-plasma cluster source (PMCS), an aerodynamic focuser, an expansion chamber, an implantation chamber and system of moving sample holders [40]. An Argon plasma is formed by high voltage discharge (750 V) and erodes a golden rod target placed in the PMCS. Sputtered gold atoms thermalize with argon and aggregate, creating a mixture of clusters and inert gas which exit the PMCS through a nozzle as a supersonic seeded beam of electrically neutral clusters. The beam passes through aerodynamic focuser where the nanoparticles are focused. It then expands at the expansion chamber where high vacuum is kept (10^{-7} Torr) and moves through the skimmer to the implantation chamber. The metal nanoparticles impact and penetrate the polymeric matrix with a soft implantation, without inducing any chemical or physical alteration due to their low kinetic energy (−0.5 eV/atom). During the deposition, the film thickness was monitored in-situ by alternatively directing the beam towards the PDMS samples and a quartz microbalance. The measured deposited mass was used to calculate the equivalent thickness t_{eq}, defined as the thickness of the film that a certain mass of clusters would form on a smooth, rigid surface of a hard substrate (e.g. silicon). The film resistivity was measured in- situ as well during the deposition process, to make sure that the deposited layer has a gold concentration above the percolation threshold. In this work, the deposited films were characterized by an equivalent thickness of 50, 100, 150, and 200 nm and a surface area of about 2 cm^2.

The patterning of the microelectrodes was done using Amplitude Systems Tangerine HP ultrashort laser ablation in atmospheric pressure. The laser wavelength was 343 nm, the pulse duration was 270 fs and the repetition rate was 12.5 kHz, maintained by pulse picking the fundamental 175 kHz repetition rate. The pulse fluence used was within the range of 0.3–1.14 μJ and was controlled by an internal acousto-optic modulator. A fast-galvanometric scanner followed by an F-theta lens (focal length = 100 mm) scans the linearly-polarized, 10 μm Gaussian laser spot diameter on the surface. The scanning velocity range was within the range of 12.5 mm/s to 250 mm/s.

Electrode lines were patterned using laser ablation of SCBD PDMS/AuNP films. The metal is ablated with equal-spaced and 50% overlap trenches so that it will act as an insulator while the electrodes remain unablated. The electrode length is 2 mm and their width values were 200 μm, 160 μm, 90 μm, 30 μm and 23 μm, 13 μm, and 3 μm.

The resistivity was measured from the current vs. voltage characteristics in a voltage sweep mode between 0 and 100 mV. The electrical characterization was carried out using a Keithley 2450 Source-Monitor-Unit (SMU) with wide and blunt end tips connected to the measurement system to prevent the penetration of the tips into the soft substrate.

HRSEM images were taken with tungsten deposition using 5 keV acceleration voltage and 0.4 nA beam current. The FIB cross section was processed with 30 V and 0.79 nA gallium dual beam system.

3. Results and discussion

3.1. Surface morphology

Fig. 1 shows images of the films which were fabricated by SCBD. Subsets (a) and (c) depict SEM cross sections of a PDMS substrate with 50 nm and 200 nm equivalent thickness, respectively and subsets (b) and (d), show SEM tops views of the surface morphology of 50 nm and 200 nm equivalent thickness, respectively. It can be seen that the gold nanoparticles create a fully covered layer and penetrate the PDMS surface to form a PDMS/ Au nanocomposite film. The film is comprised of 5–15 nm particles which maintain their shape in a randomly distributed structure.

Table 1 shows the parameters of the nanocomposte film. The actual measured thickness of the different films is presented against their equivalent thicknesses (t_{eq})- the thickness of a reference film deposited on a quartz microbalance using the same process conditions during the deposition. The equivalent thickness is measured on a hard substrate where the layer is deposited on top of the substrate and in the described process has a 50% gold density, or 9.66 g/cm^3. It can be seen that the density of the film increases with its thickness, and is in the range of 23–30% of the volume which correlates to 4.4–5.8 g/cm^3. The relatively low concentration of the gold nanoparticles in the PDMS matrix provides unique properties combining the matrix mechanical properties with the gold conductivity. The standard deviation of the measured thickness decreases with increasing film thickness, meaning that the uniformity of the film increases with its thickness (see Table 1).

As shown in Fig. 2, the actual thickness of the film is significantly larger than that of the equivalent thickness. The relation between the actual thickness and the equivalent thickness can be fitted to the following equation:

$$t_{actual} = k_1 * t_{eq}^{k_2}, \quad (1)$$

where $k_1 = 6.048$ and $k_2 = 0.759$ ($r^2 = 0.987$) (where both are in nm).

The composite material consists of the PDMS and the gold clusters. The initial pre- implantation PDMS has a low young modulus (of about 1.32–2.97 MPa [41]) and easily deforms as a response to an applied strain. During the gold cluster implantation, the composite material includes more than 20% gold in volume and 4 g/cm^3 in mass. The newly implanted clusters apply a force on the film including on the gold clusters in the film and push them further in the depth of the film. We assume that despite the fact that the gold percentage inside the composite film is below 50%, the two composites of the film form a well-organized, compact structure that does not allow further penetration of more clusters.

The layers' sheet resistance was measured on site. We characterized films with equivalent thickness in the range of 50-200 nm. The sheet resistance of the 50 nm equivalent thickness samples was very high while the rest were significantly low. Regarding the thicker gold samples, their sheet resistance allowed calculating the specific resistivity that decreased with increasing thickness. This indicates that the higher the gold concentration in the film is, the more conductive the

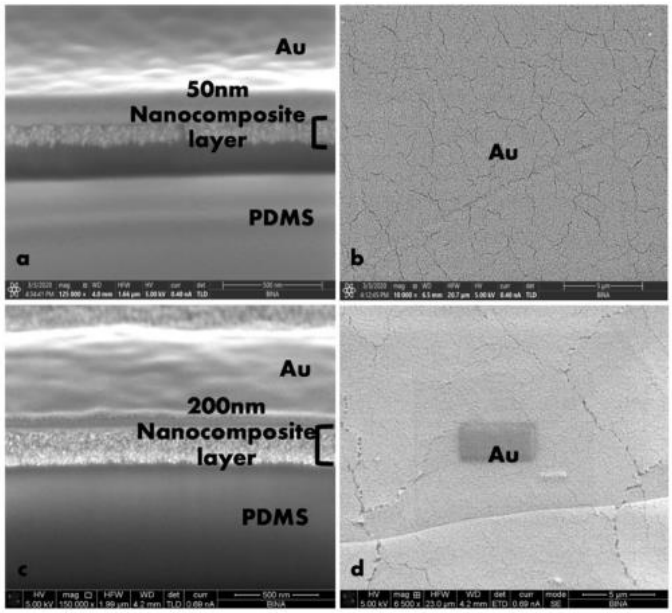

Fig. 1. SEM images of gold NP/ PDMS nanocomposite films fabricated by supersonic cluster beam deposition (SCBD). (a) and (c) FIB cross sections of 50 nm and 200 nm equivalent thickness respectively. (b) and (d) microcracks on gold surface of 50 nm and 200 nm equivalent thickness respectively. (For interpretation of the references to colour in this figure legend, the reader is referred to the web version of this article.)

Table 1
SCBD Gold/ PDMS film parameters.

Equivalent thickness [nm]	Actual thickness [nm]	Standard deviation [nm]	Percent gold [%(v/v)]	Gold density in film [g/cm^3]	Thin Film Sheet resistance [Ω/sq]	Fabricated Line Sheet resistance [Ω/sq]	Resistivity [Ω · cm]
50	114.1	19.9	21.9	4.23	–		
100	213.4	16.7	23.4	4.53	480	123.3	$2.63 \cdot 10^{-3}$
150	265.7	11.7	28.2	5.45	290		
200	330.3	4.3	30.3	5.85	210	75.1	$2.48 \cdot 10^{-3}$

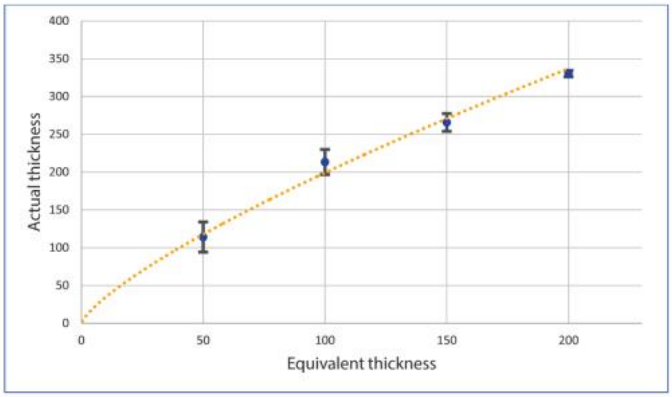

Fig. 2. Measured thickness (actual thickness) vs. the equivalent thickness. Dots represent the analyzed films and the dashed line is the best fitting.

microelectrode is.

The SEM images (see Figs. 1(b) and 1(d)) reveal microcracks in all of the deposited films, however their magnitudes differ from sample to sample. The 50 nm equivalent thickness film depicts "dry mud" islands of 1-5 μm with cracks of ~ a few tens of nm while the 200 nm equivalent thickness film had 20-40 μm islands and cracks above 100 nm thickness. This result is compatible with other studies done on conventional gold films where the increasing film thickness is associated with an increase in film grain size [21].

Unlike gold films deposited by conventional methods (e.g. e- beam

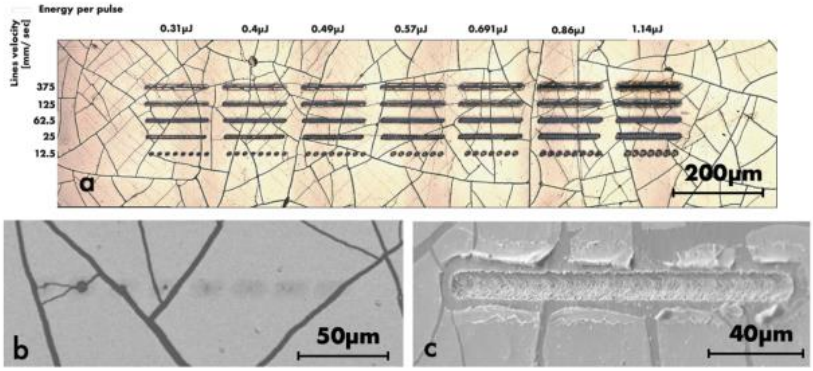

Fig. 3. Femtosecond laser ablated lines on nanocomposite films. (a) Optical imaging of matrix-line velocity [mm/s] vs. laser energy patterning [μJ]. (b) and (c) SEM imaging of zoomed patterning tests (a) 12.5 mm/s, 0.3 μJ (b) 375 mm/s, 1.14 μJ.

evaporation, sputtering etc.), the observed cracks are present only on the surface layer of the composite film. In the depth of the film, the cracks are very narrow and keep a close enough proximity between the particles to allow a conductive path.

3.2. Femtosecond laser patterning of AuNP film

The process window was optimized with a series of femtosecond laser procedures. Spot size, pulse temporal width, and Pulse repetition rate (PRR) were set to fixed values of ~10 μm, 270 fs and 12.5 kHz accordingly, while laser fluence and scanning velocities (pulse to pulse overlap) were varied. Fig. 3 depicts a typical matrix of such procedure.

The processed material has a non-uniform surface composed of randomly distributed gold nanoparticles in a PDMS matrix. The micro-processing opts to ablate and remove the gold aggregates from inside the film and have minimal effect on the polymer. The two materials have very dissimilar optical properties as the ablation threshold for gold surfaces were previously reported as 210–244 mJ/cm^2 [42,43] and the PDMS ablation threshold is 4.6 J/cm^2 [44]. A large process window is suggested in the range higher than the gold ablation threshold and lower than that of PDMS. A sweep of fluences in the defined region was carried out to find an optimal point, while scanning velocity (pulse to pulse overlap) was set from separated pulses to high overlap (>90%), where fabrication of good line roughness was targeted.

Two different phenomena can be observed in the two ends of the span, as shown in Fig. 3(b) and 3(c). In the low fluence regime (Fig. 3 (b)), single shots (bottom row lines) do not cause complete gold removal, since the fluence is not sufficient to fully-ablate the gold from the composite material. It can be suggested that gold nanoparticles in a polymeric matrix require higher fluence than standard gold film and also from gold NP induced film [45]. The continuous lines have lower scan velocity, meaning that the high overlap of the pulses results in full removal of the gold, as studied in a previous work [46].

As expected, for high fluence and low velocity, the laser processing induces PDMS ablation (Fig. 3(c)). In these process conditions, the gold is fully ablated but there is also significant surface damage. Based on the above observations, the process was tuned to a fluence of 400 mJ/cm^2 and scan speed of 45 mm/s, where clean patterning of low roughness lines was achieved.

3.3. Electrical characterization

Fig. 4 shows the measured sheet resistance multiplied by the actual thickness of the film ($R_s \cdot t_{actual}$) as a function of the film's actual thickness. The actual thickness is calculated by using the experimental dependence which had been found by fitting the measured thickness with its theoretical thickness as presented in Fig. 2 (Eq. 1). By definition, the measured sheet resistance can be expressed as $R_s = \rho \frac{l}{w \cdot t_{actual}}$. By rearrangement of the parameters we get that $R(t) \cdot t_{actual} = \rho(t) \frac{l}{w}$: the dependence of the function on the density of the film and its geometry. Since the length and width of the measurement sample don't change as the thickness of the deposited film grows, the trend is proportional to the resistivity of the film at each point. The behavior of resistivity can be separated in the two regimes. The pure PDMS has a very high resistivity of $4 \cdot 10^{15}$ Ω-cm. The implanted gold clusters provide electric conductance due to two different mechanisms- electrons tunneling effects and physical contact between conductor clusters (ohmic conductance). At low thickness, the "tunneling controlled regime", there is an exponential decay that can be attributed to tunneling effects. According to quantum mechanics tunneling theory, electrons in dispersed conducting particles in an insulator matrix can move between one conducting particle to another through tunneling. As shown by Simmons [47], the tunneling resistivity depends exponentially on the tunneling distance, or as presented in our experiment, it depends exponentially on the concentration of implanted conducting clusters in the insulating matrix. For a very small concentration, the distance between the adjacent clusters is higher than the electron- tunneling distance and no current is measured. At thicknesses higher than 200 nm, there is an "ohmic conduction regime" where a percolation network is formed. At these thicknesses the resistivity reaches a constant value, not dependent on the thickness or the density of the film. The electron passage is through contact between gold clusters, so that when a sufficient amount of connections is formed, the addition of gold does not change the conductance of the film.

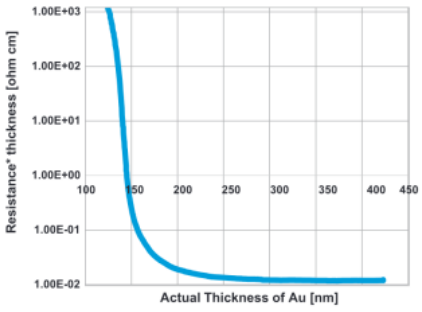

Fig. 4. Percolation curve. Presentation of the in-situ sheet resistance of gold NP/ PDMS nanocomposite film multiplied by the calculated actual thickness [Ωcm] vs the calculated actual thickness [nm].

Fig. 5 represents SEM and optical imaging of microelectrodes with varying line-width between 3 μm and 200 μm and 2 mm length. The microelectrodes were patterned using fs laser ablation process as described above with 0.3 μJ/pulse and pattern velocity of 45 mm/s. Ablation in a constant velocity was used in 50% overlap equally spaced lines to remove the conducting layer from the background, leaving a conducting layer only on the electrodes themselves.

The array of microelectrodes was tested, patterned on 75 nm t_{eq} film. All of the electrodes were conductive including 3 μm wide electrode. The measured sheet resistance 2.1–2.6kΩ/sqr.

Fig. 6 depicts the relation between 1/R to the electrode's width where R is the measured resistance of the electrode. The graph presents two trends of 100 nm and 200 nm t_{eq} films, where both have a linear relation with an ascending slope between 0.0015 and 0.02 cm. Both fitted linear lines do not start at the origin, however, they intersect with the Y axis at its positive side. The experimental data of 1/R vs. W, was fitted nicely ($r^2 = 0.997$, $r^2 = 0.959$ respectively) to a linear model:

$$1/R_{100nm} = A \cdot W_{1000m} + B\ [S] \quad (2)$$

The refitting results are shown in Table 2. We can see that both parameters A and B increase as the film thickness increases.

We assume a simple model that describes the dependence of resistance in the physical properties and in the heat effected zone (HAZ). We assume that the line resistance is in parallel to the resistance of the conducive path in the HAZ:

$$\frac{1}{R} = \frac{t \cdot W}{\rho \cdot L} + \frac{t_{HAZ} \cdot W_{HAZ}}{\rho_{HAZ} \cdot L} \rightarrow A = \frac{t}{\rho \cdot L} \text{ and } B = \frac{t_{HAZ} \cdot W_{HAZ}}{\rho_{HAZ} \cdot L} \quad (3)$$

Where ρ is the PDMS/AuNP composite film resistivity. W, L, and t are the electrode's width, length, and thickness respectively. t_{HAZ}, W_{HAZ} and ρ_{HAZ} are the thickness, width and resistivity of the heat affected zone, respectively.

It can be seen that the HAZ-related parameter B increases in correlation with the film thickness. The HAZ parameter B represents the effective widening of the microelectrode's line-width due to thermal

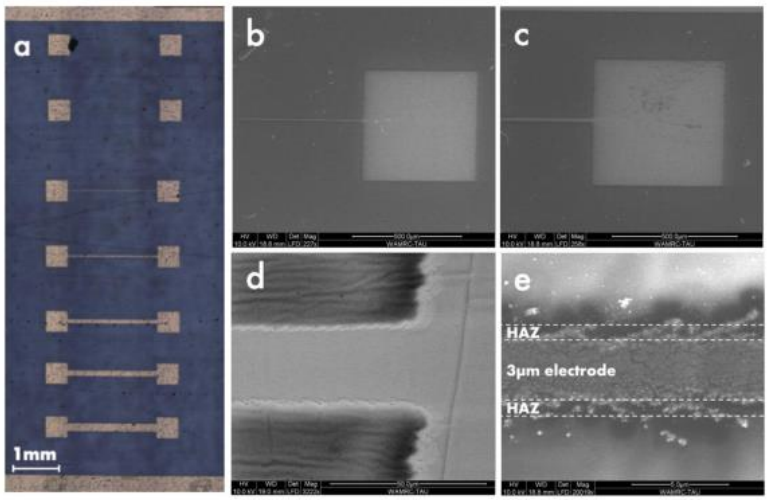

Fig. 5. The electrodes arrangement on PDMS obtained by (a) optical and (b-e) SEM imaging. The width of the electrodes in subsets (b-d) are 3 μm, 13 μm and 23 μm respectively. Figure (e) presents the electrode width and the heat affected zone.

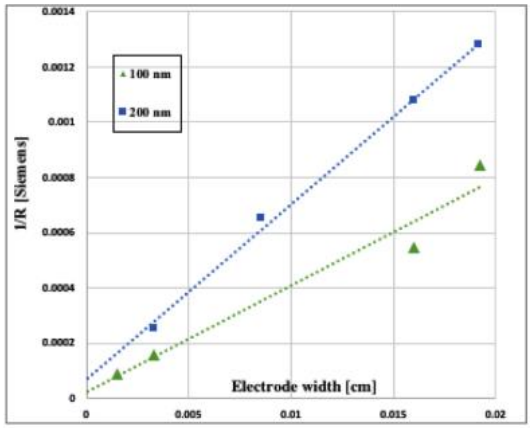

Fig. 6. Linear plot of 1/R (film resistivity) vs. the microelectrode's width for 100 nm and 200 nm equivalent thickness nanocomposite films.

effects. When assuming an ablation with a step structure, we can define the effective electrical HAZ width as B/A of eq. (3) which is proportional to the effective thickness of the film as shown in Table 2. This parameter represents the current flowing via the HAZ; thus, reducing the overall resistance. It is assumed that the increase of HAZ parameter is caused by an increase of the induced heat in the thicker film. The generated heat energy per unit area (Q') is proportional to the mass of the light absorbing gold layer that is rapidly ablated, and the mass is of course propositional to the layer's thickness: $Q' = t_{eff} \cdot c_p \cdot \triangle T$ where c_p is the heat capacitance of the gold/PDMS composite, ΔT is the temperature increase, and t_{eff} is effective thickness.

The film resistivity was extracted from each of the equations. The

Table 2
Fitting parameters of the sample conductance (1/R) to their width(W) (1/R = AxW + B).

Equivalent thickness (nm)	A (S/cm)	B (S)	Effective electrical HAZ width [μm]
100	0.0388	$2 \cdot 10^{-5}$	5.15
200	0.0637	$6 \cdot 10^{-5}$	9.42

resistivity of the 100 nm and 200 nm equivalent thickness films are $2.63e^{-3}\Omega \cdot$ cm and $2.48e^{-3}\Omega \cdot$ cm respectively, in the range of three orders of magnitude higher than bulk gold ($\rho_{gold} = 2.2e^{-6}\Omega \cdot$ cm). Such higher resistivity can be explained by considering the distribution of Au clusters inside the PDMS surface. It can be concluded that the Ohmic conduction (linear I vs V) can be achieved and the gold concentration in the structure is above the percolation threshold.

4. Conclusions

In this paper we demonstrated femtosecond laser patterning of supersonic cluster beam deposited film. The deposition of gold nanoparticle onto PDMS makes supersonic cluster deposition (SCBD) one of the most suitable methods for making interconnects on flexible substrates. Currently, it is patterned using shadow mask for its patterning which limits the line width resolution to few hundred microns. In this paper, we report SCBD gold/PDMS composite patterning with lateral resolution of 3 μm.

Our results indicate that the thickness of the composite film grows in the form of $t_{actual} = k_1 \cdot t_{sq}^{k_2}$. Where $k_1 = 6.048$ and $k_2 = 0.759$ and the density of gold within the substrate is between 23 and 30%. The PDMS removal by ablation requires higher energy fluence than gold. It was shown that by use of a 400 mJ/cm^2, it is possible to remove the gold from the nanocomposite film without damaging the substrate. The electrodes were fabricated down to 3 μm with an effective electrical HAZ of a few micrometers, depending on the film's thickness. It was found that at a certain concentration, the film reaches a constant resistivity which is not dependent on its thickness or density. This finding allows working with relatively thin layers of a few hundred nm and still obtaining the designed resistivity. The electrical resistivity of the film was found using two different models in the range of $2.5m\Omega \cdot cm$ to $10m\Omega \cdot cm$. This resistivity is 3 orders of magnitude higher than that of bulk gold, which makes it suitable for electrodes for biosensors and various additional applications.

We conclude that the combination of SCBD and femtosecond laser processing makes them a promising technology for maskless fabrication of soft and flexible electrodes. Future work on the method includes intensive investigation and modelling of the HAZ through heat transfer mechanisms and implementation of this method in sensors fabrication.

Declaration of Competing Interest

The authors declare that they have no known competing financial interests or personal relationships that could have appeared to influence the work reported in this paper.

Acknowledgements

YS, TD and YB thank the Israel Science Foundation, Grant no. 1616/17 titled "Feasibility and Modelling of Integrated Plant Cell Functional Micro Biochip System" and the Ministry of Science and Technology, Israel, Grant # 3-14345 titled "Single-cell Sensor". We would also like to acknowledge the Boris Mints Institute for Strategic Policy Solutions to Global Challenges, the Department of Public Policy and the Manna Centre for Food Security, Tel Aviv University for their generous support under the program "Plant-based heat stress whole-cell-biosensor" (Grant no. 590351) 2017. PM, TS, LM, SMV acknowledge the financial support of Fondazione CARIPLO under project ASSIST (2018-1726), under the program 'Call to support the knowledge transfer in advanced materials research'.

Credit Author Statement.

Tali Dotan: Conceptualization, Methodology, Investigation, Writing - Original Draft.
Yuval Berg: Investigation, Writing - Original Draft.
Lorenzo Migliorini: Investigation, Writing - Original Draft.
Sara Moon Villa: Resources.
Tommaso Santaniello: Writing - Review & Editing.
Paolo Milani: Supervision, Writing - Review & Editing.
Yosi Shacham- Diamand: Supervision, Writing - Review & Editing

References

[1] M.A. McClain, L.P. Clements, R.H. Shafer, R.V. Bellamkonda, M.C. LaPlaca, M. G. Allen, Highly compliant, microcable neuroelectrodes fabricated from thin film gold and PDMS, Biomed. Microdevices 13 (2) (2011) 361–373.
[2] J. Kim *et al.*, "Stretchable silicon nanoribbon electronics for skin prosthesis," *Nat. Commun.*, vol. 5, 2014.
[3] N.P. Sheeti, A. Madra, S. Basu, R.J. Mascarenhas, R.R. Kakarla, T.M. Aminabhavi, Skin Patchable Electrodes for Biosensor Applications: A Review, 2020.
[4] B.U. Hwang, et al., Transparent stretchable self-powered patchable sensor platform with ultrasensitive recognition of human activities, ACS Nano 9 (9) (2015) 8801–8810.
[5] A. Economou, C. Kokkinos, M. Prodromidis, Flexible plastic, paper and textile lab-on-a chip platforms for electrochemical biosensing, Lab Chip 18 (13) (2018) 1812–1830.
[6] K. Park, M. A. Woo, J. A. Lim, Y. R. Kim, S. W. Choi, and M. C. Lim, "In situ synthesis of directional gold nanoparticle arrays along ridge cracks of PDMS wrinkles," *Colloids Surfaces A Physicochem. Eng. Asp.*, vol. 558, no. June, pp. 186–191, 2018.
[7] D.C. Duffy, J.C. McDonald, O.J.A. Schueller, G.M. Whitesides, Rapid prototyping of microfluidic systems in poly(dimethylsiloxane), Anal. Chem. 70 (23) (Dec. 1998) 4974–4984.
[8] J. Zhou, A.V. Ellis, N.H. Voelcker, Recent developments in PDMS surface modification for microfluidic devices, Electrophoresis 31 (1) (2010) 2–16.
[9] S.P. Lacour, S. Wagner, Z. Huang, Z. Suo, Stretchable gold conductors on elastomeric substrates, Appl. Phys. Lett. 82 (15) (2003) 2404–2406.
[10] K.W. Meacham, R.J. Giuly, L. Guo, S. Hochman, S.P. DeWeerth, A lithographically-patterned, elastic multi-electrode array for surface stimulation of the spinal cord, Biomed. Microdevices 10 (2) (2008) 259–269.
[11] C. Minnai and P. Milani, "Metal-polymer nanocomposite with stable plasmonic tuning under cyclic strain conditions," *Appl. Phys. Lett.*, vol. 107, no. 7, 2015.
[12] A. Ryspayeva *et al.*, "A rapid technique for the direct metallization of PDMS substrates for flexible and stretchable electronics applications," *Microelectron. Eng.*, vol. 209, no. October 2018, pp. 35–40, 2019.
[13] T. Adrega and S. P. Lacour, "Stretchable gold conductors embedded in PDMS and patterned by photolithography: fabrication and electromechanical characterization," *J. Micromechanics Microengineering*, vol. 20, no. 5, p. 055025, May 2010.
[14] F. Borghi *et al.*, "Stretchable nanocomposite electrodes with tunable mechanical properties by supersonic cluster beam implantation in elastomers," *Appl. Phys. Lett.*, vol. 106, no. 12, 2015.
[15] S.P. Lacour, D. Chan, S. Wagner, T. Li, Z. Suo, Mechanisms of reversible stretchability of thin metal films on elastomeric substrates, Appl. Phys. Lett. 88 (20) (2006) 2004–2007.
[16] H. Stoyanov, M. Kollosche, S. Risse, R. Waché, G. Kofod, Soft conductive elastomer materials for stretchable electronics and voltage controlled artificial muscles, Adv. Mater. 25 (4) (2013) 578–583.
[17] Q. Zhang, J. Xu, Y. Liu, and H. Chen, "In-situ synthesis of poly (dimethylsiloxane)–gold nanoparticles composite films and its application in microfluidic systems (," vol. 184, pp. 352–357, 2008.
[18] M.G. Urdaneta, R. Delille, E. Smela, Stretchable electrodes with high conductivity and photo-patternability, Adv. Mater. 19 (18) (2007) 2629–2633.
[19] I. Byun, A. W. Coleman, and B. Kim, "Transfer of thin Au films to polydimethylsiloxane (PDMS) with reliable bonding using (3-mercaptopropyl) trimethoxysilane (MPTMS) as a molecular adhesive," *J. Micromechanics Microengineering*, vol. 23, no. 8, 2013.
[20] R. Seghir and S. Arscott, "Controlled mud-crack patterning and self-organized cracking of polydimethylsiloxane elastomer surfaces," *Sci. Rep.*, vol. 5, no. March, pp. 1–16, 2015.
[21] O. Akogwu, D. Kwabi, S. Midturi, M. Eleruja, B. Babatope, W.O. Soboyejo, Large strain deformation and cracking of nano-scale gold films on PDMS substrate, Mater. Sci. Eng. B Solid-State Mater. Adv. Technol. 170 (1–3) (Jun. 2010) 32–40.
[22] T. Baëtens, E. Pallecchi, V. Thomy, S. Arscott, Cracking effects in squashable and stretchable thin metal films on PDMS for flexible microsystems and electronics, Sci. Rep. 8 (1) (2018) 1–17.

[23] T. Adrega and S. P. Lacour, "Stretchable gold conductors embedded in PDMS and patterned by photolithography: Fabrication and electromechanical characterization," *J. Micromechanics Microengineering*, vol. 20, no. 5, 2010.
[24] I. Turjeman, T. Dotan, Y. Berg, Z. Kotler, D. Sherman, Y. Shacham-Diamand, Mechanical Modeling of Metal Thin Films on Elastomers for Femtosecond Laser Patterned Interconnects, Submitt. to JMEE, July, 2020.
[25] S.P. Lacour, D. Chan, S. Wagner, T. Li, Z. Suo, Mechanisms of reversible stretchability of thin metal films on elastomeric substrates, Appl. Phys. Lett. 88 (20) (2006) 2004–2007.
[26] L. Ravagnan, G. Divitini, S. Rebasti, M. Marelli, P. Piseri, and P. Milani, "Poly (methyl methacrylate)-palladium clusters nanocomposite formation by supersonic cluster beam deposition: A method for microstructured metallization of polymer surfaces," *J. Phys. D. Appl. Phys.*, vol. 42, no. 8, 2009.
[27] M. Marelli *et al.*, "Flexible and biocompatible microelectrode arrays fabricated by supersonic cluster beam deposition on SU-8," *J. Micromechanics Microengineering*, vol. 21, no. 4, 2011.
[28] A. Bellacicca, C. Prof, and F. Ragusa, "Smart materials for stretchable electronics, sensors and soft actuation," 2016.
[29] C. Ghisleri *et al.*, "Patterning of gold-polydimethylsiloxane (Au-PDMS) nanocomposites by supersonic cluster beam implantation," *J. Phys. D. Appl. Phys.*, vol. 47, no. 1, 2014.
[30] 6 John A. Rogers1 Dae-Hyeong Kim, 1* Jong-Hyun Ahn, 2* Won Mook Choi, 1* Hoon-Sik Kim, 1 Tae-Ho Kim, 1 Jizhou Song, 3 Yonggang Y. Huang, 5† Zhuangjian Liu, 6 Chun Lu, "stretch force reduction due to nanotube meander- ing. This structure provides a volume per strut of D'L 2 sin(120°) and a calculated density of r," *Nature*, vol. 320, no. April, pp. 507–511, 2008.
[31] Y. Berg, S. Winter, Z. Kotler, Y. Shacham-Diamand, Embedded metal microstructures in glass substrates by a combined laser trenching and printing process, J. Laser Micro Nanoeng. 13 (2) (2018) 131–134.
[32] Y. Berg, M. Zenou, O. Dolev, and Z. Kotler, "Temporal pulse shaping for smoothing of printed metal surfaces," *Opt. Eng.*, vol. 54, no. 1, p. 011010, 2015.
[33] M. Zenou, Z. Kotler, Printing of metallic 3D micro-objects by laser induced forward transfer, Opt. Express 24 (2) (2016) 1431–1446.
[34] M. Zenou, A. Sa'ar, and Z. Kotler, "Digital laser printing of aluminum micro-structure on thermally sensitive substrates," *J. Phys. D. Appl. Phys.*, vol. 48, no. 20, p. 205303, 2015.
[35] J.K. Chen, J.E. Beraun, Modelling of ultrashort laser ablation of gold films in vacuum, J. Opt. A Pure Appl. Opt. 5 (3) (2003) 168–173.
[36] C. Von Der Heide, M. Grein, G. Bräuer, and A. Dietzel, "Methodology of selective metallic thin film ablation from susceptible polymer substrate using pulsed femtosecond laser," *eprint arXiv:2002.00752*, pp. 1–11, 2020.
[37] J.F. Duesing, O. Suttmann, J. Koch, U. Stute, L. Overmeyer, Ultrafast laser patterning of thin films on 3-D shaped surfaces for strain sensor applications, J. Laser Micro Nanoeng. 7 (3) (2012) 311–315.
[38] S. Amoruso, N.N. Nedyalkov, X. Wang, G. Ausanio, R. Bruzzese, P.A. Atanasov, Erratum: ultrashort-pulse laser ablation of gold thin film targets: theory and experiment (thin solid films (2014) 550 190-198), Thin Solid Films 551 (2014) 205.
[39] E. Mishuk *et al.*, "Femtosecond laser processing of ceria-based micro actuators," *Microelectron. Eng.*, vol. 217, no. March, p. 111126, 2019.
[40] K. Wegner, P. Piseri, H. V. Tafreshi, and P. Milani, "Cluster beam deposition: A tool for nanoscale science and technology," *J. Phys. D. Appl. Phys.*, vol. 39, no. 22, 2006.
[41] I. D. Johnston, D. K. McCluskey, C. K. L. Tan, and M. C. Tracey, "Mechanical characterization of bulk Sylgard 184 for microfluidics and microengineering," *J. Micromechanics Microengineering*, vol. 24, no. 3, 2014.
[42] S. Preuss, A. Demchuk, M. Stuke, Sub-picosecond UV laser ablation of metals, Appl. Phys. A Mater. Sci. Process. 61 (1) (1995) 33–37.
[43] J.K. Chen, J.E. Beraun, Modelling of ultrashort laser ablation of gold films in vacuum, J. Opt. A Pure Appl. Opt. 5 (3) (2003) 168–173.
[44] H. Huang and Z. Guo, "Ultra-short pulsed laser PDMS thin-layer separation and micro-fabrication," *J. Micromechanics Microengineering*, vol. 19, no. 5, 2009.
[45] S.H. Ko, Y. Choi, D.J. Hwang, C.P. Grigoropoulos, J. Chung, D. Poulikakos, Nanosecond laser ablation of gold nanoparticle films, Appl. Phys. Lett. 89 (14) (2006) 2004–2007.
[46] O. Suttmann, J. Duesing, and L. Overmeyer, "Phenomenological model for prediction of complex ablation geometries in metal films using ultrashort laser pulses," *J. Laser Appl.*, vol. 28, no. 2, p. 022208, 2016.
[47] J.G. Simmons, Generalized formula for the electric tunnel effect between similar electrodes separated by a thin insulating film, J. Appl. Phys. 34 (6) (1963) 1793–1803.

BIBLIOGRAPHY

[1] S. Zanero, Cyber-Physical Systems, Computer. 50 (2017) 14–16. https://doi.org/10.1109/MC.2017.105.

[2] S.-H. Yang, Internet of Things Archives | Internet of Things, in: Springer, London, 2016: pp. 247–261. https://doi.org/10.1007/978-1-4471-5505-8_12.

[3] S.C. Mukhopadhyay, N.K. Suryadevara, Internet of Things: Challenges and Opportunities, Smart Sensors, Measurement and Instrumentation. 9 (2014) 1–17. https://doi.org/10.1007/978-3-319-04223-7_1.

[4] M.N. Kamel Boulos, N.M. Al-Shorbaji, On the Internet of Things, smart cities and the WHO Healthy Cities, International Journal of Health Geographics. 13 (2014) 1–6. https://doi.org/10.1186/1476-072X-13-10/COMMENTS.

[5] M.N. Kamel Boulos, B. Resch, D.N. Crowley, J.G. Breslin, G. Sohn, R. Burtner, W.A. Pike, E. Jezierski, K.Y.S. Chuang, Crowdsourcing, citizen sensing and sensor web technologies for public and environmental health surveillance and crisis management: Trends, OGC standards and application examples, International Journal of Health Geographics. 10 (2011) 1–29. https://doi.org/10.1186/1476-072X-10-67.

[6] H. Ghayvat, J. Liu, A. Babu, E. E Alahi, X. Gui, S.C. Mukhopadhyay, Internet of Things for smart homes and buildings: Opportunities and challenges, Australian Journal of Telecommunications and the Digital Economy. 3 (2015) 33–47. https://doi.org/10.18080/ajtde.v3n2.23.

[7] T.K.L. Hui, R.S. Sherratt, D.D. Sánchez, Major requirements for building Smart Homes in Smart Cities based on Internet of Things technologies, Future Generation Computer Systems. 76 (2017) 358–369. https://doi.org/10.1016/j.future.2016.10.026.

[8] D. Serpanos, M. Wolf, Industrial Internet of Things, Internet-of-Things (IoT) Systems. (2018) 37–54. https://doi.org/10.1007/978-3-319-69715-4_5.

[9] F. Kiani, A. Seyyedabbasi, Wireless sensor network and Internet of Things in precision agriculture, International Journal of Advanced Computer Science and Applications. 9 (2018) 99–103. https://doi.org/10.14569/IJACSA.2018.090614.

[10] A. Khanna, S. Kaur, Evolution of Internet of Things (IoT) and its significant impact in the field of Precision Agriculture, Computers and Electronics in Agriculture. 157 (2019) 218–231. https://doi.org/10.1016/j.compag.2018.12.039.

[11] M. Dholu, K.A. Ghodinde, Internet of Things (IoT) for Precision Agriculture Application, Proceedings of the 2nd International Conference on Trends in Electronics and Informatics, ICOEI 2018. (2018) 339–342. https://doi.org/10.1109/ICOEI.2018.8553720.

[12] S.M.R. Islam, D. Kwak, M.H. Kabir, M. Hossain, K.S. Kwak, The internet of things for health care: A comprehensive survey, IEEE Access. 3 (2015) 678–708. https://doi.org/10.1109/ACCESS.2015.2437951.

[13] Y. YIN, Y. Zeng, X. Chen, Y. Fan, The internet of things in healthcare: An overview, Journal of Industrial Information Integration. 1 (2016) 3–13. https://doi.org/10.1016/j.jii.2016.03.004.

[14] B. Reeder, A. David, Health at hand: A systematic review of smart watch uses for health and wellness, Journal of Biomedical Informatics. 63 (2016) 269–276. https://doi.org/10.1016/j.jbi.2016.09.001.

[15] J. Lockman, R.S. Fisher, D.M. Olson, Detection of seizure-like movements using a wrist accelerometer, Epilepsy and Behavior. 20 (2011) 638–641. https://doi.org/10.1016/j.yebeh.2011.01.019.

[16] B.H. Brinkmann, P.J. Karoly, E.S. Nurse, S.B. Dumanis, M. Nasseri, P.F. Viana, A. Schulze-Bonhage, D.R. Freestone, G. Worrell, M.P. Richardson, M.J. Cook, Seizure Diaries and Forecasting With Wearables: Epilepsy Monitoring Outside the Clinic, Frontiers in Neurology. 12 (2021) 1128. https://doi.org/10.3389/fneur.2021.690404.

[17] E.T. Roche, M.A. Horvath, I. Wamala, A. Alazmani, S.E. Song, W. Whyte, Z. Machaidze, C.J. Payne, J.C. Weaver, G. Fishbein, J. Kuebler, N. v. Vasilyev, D.J. Mooney, F.A. Pigula, C.J. Walsh, Soft robotic sleeve supports heart function,

Science Translational Medicine. 9 (2017). https://doi.org/10.1126/scitranslmed.aaf3925.

[18] J. Kim, M. Lee, H.J. Shim, R. Ghaffari, H.R. Cho, D. Son, Y.H. Jung, M. Soh, C. Choi, S. Jung, K. Chu, D. Jeon, S.T. Lee, J.H. Kim, S.H. Choi, T. Hyeon, D.H. Kim, Stretchable silicon nanoribbon electronics for skin prosthesis, Nature Communications. 5 (2014) 1–11. https://doi.org/10.1038/ncomms6747.

[19] F. Iida, C. Laschi, Soft robotics: Challenges and perspectives, Procedia Computer Science. 7 (2011) 99–102. https://doi.org/10.1016/j.procs.2011.12.030.

[20] C. Majidi, Soft Robotics: A Perspective - Current Trends and Prospects for the Future, Soft Robotics. 1 (2014) 5–11. https://doi.org/10.1089/soro.2013.0001.

[21] D. Trivedi, C.D. Rahn, W.M. Kier, I.D. Walker, Soft robotics: Biological inspiration, state of the art, and future research, Applied Bionics and Biomechanics. 5 (2008) 99–117. https://doi.org/10.1080/11762320802557865.

[22] T.G. Thuruthel, B. Shih, C. Laschi, M.T. Tolley, Soft robot perception using embedded soft sensors and recurrent neural networks, Science Robotics. 4 (2019) 1488. https://doi.org/10.1126/SCIROBOTICS.AAV1488.

[23] C. Majidi, Soft Robotics: A Perspective - Current Trends and Prospects for the Future, Soft Robotics. 1 (2014) 5–11. https://doi.org/10.1089/soro.2013.0001.

[24] P. Polygerinos, N. Correll, S.A. Morin, B. Mosadegh, C.D. Onal, K. Petersen, M. Cianchetti, M.T. Tolley, R.F. Shepherd, Soft Robotics: Review of Fluid-Driven Intrinsically Soft Devices; Manufacturing, Sensing, Control, and Applications in Human-Robot Interaction, Advanced Engineering Materials. 19 (2017) 1700016. https://doi.org/10.1002/adem.201700016.

[25] C. Dagdeviren, B.D. Yang, Y. Su, P.L. Tran, P. Joe, E. Anderson, J. Xia, V. Doraiswamy, B. Dehdashti, X. Feng, B. Lu, R. Poston, Z. Khalpey, R. Ghaffari, Y. Huang, M.J. Slepian, J.A. Rogers, Conformal piezoelectric energy harvesting and storage from motions of the heart, lung, and diaphragm, Proceedings of the National Academy of Sciences of the United States of America. 111 (2014) 1927–1932. https://doi.org/10.1073/pnas.1317233111.

[26] D. Chen, Q. Pei, Electronic Muscles and Skins: A Review of Soft Sensors and Actuators, Chemical Reviews. 117 (2017) 11239–11268. https://doi.org/10.1021/acs.chemrev.7b00019.

[27] Y. Qi, J. Kim, T.D. Nguyen, B. Lisko, P.K. Purohit, M.C. McAlpine, Enhanced piezoelectricity and stretchability in energy harvesting devices fabricated from buckled PZT ribbons, Nano Letters. 11 (2011) 1331–1336. https://doi.org/10.1021/nl104412b.

[28] R. Luttmann, D.G. Bracewell, G. Cornelissen, K. v. Gernaey, J. Glassey, V.C. Hass, C. Kaiser, C. Preusse, G. Striedner, C.F. Mandenius, Soft sensors in bioprocessing: A status report and recommendations, Biotechnology Journal. 7 (2012) 1040–1048. https://doi.org/10.1002/biot.201100506.

[29] A. Kumar, Methods and Materials for Smart Manufacturing: Additive Manufacturing, Internet of Things, Flexible Sensors and Soft Robotics, Manufacturing Letters. 15 (2018) 122–125. https://doi.org/10.1016/j.mfglet.2017.12.014.

[30] E. Navas, R. Fernandez, D. Sepulveda, M. Armada, P. Gonzalez-De-Santos, Soft Gripper for Robotic Harvesting in Precision Agriculture Applications, in: 2021 IEEE International Conference on Autonomous Robot Systems and Competitions, ICARSC 2021, Institute of Electrical and Electronics Engineers Inc., 2021: pp. 167–172. https://doi.org/10.1109/ICARSC52212.2021.9429797.

[31] G. Chowdhary, M. Gazzola, G. Krishnan, C. Soman, S. Lovell, Soft robotics as an enabling technology for agroforestry practice and research, Sustainability (Switzerland). 11 (2019) 6751. https://doi.org/10.3390/su11236751.

[32] D. Rus, M.T. Tolley, Design, fabrication and control of soft robots, Nature. 521 (2015) 467–475. https://doi.org/10.1038/nature14543.

[33] C. Majidi, Soft-Matter Engineering for Soft Robotics, Advanced Materials Technologies. 4 (2019) 1800477. https://doi.org/10.1002/admt.201800477.

[34] S. Kim, C. Laschi, B. Trimmer, Soft robotics: A bioinspired evolution in robotics, Trends in Biotechnology. 31 (2013) 287–294. https://doi.org/10.1016/j.tibtech.2013.03.002.

[35] S. Coyle, C. Majidi, P. LeDuc, K.J. Hsia, Bio-inspired soft robotics: Material selection, actuation, and design, Extreme Mechanics Letters. 22 (2018) 51–59. https://doi.org/10.1016/j.eml.2018.05.003.

[36] M. Piazzoni, E. Piccoli, L. Migliorini, E. Milana, F. Iberite, L. Vannozzi, L. Ricotti, I. Gerges, P. Milani, C. Marano, C. Lenardi, T. Santaniello, Monolithic Three-Dimensional Functionally Graded Hydrogels for Bioinspired Soft Robots Fabrication, Soft Robotics. (2021). https://doi.org/10.1089/soro.2020.0137.

[37] C. Laschi, M. Cianchetti, B. Mazzolai, L. Margheri, M. Follador, P. Dario, Soft robot arm inspired by the octopus, Advanced Robotics. 26 (2012) 709–727. https://doi.org/10.1163/156855312X626343.

[38] M. Wehner, R.L. Truby, D.J. Fitzgerald, B. Mosadegh, G.M. Whitesides, J.A. Lewis, R.J. Wood, An integrated design and fabrication strategy for entirely soft, autonomous robots, Nature 2016 536:7617. 536 (2016) 451–455. https://doi.org/10.1038/NATURE19100.

[39] Y. Li, Y. Chen, T. Ren, Y. Hu, H. Liu, S. Lin, Y. Yang, Y. Li, J. Zhou, A dual-mode actuator for soft robotic hand, IEEE Robotics and Automation Letters. 6 (2021) 1144–1151. https://doi.org/10.1109/LRA.2021.3056357.

[40] N. Lu, D.H. Kim, Flexible and Stretchable Electronics Paving the Way for Soft Robotics, Soft Robotics. 1 (2014) 53–62. https://doi.org/10.1089/soro.2013.0005.

[41] M. Pan, C. Yuan, X. Liang, J. Zou, Y. Zhang, C. Bowen, Triboelectric and Piezoelectric Nanogenerators for Future Soft Robots and Machines, IScience. 23 (2020) 101682. https://doi.org/10.1016/J.ISCI.2020.101682.

[42] G. Alici, Softer is harder: What differentiates soft robotics from hard robotics?, MRS Advances. 3 (2018) 1557–1568. https://doi.org/10.1557/adv.2018.159.

[43] C. Zhang, P. Zhu, Y. Lin, Z. Jiao, J. Zou, Modular Soft Robotics: Modular Units, Connection Mechanisms, and Applications, Advanced Intelligent Systems. 2 (2020) 1900166. https://doi.org/10.1002/aisy.201900166.

[44] C. Zhang, P. Zhu, Y. Lin, Z. Jiao, J. Zou, Modular Soft Robotics: Modular Units, Connection Mechanisms, and Applications, Advanced Intelligent Systems. 2 (2020) 1900166. https://doi.org/10.1002/aisy.201900166.

[45] A.G. Olabi, Encyclopedia of smart materials, Choice Reviews Online. 40 (2003) 40-4349-40–4349. https://doi.org/10.5860/choice.40-4349.

[46] G. Bao, H. Fang, L. Chen, Y. Wan, F. Xu, Q. Yang, L. Zhang, Soft robotics: Academic insights and perspectives through bibliometric analysis, Soft Robotics. 5 (2018) 229–241. https://doi.org/10.1089/soro.2017.0135.

[47] S.I. Rich, R.J. Wood, C. Majidi, Untethered soft robotics, Nature Electronics. 1 (2018) 102–112. https://doi.org/10.1038/s41928-018-0024-1.

[48] B. Oh, Y.G. Park, H. Jung, S. Ji, W.H. Cheong, J. Cheon, W. Lee, J.U. Park, Untethered Soft Robotics with Fully Integrated Wireless Sensing and Actuating Systems for Somatosensory and Respiratory Functions, Soft Robotics. 7 (2020) 564–573. https://doi.org/10.1089/soro.2019.0066.

[49] C.S. Kim, H.M. Yang, J. Lee, G.S. Lee, H. Choi, Y.J. Kim, S.H. Lim, S.H. Cho, B.J. Cho, Self-Powered Wearable Electrocardiography Using a Wearable Thermoelectric Power Generator, ACS Energy Letters. 3 (2018) 501–507. https://doi.org/10.1021/acsenergylett.7b01237.

[50] V. Leonov, Energy harvesting for self-powered wearable devices, in: Wearable Monitoring Systems, Springer US, 2011: pp. 27–49. https://doi.org/10.1007/978-1-4419-7384-9_2.

[51] M. Shirvanimoghaddam, K. Shirvanimoghaddam, M.M. Abolhasani, M. Farhangi, V. Zahiri Barsari, H. Liu, M. Dohler, M. Naebe, Towards a Green and Self-Powered Internet of Things Using Piezoelectric Energy Harvesting, IEEE Access. 7 (2019) 94533–94556. https://doi.org/10.1109/ACCESS.2019.2928523.

[52] A.S. Adila, A. Husam, G. Husi, Towards the self-powered Internet of Things (IoT) by energy harvesting: Trends and technologies for green IoT, in: 2018 2nd International Symposium on Small-Scale Intelligent Manufacturing Systems, SIMS 2018, Institute of Electrical and Electronics Engineers Inc., 2018: pp. 1–5. https://doi.org/10.1109/SIMS.2018.8355305.

[53] H. Li, C. Tian, Z.D. Deng, Energy harvesting from low frequency applications using piezoelectric materials, Applied Physics Reviews. 1 (2014). https://doi.org/10.1063/1.4900845.

[54] S. Pan, Z. Zhang, Fundamental theories and basic principles of triboelectric effect: A review, Friction. 7 (2019) 2–17. https://doi.org/10.1007/s40544-018-0217-7.

[55] J. Heikenfeld, A. Jajack, J. Rogers, P. Gutruf, L. Tian, T. Pan, R. Li, M. Khine, J. Kim, J. Wang, J. Kim, Wearable sensors: modalities, challenges, and prospects, Lab on a Chip. 18 (2018) 217–248. https://doi.org/10.1039/C7LC00914C.

[56] M. Ha, J. Park, Y. Lee, H. Ko, Triboelectric generators and sensors for self-powered wearable electronics, ACS Nano. 9 (2015) 3421–3427. https://doi.org/10.1021/acsnano.5b01478.

[57] G.H. Haertling, Ferroelectric ceramics: History and technology, Journal of the American Ceramic Society. 82 (1999) 797–818. https://doi.org/10.1111/j.1151-2916.1999.tb01840.x.

[58] H. Kawai, The Piezoelectricity of Poly (vinylidene Fluoride), Japanese Journal of Applied Physics. 8 (1969) 975–976. https://doi.org/10.1143/jjap.8.975.

[59] S. Tadigadapa, K. Mateti, Piezoelectric MEMS sensors: State-of-the-art and perspectives, Measurement Science and Technology. 20 (2009). https://doi.org/10.1088/0957-0233/20/9/092001.

[60] P. Das, A. Datta Gupta, Energy harvesting using frequency vibration of MEMS structure, Journal of Electrical Engineering. 12 (2012) 209–216. https://www.scopus.com/inward/record.uri?eid=2-s2.0-84867134828&partnerID=40&md5=18e86df10478308e5edd137acc318774.

[61] K.S. Ramadan, D. Sameoto, S. Evoy, A review of piezoelectric polymers as functional materials for electromechanical transducers, Smart Materials and Structures. 23 (2014) 33001. https://doi.org/10.1088/0964-1726/23/3/033001.

[62] Anon, Ieee Standard on Piezoelectricity., American National Standards Institute, Standards. (1978) 74. https://doi.org/10.1109/IEEESTD.1988.79638.

[63] A.L. Kholkin, N.A. Pertsev, A. v. Goltsev, Piezoelectricity and crystal symmetry, in: Piezoelectric and Acoustic Materials for Transducer Applications, Springer, 2008: pp. 17–38. https://doi.org/10.1007/978-0-387-76540-2_2.

[64] N. Sezer, M. Koç, A comprehensive review on the state-of-the-art of piezoelectric energy harvesting, Nano Energy. 80 (2021) 105567. https://doi.org/10.1016/j.nanoen.2020.105567.

[65] D. Damjanovic, Ferroelectric, dielectric and piezoelectric properties of ferroelectric thin films and ceramics, Reports on Progress in Physics. 61 (1998) 1267–1324. https://doi.org/10.1088/0034-4885/61/9/002.

[66] Z. Zhao, V. Buscaglia, M. Viviani, M.T. Buscaglia, L. Mitoseriu, A. Testino, M. Nygren, M. Johnsson, P. Nanni, Grain-size effects on the ferroelectric behavior of dense nanocrystalline BaTiO3 ceramics, Physical Review B - Condensed Matter and Materials Physics. 70 (2004) 024107. https://doi.org/10.1103/PhysRevB.70.024107.

[67] K.M. Holsgrove, D.M. Kepaptsoglou, A.M. Douglas, Q.M. Ramasse, E. Prestat, S.J. Haigh, M.B. Ward, A. Kumar, J.M. Gregg, M. Arredondo, Mapping grain boundary heterogeneity at the nanoscale in a positive temperature coefficient of resistivity ceramic, APL Materials. 5 (2017) 066105. https://doi.org/10.1063/1.4989396.

[68] L. Jin, F. Li, S. Zhang, Decoding the fingerprint of ferroelectric loops: Comprehension of the material properties and structures, Journal of the American Ceramic Society. 97 (2014) 1–27. https://doi.org/10.1111/jace.12773.

[69] D. Damjanovic, Contributions to the piezoelectric effect in ferroelectric single crystals and ceramics, Journal of the American Ceramic Society. 88 (2005) 2663–2676. https://doi.org/10.1111/j.1551-2916.2005.00671.x.

[70] N. Zhang, S. Gorfman, H. Choe, T. Vergentev, V. Dyadkin, H. Yokota, D. Chernyshov, B. Wang, A.M. Glazer, W. Ren, Z.-G. Ye, Probing the intrinsic and extrinsic origins of piezoelectricity in lead zirconate titanate single crystals, Urn:Issn:1600-5767. 51 (2018) 1396–1403. https://doi.org/10.1107/S1600576718011317.

[71] W. Wersing, W. Heywang, H. Beige, H. Thomann, The Role of Ferroelectricity for Piezoelectric Materials, Springer Series in Materials Science. 114 (2008) 37–87. https://doi.org/10.1007/978-3-540-68683-5_3.

[72] A. Albareda, R. Pérez, Non-linear behaviour of piezoelectric ceramics, in: Multifunctional Polycrystalline Ferroelectric Materials, Springer, 2011: pp. 681–726. https://doi.org/10.1007/978-90-481-2875-4_15.

[73] L. Qian, H. Zhao, Nanoindentation of soft biological materials, Micromachines. 9 (2018). https://doi.org/10.3390/mi9120654.

[74] J.G. Bergman, J.H. McFee, G.R. Crane, Pyroelectricity and optical second harmonic generation in polyvinylidene fluoride films, Applied Physics Letters. 18 (1971) 203–205. https://doi.org/10.1063/1.1653624.

[75] K. Nakamura, Y. Wada, Piezoelectricity, pyroelectricity, and the electrostriction constant of poly(vinylidene fluoride), Journal of Polymer Science Part A-2: Polymer Physics. 9 (1971) 161–173. https://doi.org/10.1002/POL.1971.160090111.

[76] A.J. Lovinger, Ferroelectric polymers, Science (New York, N.Y.). 220 (1983) 1115–1121. https://doi.org/10.1126/SCIENCE.220.4602.1115.

[77] A. Vinogradov, F. Holloway, Electro-mechanical properties of the piezoelectric polymer PVDF, Ferroelectrics. 226 (1999) 169–181. https://doi.org/10.1080/00150199908230298.

[78] Y. Ting, Suprapto, A. Nugraha, C.W. Chiu, H. Gunawan, Design and characterization of one-layer PVDF thin film for a 3D force sensor, Sensors and Actuators, A: Physical. 250 (2016) 129–137. https://doi.org/10.1016/j.sna.2016.09.025.

[79] A. Kachroudi, S. Basrour, L. Rufer, A. Sylvestre, F. Jomni, Micro-structured PDMS piezoelectric enhancement through charging conditions, Smart Materials and Structures. 25 (2016). https://doi.org/10.1088/0964-1726/25/10/105027.

[80] J. Hillenbrand, G.M. Sessler, Quasistatic and Dynamic Piezoelectric Coefficients of Polymer Foams and Polymer Film Systems, IEEE Transactions on Dielectrics and Electrical Insulation. 11 (2004) 72–79. https://doi.org/10.1109/TDEI.2004.1266319.

[81] J. Hillenbrand, Z. Xia, X. Zhang, G.M. Sessler, Piezoelectricity of cellular and porous polymer electrets, in: Proceedings - International Symposium on Electrets, 2002: pp. 46–49. https://doi.org/10.1109/ise.2002.1042940.

[82] P. Fang, L. Holländer, W. Wirges, R. Gerhard, Piezoelectric d33coefficients in foamed and layered polymer piezoelectrets from dynamic mechano-electrical experiments, electro-mechanical resonance spectroscopy and acoustic-transducer measurements, Measurement Science and Technology. 23 (2012). https://doi.org/10.1088/0957-0233/23/3/035604.

[83] S. Mishra, L. Unnikrishnan, S.K. Nayak, S. Mohanty, Advances in Piezoelectric Polymer Composites for Energy Harvesting Applications: A Systematic Review, Macromolecular Materials and Engineering. 304 (2019) 1–25. https://doi.org/10.1002/mame.201800463.

[84] E.K. Akdogan, M. Allahverdi, A. Safari, Piezoelectric composites for sensor and actuator applications, IEEE Transactions on Ultrasonics, Ferroelectrics, and Frequency Control. 52 (2005) 746–775. https://doi.org/10.1109/TUFFC.2005.1503962.

[85] Y. Peng, Z. Wang, C. Man Wong, al -, W. Winci, L. Buffoni, H. Sadeghi, C.R. Bowen, al -Vitaly Yu Topolov, F. Levassort, V. Yu Topolov, M. Lethiecq, G. Ultrasons, A comparative study of different methods of evaluating effective electromechanical properties of 0-3 and 1-3 ceramic/polymer composites, Journal of Physics D: Applied Physics. 33 (2000) 2064. https://doi.org/10.1088/0022-3727/33/16/319.

[86] Z. Ahmad, A. Prasad, K. Prasad, A comparative approach to predicting effective dielectric, piezoelectric and elastic properties of PZT/PVDF composites, Physica B: Condensed Matter. 404 (2009) 3637–3644. https://doi.org/10.1016/J.PHYSB.2009.06.009.

[87] T. Yamada, T. Ueda, T. Kitayama, Piezoelectricity of a high-content lead zirconate titanate/polymer composite, Journal of Applied Physics. 53 (1982) 4328–4332. https://doi.org/10.1063/1.331211.

[88] T. Furukawa, K. Ishida, E. Fukada, Piezoelectric properties in the composite systems of polymers and PZT ceramics, Journal of Applied Physics. 50 (1979) 4904–4912. https://doi.org/10.1063/1.325592.

[89] K. il Park, M. Lee, Y. Liu, S. Moon, G.T. Hwang, G. Zhu, J.E. Kim, S.O. Kim, D.K. Kim, Z.L. Wang, K.J. Lee, Flexible nanocomposite generator made of BaTiO 3 nanoparticles and graphitic carbons, Advanced Materials. 24 (2012) 2999–3004. https://doi.org/10.1002/adma.201200105.

[90] C.S. Smith, Piezoresistance effect in germanium and silicon, Physical Review. 94 (1954) 42–49. https://doi.org/10.1103/PhysRev.94.42.

[91] A.A. Barlian, W.T. Park, J.R. Mallon, A.J. Rastegar, B.L. Pruitt, Review: Semiconductor piezoresistance for microsystems, Proceedings of the IEEE. 97 (2009) 513–552. https://doi.org/10.1109/JPROC.2009.2013612.

[92] A.S. Fiorillo, C.D. Critello, A.S. Pullano, Theory, technology and applications of piezoresistive sensors: A review, Sensors and Actuators, A: Physical. 281 (2018) 156–175. https://doi.org/10.1016/j.sna.2018.07.006.

[93] J.C. Doll, B.L. Pruitt, Piezoresistor design and applications, 2013. https://doi.org/10.1007/978-1-4614-8517-9.

[94] A.C.H. Rowe, Piezoresistance in silicon and its nanostructures, Journal of Materials Research. 29 (2014) 731–744. https://doi.org/10.1557/jmr.2014.52.

[95] G. Wang, C. Wang, F. Zhang, X. Yu, Electrical percolation of nanoparticle-polymer composites, Computational Materials Science. 150 (2018) 102–106. https://doi.org/10.1016/j.commatsci.2018.03.051.

[96] A.I. Maaroof, B.L. Evans, Onset of electrical conduction in Pt and Ni films, Journal of Applied Physics. 76 (1998) 1047. https://doi.org/10.1063/1.357822.

[97] H. Wei, H. Eilers, From silver nanoparticles to thin films: Evolution of microstructure and electrical conduction on glass substrates, Journal of Physics and Chemistry of Solids. 70 (2009) 459–465. https://doi.org/10.1016/J.JPCS.2008.11.012.

[98] S. Yamamuro, K. Sumiyama, T. Hihara, K. Suzuki, Geometrical and electrical percolation in nanometre-sized Co-cluster assemblies, Journal of Physics Condensed Matter. 11 (1999) 3247–3257. https://doi.org/10.1088/0953-8984/11/16/006.

[99] D. Stauffer, A. Aharony, Introduction To Percolation Theory : Second Edition, Introduction To Percolation Theory. (2018). https://doi.org/10.1201/9781315274386.

[100] D. Ponnamma, N. Ninan, S. Thomas, Carbon Nanotube Tube Filled Polymer Nanocomposites and Their Applications in Tissue Engineering, Applications of Nanomaterials. (2018) 391–414. https://doi.org/10.1016/B978-0-08-101971-9.00014-4.

[101] Fundamentals of Polymer Matrix Composites Containing CNTs, Carbon Nanotube Reinforced Composites: CNR Polymer Science and Technology. (2015) 125–170. https://doi.org/10.1016/B978-1-4557-3195-4.00005-9.

[102] I. Balberg, Tunnelling and percolation in lattices and the continuum, Journal of Physics D: Applied Physics. 42 (2009) 064003. https://doi.org/10.1088/0022-3727/42/6/064003.

[103] G. Ambrosetti, C. Grimaldi, I. Balberg, T. Maeder, A. Danani, P. Ryser, Solution of the tunneling-percolation problem in the nanocomposite regime, Physical Review B - Condensed Matter and Materials Physics. 81 (2010) 155434. https://doi.org/10.1103/PhysRevB.81.155434.

[104] J.E. Barborini, G. Corbelli, G. Bertolini, P. Repetto, M. Leccardi, S. Vinati, P. Milani, The influence of nanoscale morphology on the resistivity of cluster-assembled nanostructured metallic thin films, New Journal of Physics. 12 (2010) 073001. https://doi.org/10.1088/1367-2630/12/7/073001.

[105] A.D.F. Dunbar, J.G. Partridge, M. Schulze, S.A. Brown, Morphological differences between Bi, Ag and Sb nano-particles and how they affect the percolation of current through nano-particle networks, The European Physical Journal D. 39 (2006) 415–422. https://doi.org/10.1140/EPJD/E2006-00113-4.

[106] M. Mirigliano, F. Borghi, A. Podestà, A. Antidormi, L. Colombo, P. Milani, Non-ohmic behavior and resistive switching of Au cluster-assembled films beyond the percolation threshold, Nanoscale Advances. 1 (2019) 3119–3130. https://doi.org/10.1039/C9NA00256A.

[107] J. Schmelzer, S.A. Brown, A. Wurl, M. Hyslop, R.J. Blaikie, Finite-size effects in the conductivity of cluster assembled nanostructures, Physical Review Letters. 88 (2002) 226802/1-226802/4. https://doi.org/10.1103/PhysRevLett.88.226802.

[108] S. Kim, S. Choi, E. Oh, J. Byun, H. Kim, B. Lee, S. Lee, Y. Hong, Revisit to three-dimensional percolation theory: Accurate analysis for highly stretchable conductive composite materials, Scientific Reports 2016 6:1. 6 (2016) 1–10. https://doi.org/10.1038/srep34632.

[109] M. Park, J. Park, U. Jeong, Design of conductive composite elastomers for stretchable electronics, Nano Today. 9 (2014) 244–260. https://doi.org/10.1016/J.NANTOD.2014.04.009.

[110] H. Hwang, Y. Kim, J.-H. Park, U. Jeong, H. Hwang, U. Jeong, Y. Kim, J. Park, J. Park MPPHC-CPM, 2D Percolation Design with Conductive Microparticles for Low-Strain Detection in a Stretchable Sensor, Advanced Functional Materials. 30 (2020) 1908514. https://doi.org/10.1002/ADFM.201908514.

[111] S.Z. Bisri, S. Shimizu, M. Nakano, Y. Iwasa, Endeavor of Iontronics: From Fundamentals to Applications of Ion-Controlled Electronics, Advanced Materials. 29 (2017) 1607054. https://doi.org/10.1002/adma.201607054.

[112] L.C. Tomé, L. Porcarelli, ab E. Jason Bara, M. Forsyth abd, D. Mecerreyes, Emerging iongel materials towards applications in energy and bioelectronics, Materials Horizons. 8 (2021) 3239–3265. https://doi.org/10.1039/D1MH01263K.

[113] G. Zhao, B. Lv, H. Wang, B. Yang, Z. Li, R. Junfang, G. Gui, W. Liu, S. Yang, L. Li, Ionogel-based flexible stress and strain sensors, Https://Doi.Org/10.1080/19475411.2021.1958085. 12 (2021) 307–336. https://doi.org/10.1080/19475411.2021.1958085.

[114] T.Y. Kim, W. Suh, U. Jeong, Approaches to deformable physical sensors: Electronic versus iontronic, Materials Science and Engineering R: Reports. 146 (2021) 100640. https://doi.org/10.1016/j.mser.2021.100640.

[115] M.S. us Sarwar, Y. Dobashi, E.F. Scabeni Glitz, M. Farajollahi, S. Mirabbasi, S. Naficy, G.M. Spinks, J.D.W. Madden, Transparent and conformal "piezoionic" touch sensor, in: Electroactive Polymer Actuators and Devices (EAPAD) 2015, 2015: p. 943026. https://doi.org/10.1117/12.2085598.

[116] Y. Dobashi, G. Allegretto, M.S. Sarwar, E. Cretu, J.D.W. Madden, Mechanoionic Transduction of Solid Polymer Electrolytes and Potential Applications, MRS Advances. 1 (2016) 63–68. https://doi.org/10.1557/adv.2016.74.

[117] Y. Liu, Y. Hu, J. Zhao, G. Wu, X. Tao, W. Chen, Self-Powered Piezoionic Strain Sensor toward the Monitoring of Human Activities, Small. 12 (2016) 5074–5080. https://doi.org/10.1002/smll.201600553.

[118] Y. Dobashi, Characterization of Ionic Polymers TOwards Applications as Soft Sensors in Medicine, (2016). https://doi.org/10.14288/1.0319317.

[119] V. Triandafilidi, S.G. Hatzikiriakos, J. Rottler, Molecular simulations of the piezoionic effect, Soft Matter. 14 (2018) 6222–6229. https://doi.org/10.1039/c8sm00939b.

[120] V. Woehling, G.T.M. Nguyen, C. Plesse, Y. Petel, Y. Dobashi, J.D.W. Madden, C.A. Michal, F. Vidal, Study of the piezoionic effect and influence of electrolyte in conducting polymer based soft strain sensors, Multifunctional Materials. 2 (2019) 045002. https://doi.org/10.1088/2399-7532/ab56a2.

[121] H. Ohshima, S. Ohki, Donnan potential and surface potential of a charged membrane., Biophysical Journal. 47 (1985) 673. https://doi.org/10.1016/S0006-3495(85)83963-1.

[122] Y. Liu, Y. Hu, J. Zhao, G. Wu, X. Tao, W. Chen, Self-Powered Piezoionic Strain Sensor toward the Monitoring of Human Activities, Small. 12 (2016) 5074–5080. https://doi.org/10.1002/smll.201600553.

[123] A. Adjaoud, G.T.M. Nguyen, L. Chikh, S. Péralta, L. Trouillet-Fonti, N. Uguen, M.D. Braida, C. Plesse, Piezoionic sensors based on formulated PEDOT:PSS and Aquivion®for ionic polymer-polymer composites, Smart Materials and Structures. 30 (2021) 105027. https://doi.org/10.1088/1361-665X/ac1e63.

[124] M. Li, J. Qiao, C. Zhu, Y. Hu, K. Wu, S. Zeng, W. Yang, H. Zhang, Y. Wang, Y. Wu, R. Zang, X. Wang, J. Di, Q. Li, Gel-Electrolyte-Coated Carbon Nanotube Yarns for Self-Powered and Knittable Piezoionic Sensors, ACS Applied Electronic Materials. 3 (2021) 944–954. https://doi.org/10.1021/acsaelm.0c01044.

[125] S. Mishra, L. Unnikrishnan, S.K. Nayak, S. Mohanty, Advances in Piezoelectric Polymer Composites for Energy Harvesting Applications: A Systematic Review, Macromolecular Materials and Engineering. 304 (2019) 1–25. https://doi.org/10.1002/mame.201800463.

[126] H. Parangusan, D. Ponnamma, M. Al Ali Almaadeed, Flexible tri-layer piezoelectric nanogenerator based on PVDF-HFP/Ni-doped ZnO nanocomposites, RSC Advances. 7 (2017) 50156–50165. https://doi.org/10.1039/c7ra10223b.

[127] C. Dagdeviren, P. Joe, O.L. Tuzman, K. Il Park, K.J. Lee, Y. Shi, Y. Huang, J.A. Rogers, Recent progress in flexible and stretchable piezoelectric devices for mechanical energy harvesting, sensing and actuation, Extreme Mechanics Letters. 9 (2016) 269–281. https://doi.org/10.1016/j.eml.2016.05.015.

[128] Z. Hanani, I. Izanzar, M. Amjoud, D. Mezzane, M. Lahcini, H. Uršič, U. Prah, I. Saadoune, M. El Marssi, I.A. Luk'yanchuk, Z. Kutnjak, M. Gouné, Lead-free nanocomposite piezoelectric nanogenerator film for biomechanical energy harvesting, Nano Energy. 81 (2021) 105661. https://doi.org/10.1016/j.nanoen.2020.105661.

[129] S. Gupta, R. Bhunia, B. Fatma, D. Maurya, D. Singh, Prateek, R. Gupta, S. Priya, R.K. Gupta, A. Garg, Multifunctional and Flexible Polymeric Nanocomposite Films with Improved Ferroelectric and Piezoelectric Properties for Energy Generation Devices, ACS Applied Energy Materials. 2 (2019) 6364–6374. https://doi.org/10.1021/acsaem.9b01000.

[130] D. Singh, A. Choudhary, A. Garg, Flexible and Robust Piezoelectric Polymer Nanocomposites Based Energy Harvesters, ACS Applied Materials and Interfaces. 10 (2018) 2793–2800. https://doi.org/10.1021/acsami.7b16973.

[131] J.S. Dodds, F.N. Meyers, K.J. Loh, Piezoelectric characterization of PVDF-TrFE thin films enhanced with ZnO nanoparticles, IEEE Sensors Journal. 12 (2012) 1889–1890. https://doi.org/10.1109/JSEN.2011.2182043.

[132] A. Choudhury, Dielectric and piezoelectric properties of polyetherimide/BaTiO3 nanocomposites, Materials Chemistry and Physics. 121 (2010) 280–285. https://doi.org/10.1016/j.matchemphys.2010.01.035.

[133] S. Bodkhe, G. Turcot, F.P. Gosselin, D. Therriault, One-Step Solvent Evaporation-Assisted 3D Printing of Piezoelectric PVDF Nanocomposite Structures, ACS Applied Materials and Interfaces. 9 (2017) 20833–20842. https://doi.org/10.1021/acsami.7b04095.

[134] K. Kim, W. Zhu, X. Qu, C. Aaronson, W.R. McCall, S. Chen, D.J. Sirbuly, 3D optical printing of piezoelectric nanoparticle-polymer composite materials, ACS Nano. 8 (2014) 9799–9806. https://doi.org/10.1021/nn503268f.

[135] B. Dudem, D.H. Kim, L.K. Bharat, J.S. Yu, Highly-flexible piezoelectric nanogenerators with silver nanowires and barium titanate embedded composite

films for mechanical energy harvesting, Applied Energy. 230 (2018) 865–874. https://doi.org/10.1016/j.apenergy.2018.09.009.

[136] S. Cherumannil Karumuthil, S.P. Rajeev, S. Varghese, Piezo-tribo nanoenergy harvester using hybrid polydimethyl siloxane based nanocomposite, Nano Energy. 40 (2017) 487–494. https://doi.org/10.1016/j.nanoen.2017.08.052.

[137] A. Šutka, P.C. Sherrell, N.A. Shepelin, L. Lapčinskis, K. Mālnieks, A. v. Ellis, Measuring Piezoelectric Output—Fact or Friction?, Advanced Materials. 32 (2020) 2002979. https://doi.org/10.1002/adma.202002979.

[138] M. Stewart, M.G. Cain, Direct Piezoelectric Measurement: The Berlincourt Method, in: Springer, Dordrecht, 2014: pp. 37–64. https://doi.org/10.1007/978-1-4020-9311-1_3.

[139] M.J. Lodeiro, M. Stewart, M. Cain, A round-robin to measure the direct piezeolectric coefficient using the berlincourt method, National Physical Laboratory, 2004.

[140] Anon, Ieee Standard on Piezoelectricity., American National Standards Institute, Standards. (1978).

[141] L. Shu, T. Wang, X. Jiang, W. Huang, Verification of the flexoelectricity in barium strontium titanate through d33 meter, AIP Advances. 6 (2016) 125003. https://doi.org/10.1063/1.4968524.

[142] K.H. Lam, H.L.W. Chan, H.S. Luo, Q.R. Yin, Z.W. Yin, Piezoelectrically actuated ejector using PMN-PT single crystal, Sensors and Actuators A. 121 (2005) 197–202. https://doi.org/10.1016/j.sna.2005.01.003.

[143] M.G. Gonzalez, P.A. Sorichetti, L.C. Brazzano, G.D. Santiago, Electromechanical characterization of piezoelectric polymer thin films in a broad frequency range, Polymer Testing. 37 (2014) 163–169. https://doi.org/10.1016/j.polymertesting.2014.05.014.

[144] L. Seminara, M. Capurro, P. Cirillo, G. Cannata, M. Valle, Electromechanical characterization of piezoelectric PVDF polymer films for tactile sensors in robotics applications, Sensors and Actuators, A: Physical. 169 (2011) 49–58. https://doi.org/10.1016/j.sna.2011.05.004.

[145] R.I. Mahdi, W.H. Abd Majid, Piezoelectric and pyroelectric properties of BNT-base ternary lead-free ceramic-polymer nanocomposites under different poling

conditions, RSC Advances. 6 (2016) 81296–81309. https://doi.org/10.1039/c6ra12033d.

[146] J.S. Wilson, Sensor Technology Handbook, Elsevier Inc., 2005. https://doi.org/10.1016/B978-0-7506-7729-5.X5040-X.

[147] A. Barzegar, D. Damjanovic, N. Setter, The Effect of Boundary Conditions and Sample Aspect Ratio on Apparent d33 Piezoelectric Coefficient Determined by Direct Quasistatic Method, IEEE Transactions on Ultrasonics, Ferroelectrics, and Frequency Control. 51 (2004) 262–270. https://doi.org/10.1109/TUFFC.2004.1295405.

[148] A. Gandelli, R. Ottoboni, Charge amplifiers for piezoelectric sensors, Conference Record - IEEE Instrumentation and Measurement Technology Conference. 1 (1993) 465–468. https://doi.org/10.1109/imtc.1993.382598.

[149] R.A. Shanks, I. Kong, General Purpose Elastomers: Structure, Chemistry, Physics and Performance, (2013) 11–45. https://doi.org/10.1007/978-3-642-20925-3_2.

[150] I.D. Johnston, D.K. McCluskey, C.K.L. Tan, M.C. Tracey, Mechanical characterization of bulk Sylgard 184 for microfluidics and microengineering, Journal of Micromechanics and Microengineering. 24 (2014) 035017. https://doi.org/10.1088/0960-1317/24/3/035017.

[151] M. Liu, J. Sun, Y. Sun, C. Bock, Q. Chen, Thickness-dependent mechanical properties of polydimethylsiloxane membranes, Journal of Micromechanics and Microengineering. 19 (2009) 035028. https://doi.org/10.1088/0960-1317/19/3/035028.

[152] M. Liu, J. Sun, Q. Chen, Influences of heating temperature on mechanical properties of polydimethylsiloxane, Sensors and Actuators, A: Physical. 151 (2009) 42–45. https://doi.org/10.1016/J.SNA.2009.02.016.

[153] L. Mullins, Softening of Rubber by Deformation, Rubber Chemistry and Technology. 42 (1969) 339–362. https://doi.org/10.5254/1.3539210.

[154] K. Wegner, P. Piseri, H.V. Tafreshi, P. Milani, Cluster beam deposition: A tool for nanoscale science and technology, Journal of Physics D: Applied Physics. 39 (2006) R439–R459. https://doi.org/10.1088/0022-3727/39/22/R02.

[155] F. Borghi, C. Melis, C. Ghisleri, A. Podestà, L. Ravagnan, L. Colombo, P. Milani, Stretchable nanocomposite electrodes with tunable mechanical properties by supersonic cluster beam implantation in elastomers, Applied Physics Letters. 106 (2015). https://doi.org/10.1063/1.4916350.

[156] F. Borghi, C. Melis, C. Ghisleri, A. Podestà, L. Ravagnan, L. Colombo, P. Milani, Stretchable nanocomposite electrodes with tunable mechanical properties by supersonic cluster beam implantation in elastomers, Applied Physics Letters. 106 (2015) 121902. https://doi.org/10.1063/1.4916350.

[157] K. Wegner, P. Piseri, H.V. Tafreshi, P. Milani, Cluster beam deposition: A tool for nanoscale science and technology, Journal of Physics D: Applied Physics. 39 (2006) 439–459. https://doi.org/10.1088/0022-3727/39/22/R02.

[158] P. Piseri, A. Podestà, E. Barborini, P. Milani, Production and characterization of highly intense and collimated cluster beams by inertial focusing in supersonic expansions, Review of Scientific Instruments. 72 (2001) 2261. https://doi.org/10.1063/1.1361082.

[159] E. Barborini, P. Piseri, P. Milani, A pulsed microplasma source of high intensity supersonic carbon cluster beams, Journal of Physics D: Applied Physics. 32 (1999) L105. https://doi.org/10.1088/0022-3727/32/21/102.

[160] H. Vahedi Tafreshi, P. Piseri, G. Benedek, P. Milani, The role of gas dynamics in operation conditions of a Pulsed Microplasma Cluster Source for nanostructured thin films deposition, Journal of Nanoscience and Nanotechnology. 6 (2006) 1140–1149. https://doi.org/10.1166/JNN.2006.139.

[161] H. v. Tafreshi, G. Benedek, P. Piseri, S. Vinati, E. Barborini, P. Milani, A Simple Nozzle Configuration for the Production of Low Divergence Supersonic Cluster Beam by Aerodynamic Focusing, Http://Dx.Doi.Org/10.1080/02786820252883838. 36 (2010) 593–606. https://doi.org/10.1080/02786820252883838.

[162] E. Barborini, S. Vinati, M. Leccardi, P. Repetto, G. Bertolini, O. Rorato, L. Lorenzelli, M. Decarli, V. Guarnieri, C. Ducati, P. Milani, Batch fabrication of metal oxide sensors on micro-hotplates, Journal of Micromechanics and Microengineering. 18 (2008) 055015. https://doi.org/10.1088/0960-1317/18/5/055015.

[163] M. Marelli, G. Divitini, C. Collini, L. Ravagnan, G. Corbelli, C. Ghisleri, A. Gianfelice, C. Lenardi, P. Milani, L. Lorenzelli, Flexible and biocompatible microelectrode arrays fabricated by supersonic cluster beam deposition on SU-8, Journal of Micromechanics and Microengineering. 21 (2011) 045013. https://doi.org/10.1088/0960-1317/21/4/045013.

[164] A. Zabet-Khosousi, A.A. Dhirani, Charge Transport in Nanoparticle Assemblies, Chemical Reviews. 108 (2008) 4072–4124. https://doi.org/10.1021/CR0680134.

[165] T. Andersson, The electrical properties of ultrathin gold films during and after their growth on glass, Journal of Physics D: Applied Physics. 9 (1976) 973–985. https://doi.org/10.1088/0022-3727/9/6/010.

[166] F.A. Burgmann, S.H.N. Lim, D.G. McCulloch, B.K. Gan, K.E. Davies, D.R. McKenzie, M.M.M. Bilek, Electrical conductivity as a measure of the continuity of titanium and vanadium thin films, Thin Solid Films. 474 (2005) 341–345. https://doi.org/10.1016/J.TSF.2004.09.020.

[167] R.F. Voss, R.B. Laibowitz, E.I. Allessandrini, Fractal (Scaling) Clusters in Thin Gold Films near the Percolation Threshold, Physical Review Letters. 49 (1982) 1441. https://doi.org/10.1103/PhysRevLett.49.1441.

[168] C. Ghisleri, F. Borghi, L. Ravagnan, A. Podestà, C. Melis, L. Colombo, P. Milani, Patterning of gold–polydimethylsiloxane (Au–PDMS) nanocomposites by supersonic cluster beam implantation, Journal of Physics D: Applied Physics. 47 (2013) 015301. https://doi.org/10.1088/0022-3727/47/1/015301.

[169] G. Corbelli, C. Ghisleri, M. Marelli, P. Milani, L. Ravagnan, Highly deformable nanostructured elastomeric electrodes with improving conductivity upon cyclical stretching, Advanced Materials. 23 (2011) 4504–4508. https://doi.org/10.1002/adma.201102463.

[170] T. Dotan, Y. Berg, L. Migliorini, S.M. Villa, T. Santaniello, P. Milani, Y. Shacham-Diamand, Soft and flexible gold microelectrodes by supersonic cluster beam deposition and femtosecond laser processing, (2020). https://doi.org/10.1016/j.mee.2020.111478.

[171] S.M. Villa, V.M. Mazzola, T. Santaniello, E. Locatelli, M. Maturi, L. Migliorini, I. Monaco, C. Lenardi, M. Comes Franchini, P. Milani, Soft Piezoionic/Piezoelectric Nanocomposites Based on Ionogel/BaTiO3

Nanoparticles for Low Frequency and Directional Discriminative Pressure Sensing, ACS Macro Letters. 8 (2019) 414–420. https://doi.org/10.1021/acsmacrolett.8b01011.

[172] K. Uchino, E. Sadanaga, T. Hirose, Dependence of the Crystal Structure on Particle Size in Barium Titanate, Journal of the American Ceramic Society. 72 (1989) 1555–1558. https://doi.org/10.1111/j.1151-2916.1989.tb07706.x.

[173] S. Yoon, S. Baik, M.G. Kim, N. Shin, Formation mechanisms of tetragonal barium titanate nanoparticles in alkoxide-hydroxide sol-precipitation synthesis, Journal of the American Ceramic Society. 89 (2006) 1816–1821. https://doi.org/10.1111/j.1551-2916.2006.01056.x.

[174] S. Pradhan, G.S. Roy, Study the Crystal Structure and Phase Transition of BaTiO 3 – A Pervoskite, Researcher. 55 (2013) 63–67. http://www.sciencepub.net/researcher%5Cnhttp://www.sciencepub.net.10 (accessed February 25, 2019).

[175] E.K. Al-Shakarchi, N.B. Mahmood, Three Techniques Used to Produce BaTiO 3 Fine Powder, Journal of Modern Physics. 02 (2011) 1420–1428. https://doi.org/10.4236/jmp.2011.211175.

[176] W. Li, Z. Xu, R. Chu, P. Fu, J. Hao, Structure and electrical properties of BaTiO3 prepared by sol-gel process, Journal of Alloys and Compounds. 482 (2009) 137–140. https://doi.org/10.1016/j.jallcom.2009.02.137.

[177] K. Kim, W. Zhu, X. Qu, C. Aaronson, W.R. McCall, S.C. Chen, D.J. Sirbuly, 3D Optical Printing of Piezoelectric Nanoparticle - Polymer Composite Materials, Acs Nano. 8 (2014) 9799–9806. https://doi.org/10.1021/nn503268f.

[178] S.H. Yeon, K.S. Kim, S. Choi, H. Lee, H.S. Kim, H. Kim, Physical and electrochemical properties of 1-(2-hydroxyethyl)-3-methyl imidazolium and N-(2-hydroxyethyl)-N-methyl morpholinium ionic liquids, Electrochimica Acta. 50 (2005) 5399–5407. https://doi.org/10.1016/j.electacta.2005.03.020.

[179] J. Li, Z. Zhu, L. Fang, S. Guo, U. Erturun, Z. Zhu, J.E. West, S. Ghosh, S.H. Kang, Analytical, numerical, and experimental studies of viscoelastic effects on the performance of soft piezoelectric nanocomposites, Nanoscale. 9 (2017) 14215–14228. https://doi.org/10.1039/c7nr05163h.

[180] K. Demirelli, M. Coşkun, E. Kaya, A detailed study of thermal degradation of poly(2-hydroxyethyl methacrylate), Polymer Degradation and Stability. 72 (2001) 75–80. https://doi.org/10.1016/S0141-3910(00)00204-4.

[181] M. Fukagawa, Y. Koshiba, T. Fukushima, M. Morimoto, K. Ishida, Anomalous piezoelectric properties of poly(vinylidene fluoride-trifluoroethylene)/ionic liquid gels, Japanese Journal of Applied Physics. 57 (2018) 04FL06. https://doi.org/10.7567/JJAP.57.04FL06.

[182] S.C.B. Mannsfeld, B.C.K. Tee, R.M. Stoltenberg, C.V.H.H. Chen, S. Barman, B.V.O. Muir, A.N. Sokolov, C. Reese, Z. Bao, Highly sensitive flexible pressure sensors with microstructured rubber dielectric layers, Nature Materials. 9 (2010) 859–864. https://doi.org/10.1038/nmat2834.

[183] Y. Ma, J. Choi, A. Hourlier-Fargette, Y. Xue, H.U. Chung, J.Y. Lee, X. Wang, Z. Xie, D. Kang, H. Wang, S. Han, S.-K. Kang, Y. Kang, X. Yu, M.J. Slepian, M.S. Raj, J.B. Model, X. Feng, R. Ghaffari, J.A. Rogers, Y. Huang, Relation between blood pressure and pulse wave velocity for human arteries., Proceedings of the National Academy of Sciences of the United States of America. (2018) 201814392. https://doi.org/10.1073/pnas.1814392115.

[184] X. Liu, D. Wu, H. Wang, Q. Wang, Self-recovering tough gel electrolyte with adjustable supercapacitor performance, Advanced Materials. 26 (2014) 4370–4375. https://doi.org/10.1002/adma.201400240.

[185] J. Park, Y. Lee, J. Hong, Y. Lee, M. Ha, Y. Jung, H. Lim, S.Y. Kim, H. Ko, Tactile-direction-sensitive and stretchable electronic skins based on human-skin-inspired interlocked microstructures, ACS Nano. 8 (2014) 12020–12029. https://doi.org/10.1021/nn505953t.

[186] A. Aggarwal, F. Kirchner, Object recognition and localization: The role of tactile sensors, Sensors (Switzerland). 14 (2014) 3227–3266. https://doi.org/10.3390/s140203227.

[187] H. Wang, M. Totaro, L. Beccai, Toward Perceptive Soft Robots: Progress and Challenges, Advanced Science. 5 (2018) 1800541. https://doi.org/10.1002/advs.201800541.

[188] M. Gudarzi, P. Smolinski, Q.M. Wang, Compression and shear mode ionic polymer-metal composite (IPMC) pressure sensors, Sensors and Actuators, A: Physical. 260 (2017) 99–111. https://doi.org/10.1016/j.sna.2017.04.010.

[189] J. Zhao, S. Han, Y. Yang, R. Fu, Y. Ming, C. Lu, H. Liu, H. Gu, W. Chen, Passive and Space-Discriminative Ionic Sensors Based on Durable Nanocomposite Electrodes toward Sign Language Recognition, ACS Nano. 11 (2017) 8590–8599. https://doi.org/10.1021/acsnano.7b02767.

[190] J.A. Sauer, G.C. Richardson, Fatigue of polymers, International Journal of Fracture. 16 (1980) 499–532. https://doi.org/10.1007/BF02265215.

[191] S. Maiti, P.H. Geubelle, A cohesive model for fatigue failure of polymers, Engineering Fracture Mechanics. 72 (2005) 691–708. https://doi.org/10.1016/j.engfracmech.2004.06.005.

[192] A.C.M. Kuo, Poly (dimethylsiloxane), (1999) 411–435.

[193] A. Cornogolub, P.J. Cottinet, L. Petit, Hybrid energy harvesting systems, using piezoelectric elements and dielectric polymers, Smart Materials and Structures. 25 (2016) 095048. https://doi.org/10.1088/0964-1726/25/9/095048.

[194] C.-X. Liu, J.-W. Choi, Improved Dispersion of Carbon Nanotubes in Polymers at High Concentrations, Nanomaterials. 2 (2012) 329–347. https://doi.org/10.3390/nano2040329.

[195] I. Chae, C.K. Jeong, Z. Ounaies, S.H. Kim, Review on electromechanical coupling properties of biomaterials, ACS Applied Bio Materials. 1 (2018) 936–953. https://doi.org/10.1021/acsabm.8b00309.

[196] F. Galembeck, T.A.L. Burgo, L.B.S. Balestrin, R.F. Gouveia, C.A. Silva, A. Galembeck, Friction, tribochemistry and triboelectricity: Recent progress and perspectives, RSC Advances. 4 (2014) 64280–64298. https://doi.org/10.1039/c4ra09604e.

[197] R.E. Newnham, V. Sundar, R. Yimnirun, J. Su, Q.M. Zhang, Electrostriction: Nonlinear electromechanical coupling in solid dielectrics, Journal of Physical Chemistry B. 101 (1997) 10141–10150. https://doi.org/10.1021/jp971522c.

[198] I.D. Johnston, D.K. McCluskey, C.K.L. Tan, M.C. Tracey, Mechanical characterization of bulk Sylgard 184 for microfluidics and microengineering, Journal of Micromechanics and Microengineering. 24 (2014) 035017. https://doi.org/10.1088/0960-1317/24/3/035017.

[199] J.Z. Manapat, Q. Chen, P. Ye, R.C. Advincula, 3D Printing of Polymer Nanocomposites via Stereolithography, Macromolecular Materials and Engineering. 302 (2017) 1600553. https://doi.org/10.1002/mame.201600553.

[200] X.L. Ma, Research on application of SLA technology in the 3D printing technology, in: Applied Mechanics and Materials, Trans Tech Publications Ltd, 2013: pp. 938–941. https://doi.org/10.4028/www.scientific.net/AMM.401-403.938.

[201] M. Maturi, C. Pulignani, E. Locatelli, V. Vetri Buratti, S. Tortorella, L. Sambri, M. Comes Franchini, Phosphorescent bio-based resin for digital light processing (DLP) 3D-printing, Green Chemistry. 22 (2020) 6212–6224. https://doi.org/10.1039/d0gc01983f.

[202] J.J. Relinque, A.S. de León, J. Hernández-Saz, M.G. García-Romero, F.J. Navas-Martos, G. Morales-Cid, S.I. Molina, Development of surface-coated Polylactic Acid/Polyhydroxyalkanoate (PLA/PHA) nanocomposites, Polymers. 11 (2019). https://doi.org/10.3390/POLYM11030400.

[203] M. Maturi, C. Pulignani, E. Locatelli, V. Vetri Buratti, S. Tortorella, L. Sambri, M. Comes Franchini, Phosphorescent bio-based resin for digital light processing (DLP) 3D-printing †, (2020). https://doi.org/10.1039/d0gc01983f.

[204] T. Santaniello, L. Migliorini, Y. Yan, C. Lenardi, P. Milani, Supersonic cluster beam fabrication of metal–ionogel nanocomposites for soft robotics, Journal of Nanoparticle Research. 20 (2018) 250. https://doi.org/10.1007/s11051-018-4352-x.

[205] H. Kim, S.M. Kim, H. Son, H. Kim, B. Park, J. Ku, J.I. Sohn, K. Im, J.E. Jang, J.J. Park, O. Kim, S. Cha, Y.J. Park, Enhancement of piezoelectricity via electrostatic effects on a textile platform, Energy and Environmental Science. 5 (2012) 8932–8936. https://doi.org/10.1039/c2ee22744d.

[206] K. Prashanthi, N. Miriyala, R.D. Gaikwad, W. Moussa, V.R. Rao, T. Thundat, Vibtrational energy harvesting using photo-patternable piezoelectric nanocomposite cantilevers, Nano Energy. 2 (2013) 923–932. https://doi.org/10.1016/j.nanoen.2013.03.013.

[207] S. Xu, Y.W. Yeh, G. Poirier, M.C. McAlpine, R.A. Register, N. Yao, Flexible piezoelectric PMN-PT nanowire-based nanocomposite and device, Nano Letters. 13 (2013) 2393–2398.

https://doi.org/10.1021/NL400169T/SUPPL_FILE/NL400169T_SI_001.PDF.

[208] S. Siddiqui, D. il Kim, L.T. Duy, M.T. Nguyen, S. Muhammad, W.S. Yoon, N.E. Lee, High-performance flexible lead-free nanocomposite piezoelectric nanogenerator for biomechanical energy harvesting and storage, Nano Energy. 15 (2015) 177–185. https://doi.org/10.1016/j.nanoen.2015.04.030.

[209] H.B. Kang, C.S. Han, J.C. Pyun, W.H. Ryu, C.Y. Kang, Y.S. Cho, (Na,K)NbO3 nanoparticle-embedded piezoelectric nanofiber composites for flexible nanogenerators, Composites Science and Technology. 111 (2015) 1–8. https://doi.org/10.1016/j.compscitech.2015.02.015.

[210] S.K. Ghosh, T.K. Sinha, B. Mahanty, D. Mandal, Self-poled Efficient Flexible "Ferroelectretic" Nanogenerator: A New Class of Piezoelectric Energy Harvester, Energy Technology. 3 (2015) 1190–1197. https://doi.org/10.1002/ente.201500167.

[211] M.M. Alam, D. Mandal, Native Cellulose Microfiber-Based Hybrid Piezoelectric Generator for Mechanical Energy Harvesting Utility, ACS Applied Materials and Interfaces. 8 (2016) 1555–1558. https://doi.org/10.1021/acsami.5b08168.

[212] V. Bhavanasi, V. Kumar, K. Parida, J. Wang, P.S. Lee, Enhanced Piezoelectric Energy Harvesting Performance of Flexible PVDF-TrFE Bilayer Films with Graphene Oxide, ACS Applied Materials and Interfaces. 8 (2016) 521–529. https://doi.org/10.1021/ACSAMI.5B09502/SUPPL_FILE/AM5B09502_SI_001.PDF.

[213] X. Ren, H. Fan, Y. Zhao, Z. Liu, Flexible Lead-Free BiFeO3/PDMS-Based Nanogenerator as Piezoelectric Energy Harvester, ACS Applied Materials and Interfaces. 8 (2016) 26190–26197. https://doi.org/10.1021/acsami.6b04497.

[214] S. Siddiqui, H.B. Lee, D. il Kim, L.T. Duy, A. Hanif, N.E. Lee, An Omnidirectionally Stretchable Piezoelectric Nanogenerator Based on Hybrid Nanofibers and Carbon Electrodes for Multimodal Straining and Human Kinematics Energy Harvesting, Advanced Energy Materials. 8 (2018) 1701520. https://doi.org/10.1002/aenm.201701520.

[215] K. Shi, B. Sun, X. Huang, P. Jiang, Synergistic effect of graphene nanosheet and BaTiO3 nanoparticles on performance enhancement of electrospun PVDF

nanofiber mat for flexible piezoelectric nanogenerators, Nano Energy. 52 (2018) 153–162. https://doi.org/10.1016/j.nanoen.2018.07.053.

[216] J. Fu, Y. Hou, X. Gao, M. Zheng, M. Zhu, Highly durable piezoelectric energy harvester based on a PVDF flexible nanocomposite filled with oriented BaTi2O5 nanorods with high power density, Nano Energy. 52 (2018) 391–401. https://doi.org/10.1016/j.nanoen.2018.08.006.

[217] S. Cherumannil Karumuthil, S. Prabha Rajeev, U. Valiyaneerilakkal, S. Athiyanathil, S. Varghese, Electrospun Poly(vinylidene fluoride-trifluoroethylene)-Based Polymer Nanocomposite Fibers for Piezoelectric Nanogenerators, ACS Applied Materials and Interfaces. 11 (2019) 40180–40188. https://doi.org/10.1021/acsami.9b17788.

[218] S.K. Karan, D. Mandal, B.B. Khatua, Self-powered flexible Fe-doped RGO/PVDF nanocomposite: An excellent material for a piezoelectric energy harvester, Nanoscale. 7 (2015) 10655–10666. https://doi.org/10.1039/c5nr02067k.

[219] S. Ye, C. Cheng, X. Chen, X. Chen, J. Shao, J. Zhang, H. Hu, H. Tian, X. Li, L. Ma, W. Jia, High-performance piezoelectric nanogenerator based on microstructured P(VDF-TrFE)/BNNTs composite for energy harvesting and radiation protection in space, Nano Energy. 60 (2019) 701–714. https://doi.org/10.1016/j.nanoen.2019.03.096.

[220] S.K. Karan, S. Maiti, A.K. Agrawal, A.K. Das, A. Maitra, S. Paria, A. Bera, R. Bera, L. Halder, A.K. Mishra, J.K. Kim, B.B. Khatua, Designing high energy conversion efficient bio-inspired vitamin assisted single-structured based self-powered piezoelectric/wind/acoustic multi-energy harvester with remarkable power density, Nano Energy. 59 (2019) 169–183. https://doi.org/10.1016/j.nanoen.2019.02.031.

[221] Y. Sun, J. Chen, X. Li, Y. Lu, S. Zhang, Z. Cheng, Flexible piezoelectric energy harvester/sensor with high voltage output over wide temperature range, Nano Energy. 61 (2019) 337–345. https://doi.org/10.1016/j.nanoen.2019.04.055.

[222] X. Guan, B. Xu, J. Gong, Hierarchically architected polydopamine modified BaTiO3@P(VDF-TrFE) nanocomposite fiber mats for flexible piezoelectric nanogenerators and self-powered sensors, Nano Energy. 70 (2020) 104516. https://doi.org/10.1016/j.nanoen.2020.104516.

[223] C. Shuai, G. Liu, Y. Yang, F. Qi, S. Peng, W. Yang, C. He, G. Wang, G. Qian, A strawberry-like Ag-decorated barium titanate enhances piezoelectric and antibacterial activities of polymer scaffold, Nano Energy. 74 (2020) 104825. https://doi.org/10.1016/j.nanoen.2020.104825.

[224] C. Shuai, G. Liu, Y. Yang, W. Yang, C. He, G. Wang, Z. Liu, F. Qi, S. Peng, Functionalized BaTiO3 enhances piezoelectric effect towards cell response of bone scaffold, Colloids and Surfaces B: Biointerfaces. 185 (2020) 110587. https://doi.org/10.1016/j.colsurfb.2019.110587.

LIST OF FIGURES